

UCLA

UCLA Electronic Theses and Dissertations

Title

FlexPower: Integration of Flexible Segmented Li-ion Batteries (Battlet) with Flexible Wireless Charging Technology for Wearable Devices

Permalink

<https://escholarship.org/uc/item/9d15n7zq>

Author

Ouyang, Guangqi

Publication Date

2024

Peer reviewed|Thesis/dissertation

UNIVERSITY OF CALIFORNIA

Los Angeles

FlexPower: Integration of Flexible Segmented Li-ion Batteries (Battlet) with
Flexible Wireless Charging Technology for Wearable Devices

A dissertation submitted in partial satisfaction
of the requirements for the degree
Doctor of Philosophy
in Materials Science and Engineering

by

Guangqi Ouyang

2024

© Copyright by

Guangqi Ouyang

2024

ABSTRACT OF THE DISSERTATION

FlexPower: Integration of Flexible Segmented Li-ion Batteries with
Flexible Wireless Charging Technology for Wearable Devices

by

Guangqi Ouyang

Doctor of Philosophy in Materials Science and Engineering

University of California, Los Angeles, 2024

Professor Subramanian Srikanteswara Iyer, Co-Chair

Professor Bruce S. Dunn, Co-Chair

The proliferation of wearable devices has been significantly hindered by limitations of reliable flexible power solutions. To address this challenge, this dissertation introduces the concept of a flexible Li-ion battery, featuring a partitioned cathode and anode electrode array coated on flexible composite current collectors, which is referred to as the “battlet”. Ionic liquid Lithium bis(fluorosulfonyl)imide (LiFSI) with 1-Butyl-1-methylpyrrolidinium bis(fluorosulfonyl)imide (PYR₁₄FSI) is used as liquid electrolytes to address the flammability concern. The mechanism of mechanical failure during bending, the fabrication of partitioned electrodes, a comparison of the

ionic liquid and organic electrolyte, and electrochemical performance is discussed in this work. Results show that this approach can reduce the crack propagation of the electrodes under mechanical distortion, thus improving electrochemical stability. The full cell battery achieves a 0.7 mAh/cm² capacity density and can withstand around 1000 bending cycles at a 5 mm bending radius.

Additionally, using a flexible Fan-Out Wafer-Level Packaging (FOWLP) platform, FlexTrate™, a flexible wireless charger is designed using resonant magnetic coupling. The wireless charger can withstand up to 5 mm bending radius and can deliver a constant 3.3 V output voltage and 3.9 mW peak power.

The flexible wireless charger, along with the flexible battery, serves as a fully wireless power solution for wearables that we call FlexPower. To integrate the FlexPower with flexible electronics, this dissertation also discusses a 2D and a 3D flexible integration approach based on FlexTrate™. As a demonstration of the 2D approach, the FlexPower is integrated with a UV microLED display array consisting of 33 microLEDs. The power consumption of the LED array is 3 mW, and the flexible battery, with a capacity of 4.6 mWh, can power the microLEDs for more than 1.5 hours. For the 3D integration, the dissertation explores the development of flexible interconnects on the front and back sides of FlexTrate™. A through-glass via die is used to facilitate interconnection between both sides. A detailed experimental study of the SF₆/O₂ plasma PDMS dry-etch method for backside contact opening, interconnect performance, and reliability is also addressed.

This work represents, to the best of our knowledge, the first demonstration of a flexible battery integrated with a flexible wireless charger powering flexible μ LED arrays for wearable applications.

The dissertation of Guangqi Ouyang is approved.

Ali Mosleh

Qibing Pei

Ximin He

Subramanian Srikanteswara Iyer, Committee Co-Chair

Bruce S. Dunn, Committee Co-Chair

University of California, Los Angeles

2024

DEDICATION

To my family...

Table of Contents

CHAPTER 1	Introduction	1
1.1	Development of the wearable devices.....	1
1.2	Needs of a flexible, wireless power supply for wearables	4
1.2.1	Power consumption analysis of wearable devices.....	4
1.2.2	Target specifications of the flexible power solution for wearables	5
1.3	Issues of current power supplies for wearables.....	7
1.4	Introduction to FlexPower.....	11
1.4.1	Flexible battlet Li-ion battery and flexible wireless charger	11
1.4.2	Integration of the flexible battery and wireless charger on FlexTrate™ ...	14
1.5	Contributions of the work	16
1.6	Organization of the dissertation	18
CHAPTER 2	Development of flexible battlet Li-ion battery	20
2.1	Failure analysis of battery electrodes during bending.....	20
2.1.1	Single layer model - definition of flexibility	20
2.1.2	Double layer model – cohesive and adhesive stress on the electrode	21
2.1.3	Failure analysis of conventional planar battery electrodes.....	24
2.2	Geometrical analysis of the battlet	27
2.2.1	Circular design.....	27
2.2.2	Rounded corner square design.....	29
2.3	Modeling of battlet flexibility	31
2.3.1	Comparison of the flexibility of planar electrode and battlet.....	31
2.3.2	Impact of battlet size and spacing on electrode flexibility	34
2.4	Fabrication of battlet battery	37
2.4.1	Fabrication process	37

2.4.2	Surface uniformity	40
2.4.3	Electrode bendability	41
2.4.4	Porosity	43
2.4.5	Adhesion test	47
2.4.6	Comparison of ionic liquid and organic electrolytes	48
2.4.7	Thickness optimization for reducing the surface crack	53
2.4.8	Flexibility and reliability of full cell.....	57
2.4.9	Reliability test.....	61
CHAPTER 3	Development of Flexible Wireless Chargers	64
3.1	Design of wireless power transfer device for charging batteries	64
3.2	Fabrication process.....	67
3.3	Electrical performance	70
3.4	Bendability	73
3.5	Charging ability.....	74
CHAPTER 4	Integration of the FlexPower with wearable devices.....	76
4.1	2D flexible FOWLP	76
4.1.1	Circuit design of integration with μ LED array.....	76
4.1.2	μ LED array characteristics	77
4.1.3	Integration of FlexPower with μ LED array.....	79
4.2	3D flexible FOWLP	81
4.2.1	Through Glass Vias.....	82
4.2.2	Fabrication process	83
4.2.3	PDMS dry etch process	86
4.2.4	Front- and back-side interconnections on 3D FlexTrate™	92
4.2.5	Reliability	94

4.2.6	Inkjet printing of silver ink for integration of 3D FlexTrate™	96
4.2.7	Comparison of 3D FOWLP method with existing technologies	97
CHAPTER 5	Conclusions and outlook	101
5.1	Conclusions	101
5.2	Outlook and future work	102
5.2.1	Inkjet printing approach for battlet fabrication.....	102
5.2.2	Co-plane cathode and anode battlet battery.....	105
5.2.3	Power management on wireless charger.....	106
5.2.4	Integration of the FlexPower with light sensor controller.....	106
Appendix A	Investigation of Die Shift in FlexTrate™ Process.....	107
A.1	Introduction to Fan-Out Wafer-Level Package (FOWLP)	107
A.2	PDMS and its cure kinetic behavior.....	109
A.2.1	PDMS properties	109
A.2.2	PDMS cure reaction.....	109
A.3	Die shift problem.....	112
A.3.1	Die shift analysis on FOWLP	112
A.3.2	Die shift analysis on FlexTrate™	113
A.4	Experimental setup and methodology	115
A.4.1	Flow diagram of the work.....	115
A.4.2	Differential scanning calorimetry test of PDMS cure kinetics	116
A.4.3	PDMS shrinkage and die shift measurement method.....	118
A.4.4	Finite Element Simulation of PDMS Shrinkage and Die Shift	121
A.5	Results of PDMS shrinkage and die shift.....	125
A.5.1	PDMS cure kinetics	125
A.5.2	PDMS shrinkage characterization	129

A.5.3	Parametric study of die shift.....	131
A.5.4	Die shift prediction on surface electromyography (sEMG) system	136
References	139

List of Figures

Figure 1-1 Comparison of FlexTrate™ and conventional FHE.	4
Figure 1-2 BLE nRF52832 operation sequence.	5
Figure 1-3 Structure comparison of the conventional electrode on metal foil current collector and battlet electrode on flexible metal-sputtered current collector.	11
Figure 1-4 Young's modulus of the materials used in this work.	12
Figure 1-5 Exploded view of the battlet flexible battery: rounded-corner electrode array is on the metal current collector and on flexible PDMS substrate.	13
Figure 1-6 (a) schematic view of the flexible wireless charger using flexible Fan-Out Wafer Level Packaging; (b) layout of the wireless charger based on the circuit design.	14
Figure 1-7 (a). schematic view of the flexible 2D FOWLP for wearables. (b). schematic view of the flexible 3D FOWLP using through-glass vias for wearables.	16
Figure 1-8 Organization of the work.	19
Figure 2-1 Single layer bending model.	21
Figure 2-2 double layer model.	22
Figure 2-3 Conventional LFP cathode coated on Al metal current collectors at bending state. ...	25
Figure 2-4 Major failure mechanisms of flexing conventional planar battery electrodes. (a) Crack formation and propagation; (b) electrode layer delamination; (c) electrode layer peel-off; (d) Metal current collector fracture.	26
Figure 2-5 Four of failure modes of conventional planar LFP cathode during mechanical bending cycles: (a). Crack on LFP film; (b). Delamination between LFP and Al current collector; (c). LFP layer peels off from Al current collector; (d). Fracture on Al current collector.	26

Figure 2-6 Experimental design comparing different electrode radii and stacking configurations.	27
Figure 2-7 Calculation of the filling factor for the circular electrode shape design.	28
Figure 2-8 Optical images of PDMS after laser-cut using various circular shape layout.	28
Figure 2-9 Calculation of the filling factor for the rounded corner electrode shape design	29
Figure 2-10 Optical images of PDMS after laser-cut using various rounded corner shape layout from 1 mm spacing distance to 100 μm spacing distance.....	30
Figure 2-11 When cell spacing is 400 μm , battlets are likely to merge.	31
Figure 2-12 Ansys model of a planar electrode and a battlet electrode.	32
Figure 2-13 Strain and stress plot of planar electrode at 5 mm bending radius.	33
Figure 2-14 Strain and stress plot of battlet electrode at 5 mm bending radius (bend at center of left battlet, symmetric).	34
Figure 2-15 Stress plot of different battlet electrode geometries at 5 mm bending radius	35
Figure 2-16 The maximum stress of the flexible current collector in different battlet spacing during bending.....	36
Figure 2-17 Stress plot of different battlet electrode geometries at 5 mm bending radius	36
Figure 2-18 Inward and outward folding of a battlet	37
Figure 2-19 Fabrication process of the battlet battery: (a) Lamination of thermal release tape. (b) Deposition of 5 μm Parylene C. (c) Sputtering 600 nm Al/Cu and etch pattern. (d) Screen printing slurry, wet coating thickness (100-200 μm). (e) Dry slurry and laminate double side PI tape as reservoir. (f) Place separator and dispense electrolyte 100 μL . (g) Assembly the full cell (cathode and anode). (h) Release of the substrate.....	39

Figure 2-20 optical images of 4x4 (a) battlet cathodes and (b) battlet anodes before bending. (c) Confocal microscope images of the surface profile of the cathode electrodes	41
Figure 2-21 optical images of (d) cathodes and (f) anodes after bending test; (e)(f) backside of the cathode and anode showing the bending traces in between each battlet.....	42
Figure 2-22 SEM images of battlet electrode at different positions after 1000 bending cycles ...	43
Figure 2-23 SEM images of the surface of the (a) cathode battlet electrode at the corner and (b) zoom-in image. (c) anode battlet electrode at the corner and (d) zoom-in image.....	44
Figure 2-24 cross-section of LFP cathode (a) in between of electrode (b) and (c) center of the electrode. (d) processed image for porosity measurement	45
Figure 2-25 cross-section of LFP cathode (a) in between of electrode (b) & (c) center of the electrode. (d) processed image for porosity measurement.	46
Figure 2-26 (left) T-peeling test step (right) comparision of the electrode layer - current collector layer adhesion strength.....	47
Figure 2-27 Chemical structure of LiFSI as battery ionic liquid electrolyte an PYR14FSI as solvent for the ionic liquid	49
Figure 2-28 Contact angle measurement indicating the wettability of the ionic liquid on the surface of the LFP electrode.	50
Figure 2-29 Testing results of LFP/ionic liquid electrolyte/Li metal battery system: Charging/discharging cycling at different C-rates for (a) ionic liquid electrolyte and (b) organic electrolyte.....	52
Figure 2-30 Discharge capacity density and columbic efficiency for 20 cycles at 2C rate for (c) ionic liquid electrolyte and (d) 1M LiPF6 in DEC:EC:DMC (1:1:1) organic electrolyte.	53
Figure 2-31 structure model of LFP electrodes (not to scale).....	54

Figure 2-32 Electrode thickness in different slurry compositions and stencil thicknesses	56
Figure 2-33 Calculated capacity of the electrode and the tested capacity of the electrode in different compositions and stencil coating thickness.....	56
Figure 2-34 Optical images of the electrode under different compositions and stencil coating thickness.....	57
Figure 2-35 Batteries at static state at (a) 5 mm bending radius (b) 10 mm bending radius.	58
Figure 2-36 Output voltage at dynamic bending test	59
Figure 2-37 (a) comparison of the rate performance of the battlet battery and planar electrode battery in different C rates. (b)) comparison of the cycling performance of the battlet battery and planar electrode battery	60
Figure 2-38 Comparison of the open circuit voltage variation in 50 hours aging time of the assembled full cell with flexible package and coin cell package in Ar gas environment and in lab environment.....	61
Figure 2-39 Open-circuit voltage of battlet battery under different humidity environment.	62
Figure 2-40 Open-circuit voltage of battlet battery in different temperature environment.....	63
Figure 3-1 Circuit design of the wireless charging system.	65
Figure 3-2 Fabrication process of the wireless charger. (a) Die placement on thermal release tape laminated on a silicon handler. (b) Dispense DPMS and mold with 170 °C TRT on 2nd silicon handler. (c) Release of 1st silicon handler. (d) Deposition of parylene and spin-coat SU8 dielectric layer. (e) Contact opening using RIE dry etch process. (f) Electroplating Cu interconnects. (g) Fabrication of 2nd layer interconnects. (h) Thermal release of the 2nd handler.....	68
Figure 3-3 Optical image of wireless power transfer coils. (a). transmitting coil; (b) and (c) 8 turns of the transmitting coil, the width is 100 μm while the spacing is 50 μm between each turn.	69

Figure 3-4 Optical images of the fabricated wireless charger. (a) LDO. (b) full-wave rectifier using four diode. (c) Dies align to the substrate with $< 1 \mu\text{m}$ shift after pick-and-placement. (d) fabricated device. 70

Figure 3-5 Electrical performance of the wireless charger (a) output voltage in different coupling frequencies and coupling distances; (b) Output voltage vs. bending radius; (c) Output voltage vs. coupling distance..... 72

Figure 3-6 Output voltage at different offset distance at 5V V_{pp} , 13.56 MHz (top) output voltage vs offset. (bottom) Illustration of different offset mode (a) 0 mm, two coils are concentric; (b) 5 mm, two coils are internally tangent; (c) 15 mm, external coil passes the center of internal coils; (d) 25 mm, two coils are externally tangent. Orange coil is the external coil while the yellow coil is the gain coil. 73

Figure 3-7 Bending test of the wireless charger. (left) test setup. (b) The resistance of two power transfer coils bended in 5 mm bending radius in cumulative number of bending cycles up to 1000 times 74

Figure 3-8 (a) Output voltage (purple) and passthrough current (blue) of the wireless charger in different loading resistances. (b) Charging voltage (orange) and charging current (green) of the wireless charger when charging a flexible battery. 75

Figure 4-1 (a) Circuit design of the 2D integration of battery, wireless charger and microLEDs. (b) Design layoutss 77

Figure 4-2 (a) optical images of the μLED array. (b) the LEDs emit near-UV light powered by external source..... 78

Figure 4-3 (a) optical images of the μLED array. (b) light intensity of the μLED in different external voltages..... 78

Figure 4-4 (a) optical image of final integrated sample, and (b) at bending state. 79

Figure 4-5 (a) Measurement of battery output voltage at microLEDs off state, and (b) at LED off state. (c) the operation of the microLEDs by pressing the dome switch..... 80

Figure 4-6 (a) Experiment setup for LED light intensity measurement. (b) LED intensity change during the wireless charging of the battery. 81

Figure 4-7 (a). The optical image of through glass die. The size of the die is 1 x 1.2 mm. Total thickness of the die is 300 μm . The Cu pillar is 40 μm diameter, and the minimum pitch is 100 μm ; (b). Backside vias; Interconnection on the glass die after electroplating. The interconnection of the Cu wire is 40 μm pitches..... 83

Figure 4-8 Fabrication process flow of flexible 3D integration. (a). Placement of TGVs. (b) and (c). Molding and curing of flexible PDMS polymer with the 2nd glass carrier and 120 °C. (d). Release of the 1st glass carrier by heating up to 105 °C. (e) Semi-additive process for the Cu RDL interconnection as same as FlexTrate™; (f). Lamination of 170 °C thermal release tape and 3rd glass carrier for backside RDL process. (g). Release of the 2nd carrier. (h). Deposition of 100 nm Al using lift-off method. (i). Dry etch of PDMS for opening the back side contacts. (j). Wet etch of the Al hard mask. (k). Fabrication of 2nd RDL (l). Open the contact on the interconnection by dry etch method. (m). Deposition of silver paste by Inkjet printing method. (n). Place a 2nd layer of the FlexTrate for bonding. (o). Release of the 3rd handler. 86

Figure 4-9 (a) Structure of test sample. spin-coated PDMS evaporated with 100 nm Al hard mask for plasma etching. (b) Top view of the prepared sample with opening contact from 400 μm diameter to 20 μm diameter. 87

Figure 4-10 Plot of etch power vs etch rate. 88

Figure 4-11 Plot of etch pressure vs. etch rate. 89

Figure 4-12 Etching profile under different etch pressure measured by surface profiler..... 89

Figure 4-13 Etching profile under different etch pressure from 50 mTorr to 270 mTorr measured by optical microscope..... 90

Figure 4-14 Optical image of the etched features shows shadowing issue of dry etching for feature size smaller than 150 μm diameter. 91

Figure 4-15 AFM results show the PDMS surface roughness (a) prior to plasma dry etch, as (b) subsequent to plasma dry etch with a masked Al metal layer, and as (c) after plasma dry etch without an Al metal layer mask. 92

Figure 4-16 Optical images of (a) fabricated sample at a bending state. The total thickness is 300 μm . (b) Electroplated Cu interconnection connected with TGVs. (c) Backside contacts after plasma dry etching. (d) and (e) Interconnections on the TGVs contacts and with SU8 corrugation on the front interconnection. (f) Interconnections on the back side of the TGVs..... 94

Figure 4-17 (a). Illustration of two different measurement positions front RDL (f-RDL) and back RDL (b-RDL) on the test vehicle. (b) Four-probe measurement results..... 95

Figure 4-18 (a) Voltera inkjet printer for dispensing silver interconnect ink. (b) Schematic view of the test vehicle. (c), (d) and (e) the optical images of test samples..... 97

Figure 5-1 Inkjet printer and inkjet printed battlet electrodes..... 103

Figure 5-2 Confocal microscope results of the surface profile of the inkjet - printing cathode electrodes..... 104

Figure 5-3 Comparison of the profile of screen-printing electrodes and inkjet-printing electrodes. 104

Figure 5-4 Co-plane cathode and anode battlet battery..... 105

Figure 5-5 No-contact light-control switch integrated with battlet battery and LED array 106

Figure A-1 Structure of FI-WLP (Left) and FO-WLP (Right).....	107
Figure A-2 FOWLP process flow: (a). Align Tape on Handler; (b). Die placement; (c). Wafer level Molding; (d). Release from handler; (e). RDL and Bumping processing; (f). Singulation	109
Figure A-3 Cure process of PDMS. (a). Monomer; (b). Monomer starts reaction; (c). Network formation; (d). Fully cured.....	110
Figure A-4 Two parts of PDMS. (a). Base structure; (b). Cure Agent structure.[11].....	112
Figure A-5 RDL layer construction. (a). FOWLP, epoxy is free without support handler; (b). FlexTrate™, PDMS is held by a wafer handler.	114
Figure A-6 The flow diagram of this work.....	116
Figure A-7 Perkin Elmer DSC 8000	117
Figure A-8 FlexTrate™ process for PDMS shrinkage measurement: (a). Align thermal release tape on Si wafer; (b). Deposit Parylene C (1 μm), gold (50 nm) and photoresist SU8 (0.5 μm); (c). Lithograph SU8 and dry etch gold to create pattern; (d). Dispense PDMS; Cover Second handler and Cure; (e). Release 1 st handler and measure pattern interval change; (f). Release 2 nd handler and measure pattern interval change.....	119
Figure A-9 Mark matrix layout after release 1st handler. The blue background is PDMS and yellow crosses are gold marks.....	120
Figure A-10 Lab Owned Nanotronics Co. nSpec Tool.	121
Figure A-11 Workflow of PDMS cure, PDMS shrinkage, and die shift simulation in ANSYS Workbench.....	122
Figure A-12 Geometry model in ANSYS simulation. (a). Top View of PDMS embed with dies; (c). Cross section of PDMS embed with dies.	123

Figure A-13 DSC Results: (a). Dynamic DSC curves; (b) and their running integral at different heating rates..... 125

Figure A-14 Autocatalytic model at varying conversions. 127

Figure A-15 Comparing the autocatalytic Model with experiment results. 128

Figure A-16 ANSYS Transient Thermal module simulation of (a). PDMS degree of cure, and (b). Heat of reaction verse time in FlexTrate™ process. 129

Figure A-17 (a). 90mm diameter PDMS with gold pattern; (b). Gold pattern on PDMS taken by nSpecs..... 129

Figure A-18 Gold patterns shift on PDMS due to cure shrinkage (a). after release first handler; (b). After release second handler. 130

Figure A-19 PDMS shrinkage simulation after release (a) first handler and (b) second handler. 131

Figure A-20 Points: the experiment average shrinkage of PDMS verse distance from the center. Lines: the simulation results of PDMS shrinkage verse distance from the center. 131

Figure A-21 (a). One of the die shift simulation results. (b). The scaled figure of (a), the black wireframe is the original die's position. 133

Figure A-22 The data select rule on each simulation. 133

Figure A-23 (a). Simulation results of die shift verse die distance from center to the corner of matrix in different die size; (b). Die shift ratio verse different die sizes..... 134

Figure A-24 Simulation results of die shift verse die intervals from center to the corner of matrix in different die size 135

Figure A-25 Die shift difference (a). between different die thickness, and (b). different PDMS Thickness..... 136

Figure A-26 (a). The geometry of two mirror-designed flexible sEMG systems on PDMS. Number 1 & 2 are Bluetooth chips; 3, 4, 6, 7 are capacitors, and 5, 8 are amplifiers. (b). Simulation of the die shift in x axis direction. (c). Simulation of the die shift in y axis. 137

List of Tables

Table 1-1 Target specs of battery for operation of a sEMG 8 hours per day for a year	6
Table 2-1 Statistical results of LFP cathode cross-section by Image J.....	45
Table 2-2 Statistical results of graphite anode cross-section by Image J	46
Table 2-3 Electrode performance test parameters and value.....	50
Table 2-4 Design of experiment for the optimization of the electrode slurry optimization.....	55
Table 3-1 List of components utilized in this study.....	66
Table 3-2 Design of the transmission and receive coils.	67
Table 4-1 Comparison of different multilayer integration methods.....	99
Table 5-1 Selected specs of DSC 8000	117
Table 5-2 Specs of Nanotronics Co. nSpec tool.....	121
Table 5-3 List of boundary conditions	124
Table 5-4 The parameters of the simulation design.	124
Table 5-5 Summary of DSC experiment results.....	125
Table 5-6 Summary of die dimensions and die shift results.	138

ACKNOWLEDGEMENTS

I would like to take this opportunity to express my sincere gratitude to my advisor, Prof. Subramanian S. Iyer, for his invaluable guidance throughout my research work. From him, I have learned not only a wealth of knowledge but also the importance of a continuous eagerness to learn new things and the value of diligent work. I deeply appreciate his dedication to my education and growth.

I thank Prof. Bruce Dunn, Prof. Ali Mosleh, Prof. Qibing Pei, and Prof. Ximin He for providing a critical review of this work and for serving as members of my dissertation committee.

I would like to thank Dr. Venkat Srinivasan, director of the Argonne Collaborative Center for Energy Storage Science (ACCESS), for his generous help and discussions on battery electrodes.

I would like to thank Jacky (Tsz Tat) Yu, Makena White, Dr. Grace Whang and Dr. Christopher S. Choi from the Dunn Lab for their help on the battery testing, electrolyte system development, and useful discussions.

I would like to thank 3D Glass Solutions Inc. for providing the through-glass via dies and Neware Technology LLC for providing the battery tester.

I would like to thank NMBC, the UC system, and the UCLA CHIPS consortium for supporting this work in parts.

I would like to thank all my colleagues: Mansi Sheth, Henry Sun, Randall Irwin, Golam Sabbir, Haoxiang Ren, Krutikesh Sahoo, Vineeth Harish, Jui Han Liu, Cheng-Ting (Michael) Yang, Seungwoo Baek, Tanmay Konnur, Zoe Chen, Siyun Qiao, Ziyi Guo, Naarendharan Meenakshi Sundaram, Ben Yang, Samuel Wang, Joanna Fang, Jacklyn Zhu.

I would like to thank all UCLA CHIPS alumni including Prof. Takafumi Fukushima, Dr. Arsalan Alam, Dr. Goutham Ezhilarasu, Dr. Samatha Benedict, Jon Cox, Arpan Dsgupata, Ko-Ching Hou,

Yu-pei (Anne) Huang, Dr. Siva Chandra Jangam, Dr. Faraz Khan, Dr. Kannan Kalappurakal Thankappan, Shelly Ku, Ankit Kuchhanggi, Yongxi Li, Meng-Hsiang (Andy) Liu, Emily MacInnis, Dr. Umesh Mogera, Michael Molter, Dr. Steven Moran, Dr. Sepideh Nouri, Dr. Saptadeep Pal, Harshit Ranjan, Shaurya Seth, Dr. Ujash Shah, Dr. Niloofar Shakoorzadeh, Po-Chang (Steven) Shih, Harshal Sonagara, Eric Sorensen, Dhruv Srinivas, Niharika Tripathi, Pragathi Venkatesh, Arshiya Vohra, Dr. Zhe (Frank) Wan, Yilin (Lenny) Wu, Tianyu Xiang, Dharani Jaya Yakkaluru, Dr. Yu-Tao (Ray) Yang, and Jingxuan Zhu for many successful collaborations and meaningful discussions.

I would also like to thank the staff of UCLA Integrated Systems Nanofabrication Cleanroom, Nanolab Research Facility, and Center for High-Frequency Electronics for their help and support.

I express my deep sense of gratitude to my family including my parents, Jingyue Liu, and Siyu Liu for their never-ending love and moral support. You are the reason I find meaning in everything I do.

VITA

- 2014-2018 B.S. Materials Science and Engineering
Central South University, Hu'nan, China
- 2019 Materials Engineering Intern, CloudKeyz, Inc.
- 2020-2022 Chair, IEEE Student Chapter, UCLA
- 2020 Teaching Assistant, MSE department, UCLA
- 2023 Packaging Intern, Apple Inc.

SELECTED PUBLICATIONS

Ouyang, G., Whang, G., MacInnis, E. and Iyer, S.S., 2021, June. Fabrication of flexible ionic-liquid thin film battery matrix on FlexTrate™ for powering wearable devices. In 2021 IEEE 71st Electronic Components and Technology Conference (ECTC) (pp. 1620-1626). IEEE.

Ouyang, G., Ezhilarasu, G., Sun, H., Ren, H., Yang, Y.T. and Iyer, S.S., 2021, June. A Flexible Power Module for Wearable Medical Devices with Wireless Recharging using Corrugated Flexible Coils. In 2021 IEEE 71st Electronic Components and Technology Conference (ECTC) (pp. 2266-2271). IEEE.

Ouyang, G., Whang, G., MacInnis, E., Ren, H., Sun, H., Irwin, R., Dunn, B. and Iyer, S.S., 2022, May. Fabrication of Flexible Li-ion Battery Electrodes Using " Battlets" Approach with Ionic Liquid Electrolyte for Powering Wearable Devices. In 2022 IEEE 72nd Electronic Components and Technology Conference (ECTC) (pp. 780-785). IEEE.

Ouyang, G., Ren, H., Sun, H. and Iyer, S.S., 2022, August. A thin film and high roughness flexible current collector for high charging/discharging rate flexible Li-ion battery. In 2022 IEEE International Flexible Electronics Technology Conference (IFETC) (pp. 1-3). IEEE.

Ouyang, G., Hanna, A., Benedict, S., Ezhilarasu, G., Alam, A., Irwin, R.W. and Iyer, S.S., 2022. Comprehensive Investigation of In-Plane and Out-of-Plane Die Shift in Flexible Fan-Out Wafer-Level Packaging Using Polydimethylsiloxane. IEEE Transactions on Components, Packaging and Manufacturing Technology, 12(10), pp.1692-1701.

Ouyang, G., Fukushima, T., Ren, H. and Iyer, S.S., 2023, May. 3D flexible Fan-Out Wafer-Level Packaging for Wearable Devices. In 2023 IEEE 73rd Electronic Components and Technology Conference (ECTC) (pp. 601-605). IEEE.

CHAPTER 1 Introduction

1.1 Development of the wearable devices

There has been a surge in wearable devices for health monitoring amplified post-pandemic. Based on the formular and functions, wearables can be divided into three primary categories. The first type, referred to as “rigid”, typically includes devices like smart watches, and earphones [1], [2]. In recent years, these devices have become more mature and popular in the market because of Moore’s Law which enables the miniaturization of the devices. These devices usually incorporate a small rigid device including silicon chips and rigid interconnects and print circuit boards (PCB). To be flexible, wearables are usually equipped with flexible bands, like rubber and textile materials. The relatively high performance of those wearables benefits from the silicon fabrication process. The devices can be operated at up to GHz frequency. However, due to the limited flexibility of the PCB and rubber band approach, this type of device has significant limitations on its application in human body areas where bending or conforming to non-flat surfaces is required.

The second type, “all flexible”, consists of devices made entirely of flexible components, including organic transistors and wiring [3], [4]. This design prioritizes high flexibility and biocompatibility, making it well-suited for direct skin contact and wearable applications that require a gentle and compliant touch. Despite these advantages, the all-flexible type often struggles with low carrier mobility, which hampers electrical performance. This issue is particularly pronounced with p-type flexible transistors [5]. The frequency range of these devices is typically between kHz to MHz. Furthermore, scaling down these components to smaller sizes remains a technical challenge, hindering the development of highly integrated flexible circuits. Therefore, large scale applications using this type of wearable device are still far away.

The third category is a “hybrid” version, also known as flexible hybrid electronics (FHEs) [6], [7], [8]. This approach features small rigid high-performance dies embedded in a flexible or stretchable substrate using advanced packaging, thus allowing for a certain degree of bending and flexing. This type of device manages to deliver high performance akin to rigid silicon-based devices while also providing the adaptability and mechanical compliance of flexible materials. The result is a small form factor that does not sacrifice functionality for flexibility.

Nowadays, FHEs are increasingly prevalent in wearable electronics. Traditional FHEs integrate printed electronics with conventional semiconductor devices, yielding flexible, lightweight, and durable electronic systems. The typical FHE structure comprises a flexible substrate, often made of materials such as polyimide (PI) or polyethylene terephthalate (PET). Conductive traces, printed using conductive inks like silver or copper, form the circuit pathways on this substrate. Rigid components, including integrated circuits (ICs) and sensors, are mounted on the flexible substrate, with protective encapsulation layers applied to shield the electronics from environmental factors such as moisture and mechanical stress.

However, FHE faces several significant challenges. First, the performance and functionality are hindered by large pitch interconnections due to the printing method of fabrication of interconnections. Second, FHE systems often suffer from high interconnect resistance due to the low conductive interconnects materials, which can degrade performance. The use of thin silicon dies, while enhancing flexibility, can lead to lower performance due to increased sensitivity to applied stresses. Additionally, ensuring manufacturing consistency in FHE production processes is challenging, leading to variations in product quality and reliability.

Considering these constraints of traditional FHE methods, FlexTrate™ platform is developed to solve the issues as shown in Figure 1-1 [9]. FlexTrate™ is a die-first Fan-Out Wafer-

Level Packaging (FOWLP) platform designed to achieve high precision and flexibility in electronic packaging [9]. It begins by assembling dies on a thermally releasable adhesive with ~ 1 μm placement accuracy using pick and place technology. The dies are then reconstituted by compression molding with a soft, biocompatible elastomer (PDMS, Silastic MDX4-4210) that cures at room temperature for 24 hours. This process results in less than $6\mu\text{m}$ die-shift across a 100mm diameter wafer due to the low Young's modulus (~ 0.5 MPa) of the molding compound and room temperature curing. Standard Si Back End of Line (BEOL) processes are subsequently used to interconnect the dies with electroplated copper (Cu) metallization at fine interconnect pitches down to 20 μm . FlexTrateTM allows for solderless heterogeneous integration of bare dies at less than 40 μm pad pitches, which is not achievable with conventional flexible technologies. It also supports bending to a 1 mm radius over thousands of cycles, making it suitable for next-generation wearable and implantable applications requiring high-performance flexible systems, such as multi-channel sEMG systems and optogenetics for neural implants. Based on FlexTrateTM, various flexible wearable devices were developed including flexible displays [10], flexible sEMG systems [11], flexible wireless power transfer devices [12], and others [13], [14], [15]. The platform has already demonstrated high-level heterogeneous integration ability, high flexibility, reliability, and compatibility for wearable devices.

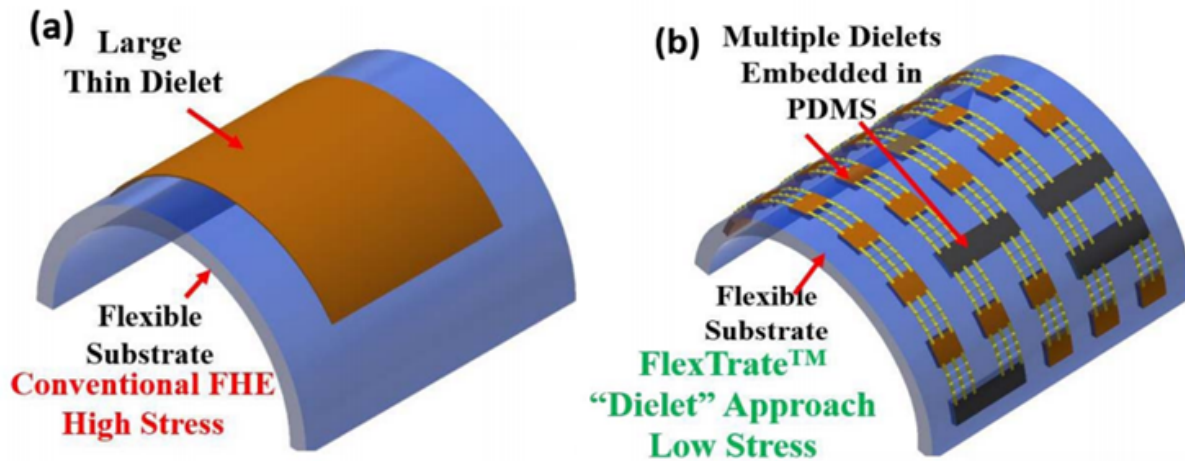


Figure 1-1 Comparison of FlexTrate™ and conventional FHE.

1.2 Needs of a flexible, wireless power supply for wearables

1.2.1 Power consumption analysis of wearable devices

A typical wearable device has three subsystems: sensing, data acquisition and pre-processing, and data storage and data transmission. The sensing system incorporates various types of flexible sensors that have been extensively studied over the past decades. [6], [16], [17], [18]. These sensors can be categorized based on their specific functions as temperature, tactile, optical, electrical, and chemical sensors. In terms of power consumption, these sensors generally consume only a small amount of power during continuous monitoring, typically ranging from nW to tens of μW .

The primary roles of data acquisition circuits include interfacing/readout, signal-conditioning, amplifying, filtering, analog-to-digital conversion, etc. The power consumption of these circuits largely depends on the complexity of the application-specific integrated circuits (ASICs), varying from tens of μW to less than 200 μW .

Alternatively, data storage and transmission components consume significantly more power during operation, which represents a major challenge for the commercialization of wearable

devices. For instance, the power consumption of a microcontroller unit (MCU) is at the mW level, and Low Energy Bluetooth (BLE) requires tens of mW during continuous data transfer due to the high output power needed for effective wireless data transmission [19]. As shown in Figure 1-2, the BLE chip operates at 4.28 ms per event and 7.5 ms per interval. The peak power consumption is 19.8 mW and standby power is less than 1 mW. Over one cycle, the estimated average power consumption is about 12.5 mW, suggesting that an energy budget of 100 mWh (30 mAh at 3.3 V) would allow the system to operate for 8 hours.

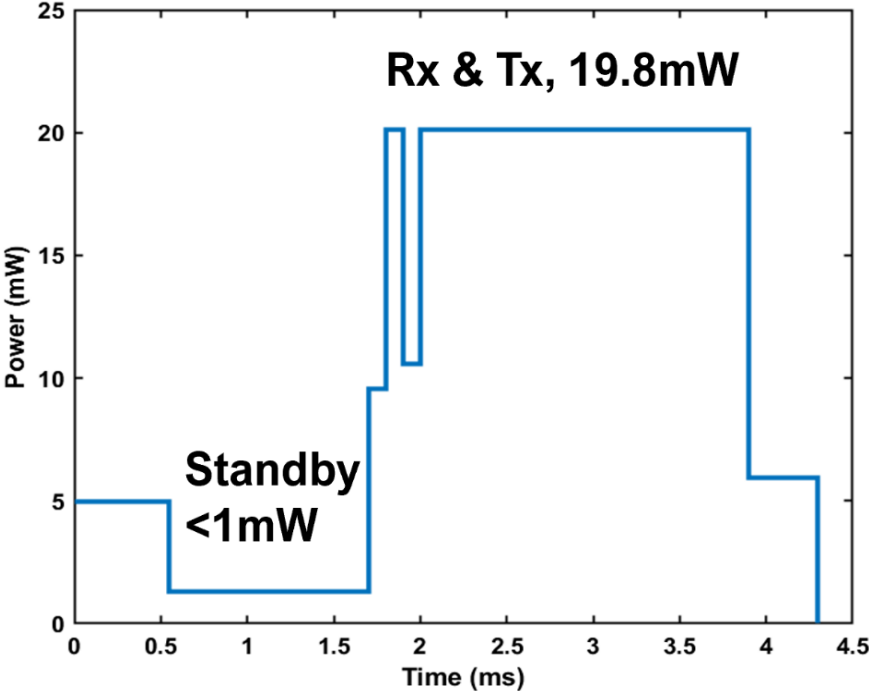


Figure 1-2 BLE nRF52832 operation sequence.

1.2.2 Target specifications of the flexible power solution for wearables

Assuming the surface electromyography (sEMG) device is used for 8 hours every day over the span of one year, and considering that the total available space for the battery within the sEMG device is approximately 20 cm², we can derive the necessary specifications for the battery to effectively power wearable devices as shown in the table Table 1-1.

Table 1-1 Target specs of battery for operation of a sEMG 8 hours per day for a year

Category		Specification	Target
Flexible battery	Electrochemical	Areal Capacity	1 mAh/cm ² @ 3.3 V
		Max output power	1.6 mW/cm ²
		Cycling Life	400 times @ 80% initial capacity (1 yr usage)
	Mechanical and safety	Flexibility	5 mm radius w/ 1000 cycles
		Safety	Non-flammable and high thermal and moist resistance
	Thickness	< 500 μm	

The electrochemical specifications of the flexible battery are pivotal for ensuring consistent performance and longevity. The battery must achieve area capacity of 1 mAh/cm² at a voltage of 3.3 V and the maximum output power of 1.6 mW/cm². These values are critical to ensure that the battery can meet the daily energy consumption of 60 mWh while maintaining efficiency. Moreover, the battery's cycling life is required to withstand 400 cycles at 80% of its initial capacity, aligning with the one-year usage period where the device is utilized daily.

Assuming the surface electromyography (sEMG) device is used for 8 hours every day over the span of one year and considering that the total available space for the battery within the sEMG

device is approximately 20 cm², we can derive the necessary specifications for the battery to effectively power wearable devices.

The electrochemical specifications of the flexible battery are designed to meet the device's power requirements. The battery must achieve an areal capacity of 3 mWh/cm² (1 mAh/cm² at 3.3 V). This value is derived from the total daily power consumption of the sEMG device, which is 60 mWh, divided by the 20 cm² area of the device. Additionally, the battery must provide a maximum output power of 1.6 mW/cm². To ensure long-term usability, the battery should maintain at least 80% of its initial capacity over 400 cycles, which corresponds to daily use over one year.

The mechanical and safety specifications of the battery are also crucial. The battery must exhibit a flexibility that matches the FlexTate™ platform, with a bending radius of 5 mm and the ability to withstand 1,000 bending cycles. This level of flexibility is necessary to maintain performance in wearable applications. Safety requirements include non-flammability and high resistance to thermal stress and moisture, ensuring safe operation in various environments. Additionally, the battery's thickness should be less than 500 μm to integrate smoothly into the compact design of wearable devices.

1.3 Issues of present power supplies for wearables

The target specifications discussed in the last section underscore the necessity for a highly efficient, durable, and safe power supply to fulfill the power requirements of wearable technologies, particularly sEMG devices as an example.

Nowadays, the reported power supplies for wearables include solar cells, NFC, triboelectric devices, thermal-electric devices, supercapacitors, batteries, etc. Solar cells convert sunlight into electrical energy, offering a renewable and environmentally friendly power source; however, their efficiency is limited by the availability of light and dependence on external

environmental conditions leading to a poor output stability. Near Field Communication (NFC) devices facilitate wireless power transfer over short distances, allowing for convenient and cable-free charging; yet, they require proximity to a compatible transmitter, which limits their practicality for continuous power supply. Triboelectric devices generate electricity through contact and separation between different materials, providing an innovative way to harness mechanical energy from everyday movements; but their output is often inconsistent, low, and dependent on the wearer's activities. Mechanical-electric devices harness mechanical energy from motion, such as walking, and can generate power without the need for an external energy source; however, they can be bulky and may not provide a steady power output. Thermal-electric devices convert body heat into electricity, leveraging the constant heat generated by the human body; still, their efficiency is relatively low and depends on the temperature difference between the body and the environment. Supercapacitors store energy electrostatically and deliver rapid bursts of power, featuring fast charging and discharging cycles; nonetheless, they have lower energy density compared to batteries, making them less suitable for long-term use.

Batteries provide a reliable and continuous power source, which is essential for the sustained operation of wearables, ensuring that these devices can function consistently without frequent interruptions for recharging. This reliability makes batteries a crucial component for applications that require constant power, such as health monitoring, fitness tracking, and other continuous data collection tasks. However, the integration of batteries in wearable devices often presents several challenges.

One major challenge is flexibility; traditional batteries are typically rigid and bulky, making them difficult to incorporate into the flexible, lightweight, and compact designs of wearable

technology. This rigidity can hinder the comfort and usability of wearables, which are designed to be worn on the body and must accommodate a wide range of movements.

In designing flexible batteries, considerations should also extend beyond power consumption to include the form factor, flexibility, safety, and integration requirements. For instance, the thickness of present wearable devices has been reduced to hundreds of microns [20], [21], [22]. However, traditionally used coin cell batteries, such as type 2032 with a total thickness of 2 mm, have not undergone similar miniaturization as electronic components. Consequently, the final thickness of the integrated system is often constrained by the battery size. Additionally, traditional battery formats lack the flexibility required by the devices they power, undermining the potential benefits of wearable technologies. It is also important to note that, given the energy density of typical battery materials, the size of the batteries must be several times larger than the dies [23], [24]. Moreover, the connection pads of present batteries are not designed for flexible packaging and typically require additional wires or connectors for integration.

Since the traditional batteries are not intrinsically flexible, researchers in the past few decades have developed various types of flexible batteries, including pouch cell batteries [34], rubber-like batteries [35], [36], [37], 1D fibrous batteries [38], [39], [40], etc. Pouch cell batteries are a relatively mature technology in the battery market. While they exhibit some degree of flexibility, they are limited to a bending radius of ~ 20 mm. In addition, pouch cell batteries typically contain flammable organic electrolyte, presenting serious safety concerns for wearable devices. Beyond flammability concerns, other issues, including swelling, leakage, and lack of biocompatibility, limit the application of pouch cells in wearable devices [41]. Other formats such as rubber-like batteries, utilize crosslinked rubber-based polymers to fabricate cathode, anode, and electrolyte, and offer a route for flexible batteries. While this approach provides intrinsic flexibility

and stretchability, the ionic conductivity of the electrolyte remains low, resulting in low output power and high internal resistance [34], [42]. 1D fibrous batteries are another emerging type of batteries for wearable devices. Typically, fibrous cathodes and anodes are weaved together to create a single-thread full cell battery. This type of 1D batteries can also be woven as a cover for the devices, but with major limitation in energy density and output power density.

In addition to the flexibility of the battery, safety is another significant concern. Batteries, especially those based on lithium-ion technology, can pose risks of overheating, leakage, or even combustion if not properly managed. Ensuring the safety of batteries in wearable devices is paramount, as these devices are in close contact with the skin and often used in diverse and sometimes harsh environmental conditions.

To achieve a fully wireless wearable device, which incorporates modules for data acquisition, data processing, and data transmission, along with a power source such as a button battery, a flexible wireless charging module is required to charge the button battery. However, considering the transmission efficiency, device size, and safety, the wireless charging module, and lithium-ion battery cannot be integrated into the same plane with sensors and other close to the human skin due to a few reasons [66], [67], [68], [69]. First, the wireless charging module will reduce the energy conversion efficiency of the coil if it is in a position close to the skin. Second, wireless charging modules and battery modules are large area and volume devices, usually accounting for more than 50% of the total device volume. Finally, considering the safety of lithium-ion batteries, the batteries themselves should not be placed close to the skin to prevent burning.

Addressing these challenges involves ongoing research and development to create batteries that are not only flexible and safe but also durable enough to meet the demands of wearable

technology. Innovations such as flexible battery materials, solid-state electrolytes, and advanced packaging techniques are being explored to overcome these obstacles and enhance the performance of batteries in wearable applications.

1.4 Introduction to FlexPower

1.4.1 Flexible battlet Li-ion battery and flexible wireless charger

To overcome these issues in present designs of flexible batteries, we implemented the dielet method in wearable electronics packaging to design and fabricate a flexible Li-ion battery known as battlet [15], [43], [44]. The battlet approach explodes a single large electrode into a small cell matrix and flexibly interconnects the cells on a flexible substrate PDMS as shown in Figure 1-3. In addition, to address the safety concerns of the Li-ion battery for wearables, an ionic liquid electrolyte is used. Ionic liquids are room temperature molten salts which exhibit wide electrochemical stability window (0V - 5V), excellent thermal stability, and nonflammability owing to their low vapor pressure [45], [46], [47], [48], [49]. Thus, ionic liquid electrolytes present a number of advantages over traditional organic electrolytes for powering wearable devices.

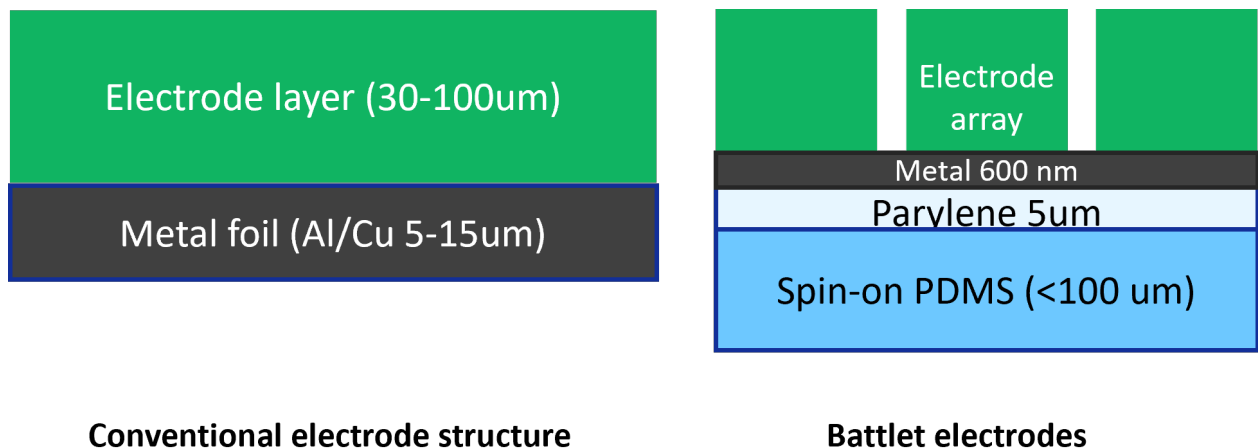


Figure 1-3 Structure comparison of the conventional electrode on metal foil current collector and battlet electrode on flexible metal-sputtered current collector.

Considering the materials properties of the components as shown in Figure 1-4. this battlet design can significantly reduce the stress concentration of the electrode during bending with conventional electrode materials and fabrication methods.

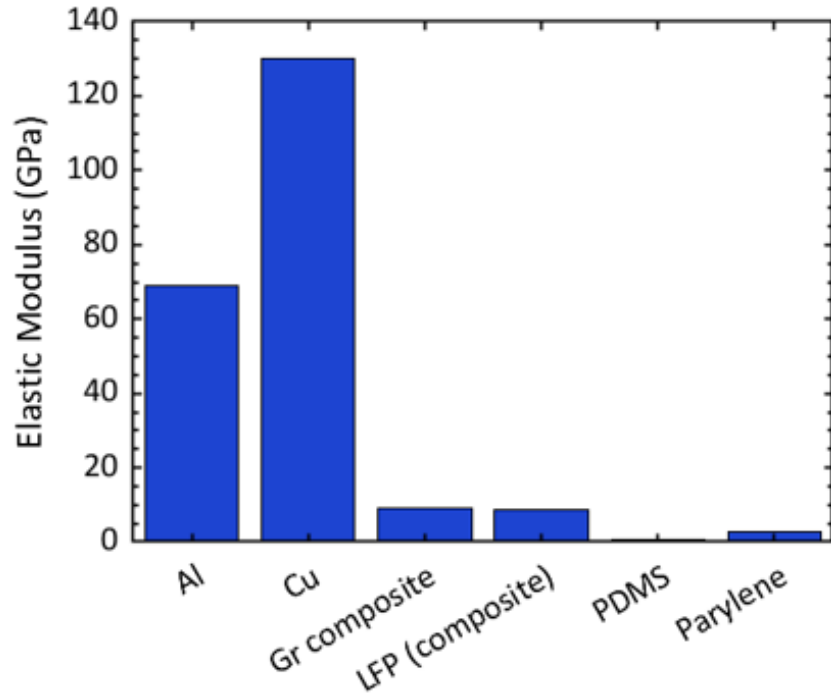


Figure 1-4 Young's modulus of the materials used in this work.

Figure 1-5 (© 2024 IEEE) shows the exploded view of the battlet battery structure. The top and bottom PDMS is as a substrate and sealing. The cathode battlet and anode battlet are aligned and separated by a glass fiber separator. In addition, a double side polyimide tape ring is placed on the edge of the electrode as an electrolyte reservoir. Ionic liquid with additive (PYR₁₄FSI + LiFSI + 5% Vinylene Carbonate) is used as the battery electrolyte.

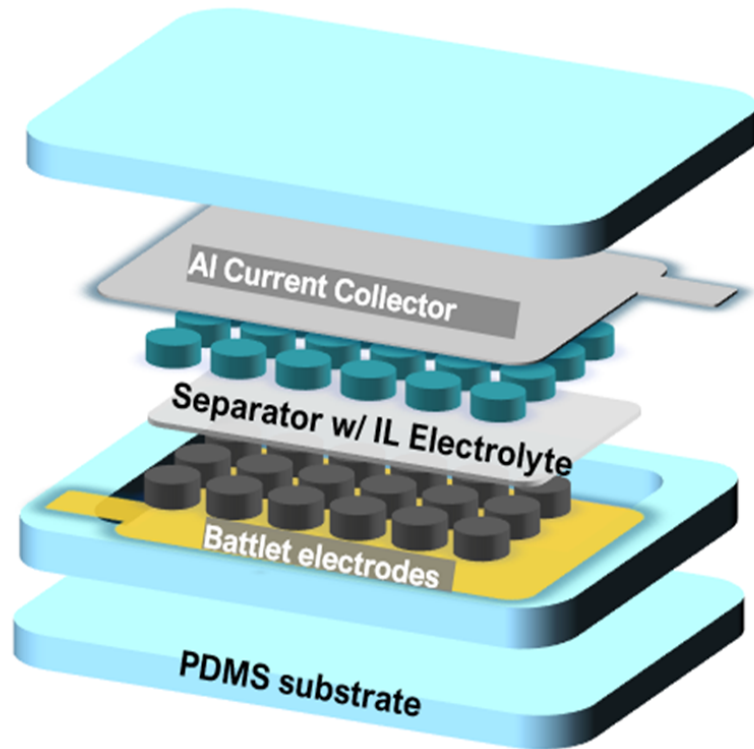


Figure 1-5 Exploded view of the battlet flexible battery: rounded-corner electrode array is on the metal current collector and on flexible PDMS substrate.

To wirelessly charge the battlet battery, a wireless charging module is required on the FlexTrate™. Conventional wireless charging modules often incorporate rigid, bulky, and non-biocompatible materials, which present a stark contrast to the low Young's modulus and compact design of FlexTrate™. The disparity in modulus and form factor between the solid-state charging modules and wearable technology restricts their application.

To address these issues, a flexible wireless charging module is also developed on FlexTrate™ platform. Based on previous designed resonant magnetic wireless power transmission (WPT) [12], the design is optimized for charging the battlet battery (LFP/Graphite system) at an optimal frequency of 13.56 MHz. In this work, a thin, highly flexible resonant magnetic wireless power transfer link for Li-ion battery charging was developed on the FlexTrate™ platform [10],

[65]. This device integrates commercially available components with a resonant magnetic coupling coil and achieves a 3.3 V output for wireless charging. The device's maximum charging power reached 3.97 mW with 5 V V_{pp} at 13.56 MHz input for a commercial Li-ion coin cell battery, and maintains performance without degradation after 1000 bending cycles at a 5 mm radius, demonstrating its potential for integration into flexible wearable technology.

The schematic view of the wireless charger and design are shown in Figure 1-6 (a) and (b) (© 2024 IEEE). In this design, there are 8 dies embedded in the PDMS including deep trench capacitors, LDO, and diodes. The total size of the wireless charger is 3.5 cm² with 4 turns of the coil. The total thickness of the charger is 500 μm. The charger is designed to work at 13.56 MHz with 3.3 V output voltage while charging the battery.

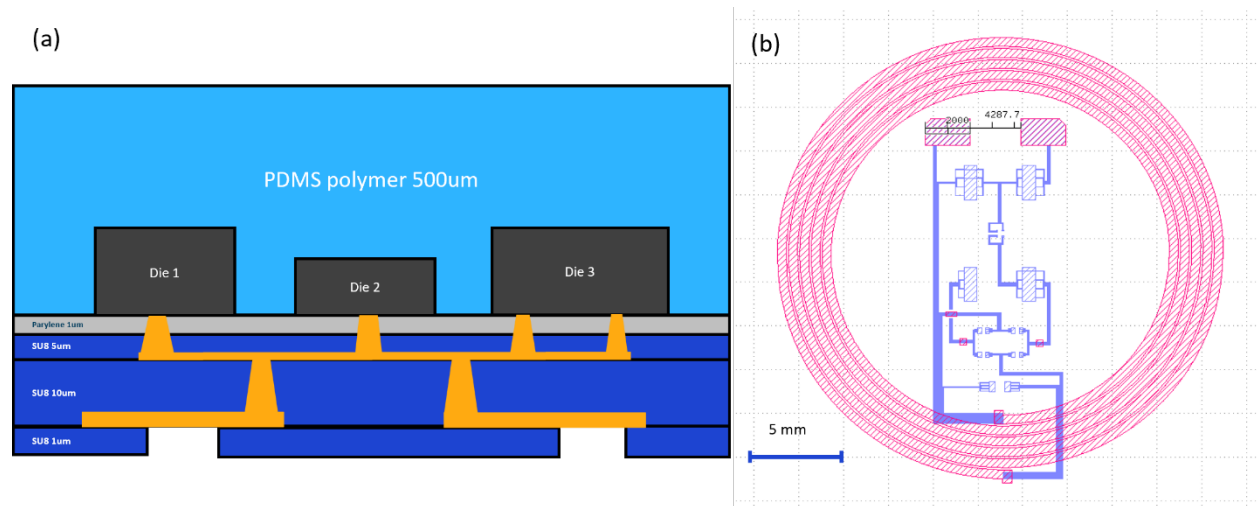


Figure 1-6 (a) schematic view of the flexible wireless charger using flexible Fan-Out Wafer Level Packaging; (b) layout of the wireless charger based on the circuit design.

1.4.2 Integration of the flexible battery and wireless charger on FlexTrate™

For the integration of the flexible battery and wireless charger, we have implemented both 2D and 3D approaches as demonstrations of FlexPower's capabilities as shown in Figure 1-7.

Figure 1-7 (a) (© 2024 IEEE) shows the schematic view of the 2D integration. In the 2D integration

approach, a microLED array is transferred to and interconnected on the FlexTrate™ platform, where both the flexible wireless charger and the flexible Li-ion battery are integrated with the LEDs on the same wiring level using low-temperature solder. In the 3D integration approach, we propose a 3D FOWLP structure that incorporates through-glass via dies (TGVs). This innovative structure enables flexible interconnections of the battery and wireless charger on the backside of wearable devices, with TGVs facilitating power delivery from the back to the front side. This 3D FOWLP structure offers a pragmatic solution for optimizing the integration and functionality of power components in wearable technology.

The microLED array is molded in the 1st layer PDMS and the light goes through the bottom of the 1st layer PDMS. The flexible wireless charger and the flexible Li-ion battery are integrated with the LEDs on the same wiring level using low temperature solder. Figure 1-7 (b) is the schematic view of the flexible 3D FOWLP for wearables. The 1st PDMS layer is the wearable devices using FlexTrate™ technology, and the second layer is the power supply including the flexible batteries and flexible wireless charger. The two layers are interconnected by a through-glass via die.

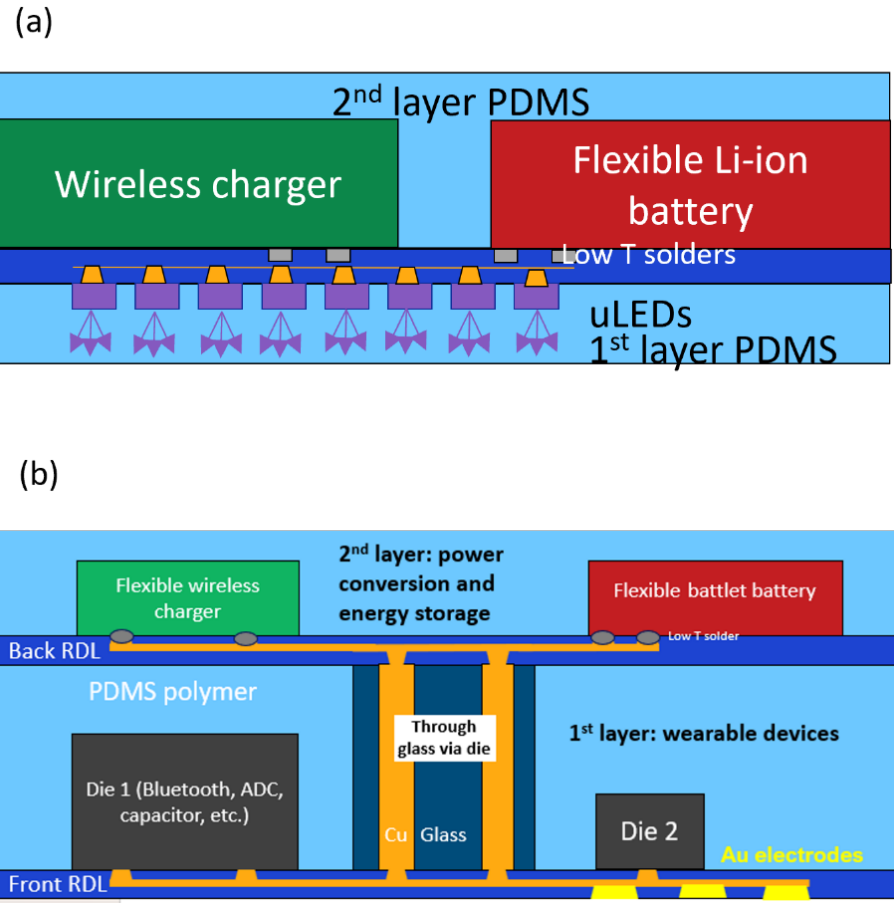


Figure 1-7 (a). schematic view of the flexible 2D FOWLP for wearables. (b). schematic view of the flexible 3D FOWLP using through-glass vias for wearables.

1.5 Contributions of the work

This dissertation contributes to the field of flexible power solutions for wearable devices through several key advancements and innovations:

Mechanical Failure Analysis of Conventional Batteries: This work provides a comprehensive analysis of the mechanical failure modes in conventional planar batteries when subjected to the dynamic and flexible environments required for wearable devices. It identifies key issues such as crack formation in brittle electrode materials and current collectors, and delamination due to poor adhesion between material layers. These failures result in a loss of

electrical conductivity and compromised electrochemical performance, underscoring the need for enhanced flexibility and mechanical resilience in battery design.

Development of Flexible Battlet Li-ion Battery with Ionic Liquid Electrolyte: The research introduces a novel flexible Li-ion battery, termed "battlet," which features a segmented cathode and anode array on flexible composite current collectors. This design reduced the bending stress concentration on conventional battery electrode during bending and addresses the mechanical failure issues in conventional planar electrode including crack formation and delamination. The flexible battery demonstrated enhanced electrochemical stability, maintaining a capacity density of 0.7 mAh/cm² and enduring 1000 bending cycles at a 5 mm bending radius. Additionally, the incorporation of ionic liquid PYR₁₄FSI as the electrolyte improves the safety of the flexible battery and mitigates flammability concerns associated with traditional organic electrolytes, thereby enhancing the battery's overall safety for wearable applications.

Flexible Wireless Charging Technology: Leveraging the flexible Fan-Out Wafer-Level Packaging (FOWLP) platform, the dissertation develops a flexible wireless charger based on the magnetic resonance method. This charger can deliver a consistent 3.3 V output voltage and 3.9 mW peak power, and it maintains functionality after repeated bending with a 5 mm radius. This innovation provides a reliable wireless power solution, eliminating the need for physical connectors and enhancing the convenience of wearable devices.

Integration of FlexPower with Wearable Devices: This work explores both 2D and 3D flexible integration approaches to incorporate the FlexPower system with wearable electronics on the FlexTrate™ platform. In the 2D approach, the FlexPower system powers a 33 UV microLED display array, demonstrating the feasibility of powering flexible electronics. The 3D integration approach involves developing interconnects on both sides of the FlexTrate™, utilizing through-

glass via technology, and implementing an SF₆/O₂ plasma PDMS dry-etch method for backside contact opening.

1.6 Organization of the dissertation

The remainder of this dissertation is organized as follows and Figure 1-7 shows the organization of chapter 2 to chapter 4:

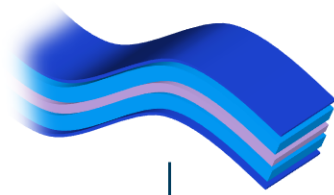
Chapter 2 discusses a battlet Li-ion battery with high flexibility, high safety, good electrochemical performance, and reliability. The chapter analyzes the mechanical failure of conventional electrodes during flexing, the concept of battlet, and fabrication approaches. The results of morphological, electrochemical performance, and reliability are discussed in detail.

Chapter 3 demonstrates a flexible wireless charger based on FlexTrate™, adapted and optimized from a previously developed wireless power transfer device. The electrical, topological, and mechanical results are discussed in this chapter.

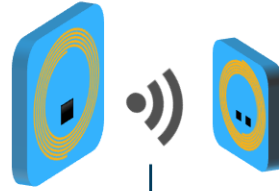
Chapter 4 discusses two integration approaches for the flexible battery and the flexible wireless charger, including 2D and 3D approaches. For the 2D approach, a flexible battery and wireless charger are integrated with a microLED array based on the FlexTrate™ platform as a demonstration. In the 3D approach, the fabrication processes are discussed using through-glass via dies, and a PDMS dry etch method is described.

Chapter 5 presents a summary of the dissertation. Future work and potential research directions are also proposed based on present research.

1. Flexible "battlet" Li-ion Battery

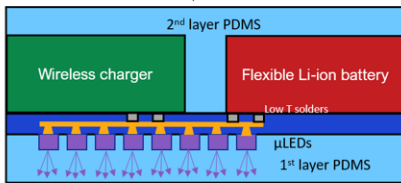


2. Flexible wireless charger



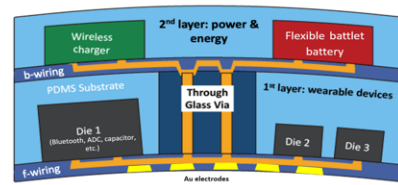
3. Integration

2D integration with μ LEDs



Powering flexible μ LED display

3D integration using TGVs



Powering flexible sEMG with TGVs

Figure 1-8 Organization of the work

CHAPTER 2 Development of flexible battlet Li-ion battery

In this chapter, the theoretical analysis of various failure models of battery electrodes is first presented. Following this analysis, a battlet electrode structure is proposed to enhance the flexibility of the electrode. To fabricate battlets, a screen – printing method is discussed. Detailed discussions on the morphology of the electrodes, as well as their mechanical performance, electrochemical performance, and reliability are provided in this chapter.

2.1 Failure analysis of battery electrodes during bending

2.1.1 Single layer model - definition of flexibility

Consider a thin film with thickness h and length πr_b , as shown in Figure 2-1. When the film is bent to a radius r_b , the outer length increases to $\pi(r_b + \frac{1}{2}h)$, while the inner length decreases to $\pi(r_b - \frac{1}{2}h)$. Therefore, the strain at the outer or inner surface can be expressed as:

$$\varepsilon = \frac{\text{outer (or inner) surface} - \text{neutral plane}}{\text{neutral plane}} = \frac{\pi(r_b \pm \frac{1}{2}h) - \pi r_b}{\pi r_b} = \frac{h}{2r_b}$$

Since strain ε is defined as $\varepsilon = \frac{\sigma}{E}$, it follows that:

$$\frac{1}{r_b} = \frac{\sigma}{E} \times \frac{2}{h}$$

If the materials fracture upon reaching its yield strength σ_y , then the minimum bending radius is:

$$\frac{1}{r_{bmin}} = \frac{\sigma_y}{E} \times \frac{2}{h}$$

Therefore, we can define the bendability f of the materials as:

$$f = \frac{1}{r_{bmin}} = \frac{\sigma_y}{E} \times \frac{2}{h}$$

Additionally, the flexibility form factor $f_{fom} = \frac{\sigma_y}{E}$ only depends on materials properties [25].

It is evident from the equation that reducing materials thickness h or selecting materials with a low Young's modulus can enhance flexibility. For instance, glass fibers achieve considerable flexibility when thinned down to 250 μm , and silicon film thinned down to 200 μm .

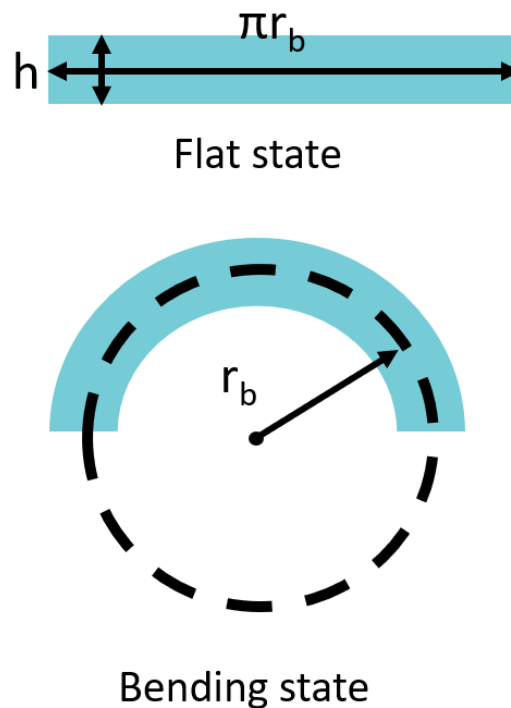


Figure 2-1 Single layer bending model.

2.1.2 Double layer model – cohesive and adhesive stress on the electrode

The single layer model in the previous section is an ideal model, which assumes that:

- (1) the material has isotropic properties across the layer.
- (2) freestanding boundary conditions, no fixed or confined edge or corners of the model.

(3) and a failure mode where the bending stress σ_b is less than its yield stress σ_y , according to the maximum principal stress theory.

However, battery electrodes typically consist of two different layers: the current collector (usually Al or Cu) and the composite electrode material. To better approximate the real scenario of bending a battery, a double-layer model is defined. The top layer thickness is h_{top} and the top layer Young's Modulus E_{top} . The bottom layer thickness is h_{bottom} . The bottom layer Young's Modulus is E_{bottom} . The total thickness of the layer is h and when bent to a radius r_b , the stress and strain expressions for the top and bottom layers are similar to the single-layer model:

$$h = h_{top} + h_{bottom}$$

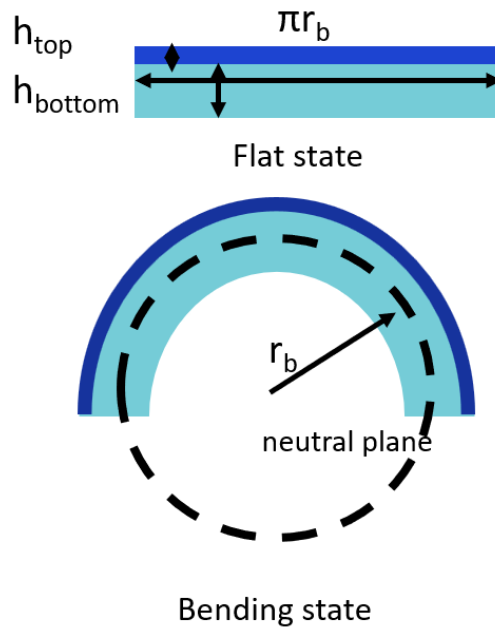


Figure 2-2 double layer model.

The expression for strain and stress of top/bottom layer surface are similar to the single layer model:

$$\epsilon_{top/bottom\ surface} = \pm \frac{(h_{top} + h_{bottom})}{2r_b}$$

The top surface is tensile strain, which is positive, while the bottom surface is native compressive strain. The stress at the top surface is

$$\sigma_{top/bottom\ surface} = E_{top/bottom} \cdot \varepsilon_{top/bottom\ surface}$$

Additionally, the strain at the interface is:

$$\varepsilon_{interface} = \frac{h_{bottom} - h_{top}}{2r_b}$$

At the interface, stress should be evaluated separately for the top and bottom sides:

Top side stress at the interface:

$$\sigma_{inter-top} = E_{top} \cdot \varepsilon_{inter}$$

Bottom side stress at the interface:

$$\sigma_{inter-bottom} = E_{bottom} \cdot \varepsilon_{inter}$$

It shows that at the interface, the stress on the bottom layer side depends on the bottom materials Young's modulus where the stress on the top layer depends on the top materials Young's modulus. The stress difference between the two layers creates shear stress at the interface, which is the region of adhesion between the 2 layers. When the shear stress is greater than the adhesion stress between the adhesion force, layers delaminate.

In summary, the single layer and the double layer theoretical models define the flexibility of electrode materials, analyze the stress distribution within the electrode layer during bending, and identify typical failure mechanisms, including cohesive and adhesive failures. In the subsequent section, a more realistic model will be examined, where the typical failure mechanisms and their impact on battery performance will be further analyzed.

2.1.3 Failure analysis of conventional planar battery electrodes

Conventional flexible batteries employ large planar anodes and cathodes consisting of two layers as shown in Figure 2-3: an active materials layer and a metal collector film layer [26], [27], [28], [29]. The current collector is approximately 5 -15 μm thick, while the active layer thickness ranges from 20 -80 μm . The active layer which is porous has a polymer binder (e.g., Polyvinylidene Fluoride, PVDF), active material powder (e.g., LiFePO_4 for the cathode, and graphite for the anode), and conductive additives (e.g., carbon black).

The bonding forces within the electrode can be categorized into adhesive and cohesive types [30]. The cohesive force at the electrode/current collector interfaces is primarily governed by the Van der Waals forces between the PVDF and the metal surface. Other interactions include Van der Waals forces between PVDF and particles, chain entanglement among PVDF molecules, and metal bonds within the current collector layer. Generally, the adhesive strength hierarchy is as follows: PVDF-PVDF interactions are stronger than PVDF-particle interactions, which in turn are stronger than PVDF-metal interactions.

As a result, the mechanical performance—particularly in terms of flexibility and bendability—depends significantly on the adhesion force and the mechanical strength between the electrodes and current collectors. This relationship is crucial for maintaining the structural integrity of the battery under mechanical stress [31], [32], [33].

Conventional battery electrode at bending state – e.g. LiFePO_4

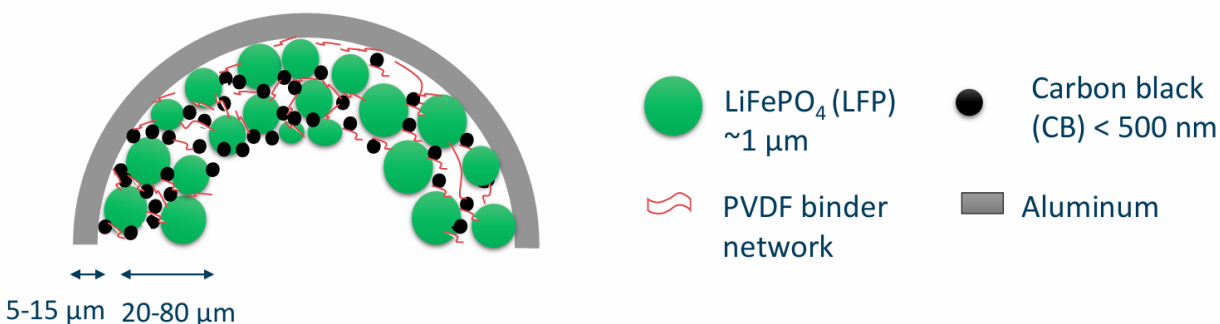


Figure 2-3 Conventional LFP cathode coated on Al metal current collectors at bending state.

Figure 2-4 depicts the progress of conventional planar electrode failure over mechanical bending cycles. And Figure 2-5 (© 2021 IEEE) depicts the SEM images of a planar LFP electrode in 1000 cycles at 5 mm bending radius. Initially, as shown in Figure 2-4 (a) and Figure 2-5 (a) due to the low mechanical strength of the PVDF to PVDF Van der Waals bonding and chain entanglement in the electrode layer, cracks form and propagate on the surface of the electrode. It will increase the nonuniformity of electrode surface, thus leading to over lithiation and faster dendrite growth on the surface of electrode. As a result, the dendrite will shorten the battery internally. Furthermore, as shown in Figure 2-4 (b) Figure 2-5 (b) as the number of bending cycle increases, cracks will reach to the interface between electrode current collector layer, then propagate along the interface, causing the delamination of electrode layer. The delamination increases the contact resistance between the electrode and current collector, thus contributing to the increase of internal resistance of the full battery. In the third stage Figure 2-4 (c) and Figure 2-5 (c), the LFP layer completely peels off from the aluminum current collector, resulting in a significant decrease in battery capacity. Eventually as shown in Figure 2-4 (d) and Figure 2-5 (d),

due to metal fatigue, the aluminum film begins to fracture, thus leading to connection issues with the external circuit rendering the battery inoperative.

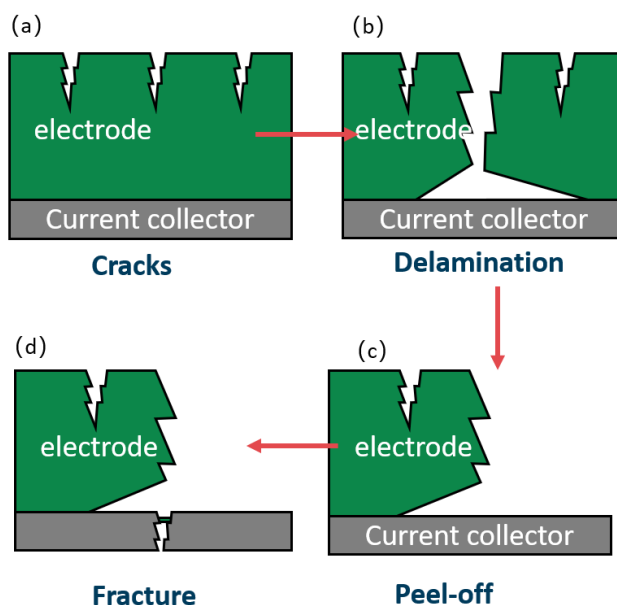


Figure 2-4 Major failure mechanisms of flexing conventional planar battery electrodes. (a) Crack formation and propagation; (b) electrode layer delamination; (c) electrode layer peel-off; (d) Metal current collector failure.

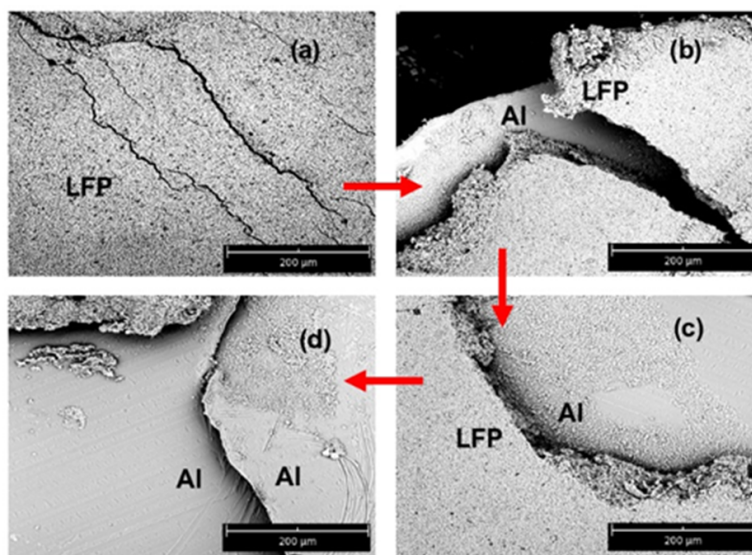


Figure 2-5 Four of failure modes of conventional planar LFP cathode during mechanical bending cycles: (a). Crack on LFP film; (b). Delamination between LFP and Al current collector; (c). LFP layer peels off from Al current collector; (d). Fracture on Al current collector.

2.2 Geometrical analysis of the battlet

2.2.1 Circular design

Two battery matrix shapes are discussed in this work. The first is the circular shape as shown in Figure 2-6. The calculated filling factors of this design is shown in Figure 2-7. This circular design utilizes about 30-40 % area of the whole area of the substrate.



Figure 2-6 Experimental design comparing different electrode radii and stacking configurations.

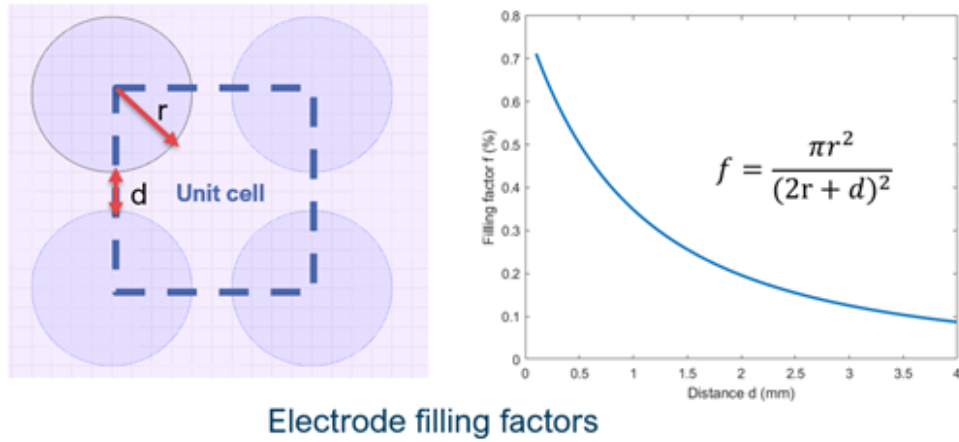


Figure 2-7 Calculation of the filling factor for the circular electrode shape design.

The disk radius is from 0.5 mm – 2 mm, and the disk distance is in the range of 1-2 mm. The total area of each design is about 4 cm² electrode array. In Figure 2-8, it shows the optical images of the sample after laser-cutting. The all design shows clean and shape edge. The black dusts are carbonized PDMS after laser cut due to high temperature.

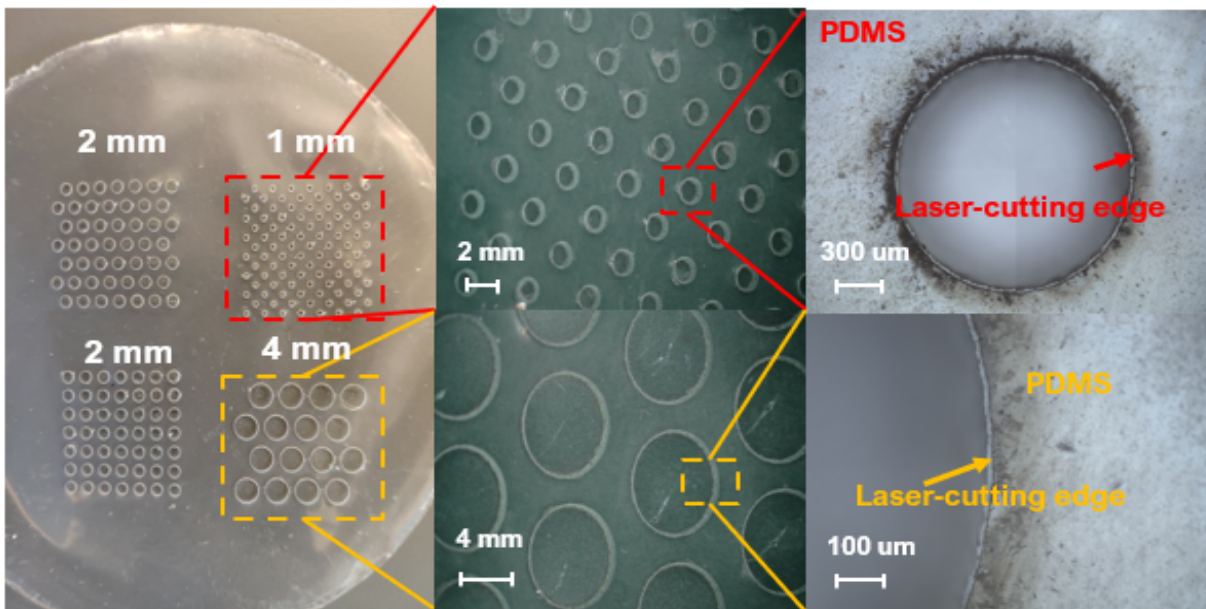


Figure 2-8 Optical images of PDMS after laser-cut using various circular shape layout.

2.2.2 Rounded corner square design

To further increase the energy density of the battery, the second battery matrix rounded corner is shown in Figure 2-9. The corner radius is 0.5 mm while the length of the square is 2 mm. The cell distance is 0.2 mm, thus giving a filling factor ~80%.

Figure 2-10 presents optical images taken after laser cutting of PDMS. Due to the size of the laser beam, which is approximately 30 μm , the PDMS stencil distances have been optimized down to 200 μm . Distances smaller than 100 μm encounter issues with over-cutting due to excessive heating. Reducing the laser power to avoid this issue leads to another problem: if the power is too low, the laser cannot completely cut through the sample, compromising the quality of the desired laser-cut sample. In addition, we also noticed that for the PDMS stencil cell spacing smaller than 400 μm (as shown in Figure 2-11). Electrodes are likely to merge after printing, which limits the spacing larger than 400 μm .

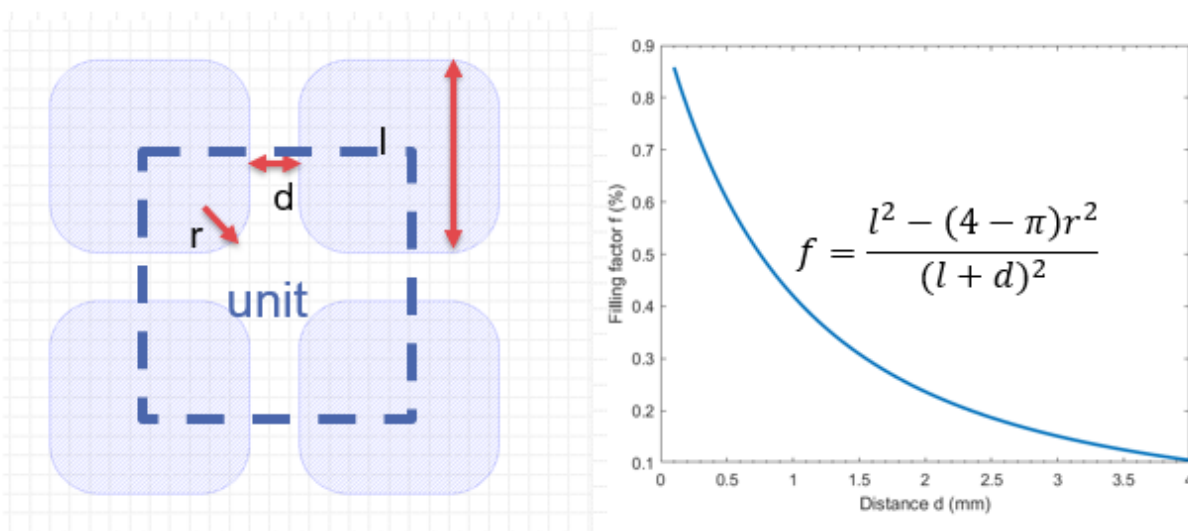


Figure 2-9 Calculation of the filling factor for the rounded corner electrode shape design

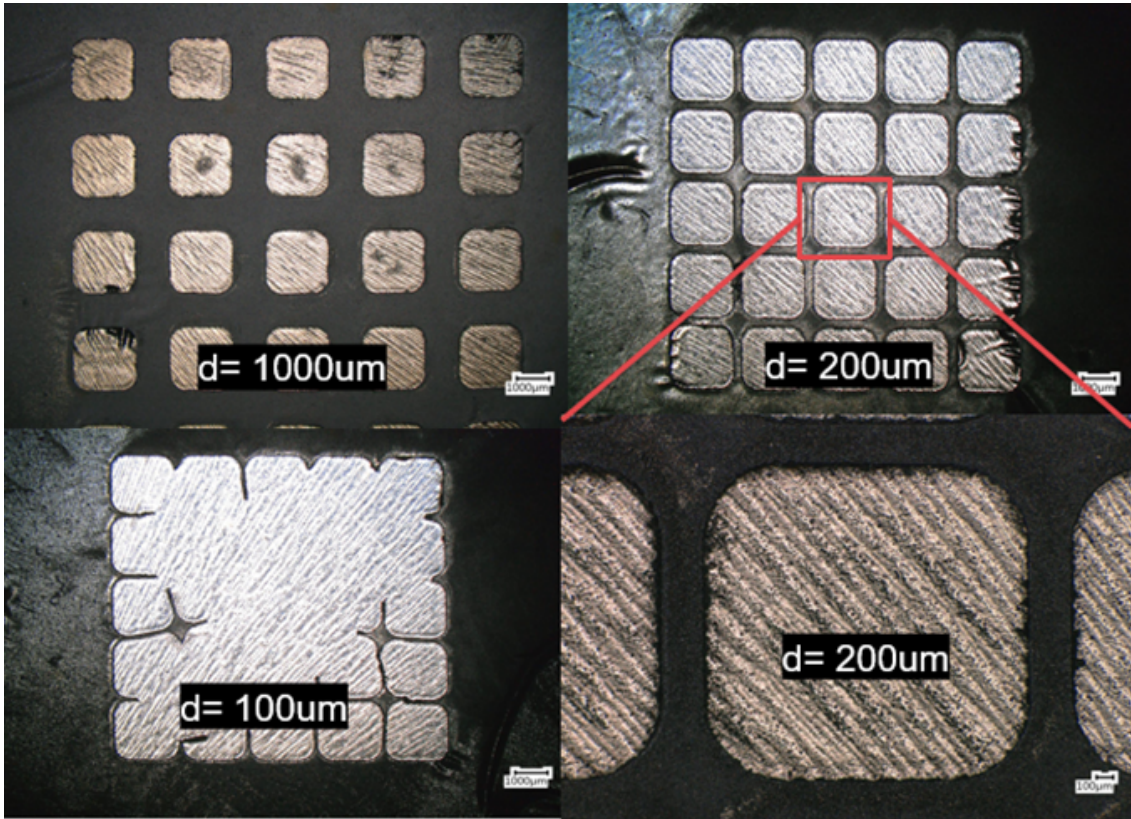


Figure 2-10 Optical images of PDMS after laser-cut using various rounded corner shape layout from 1 mm spacing distance to 100 μm spacing distance.

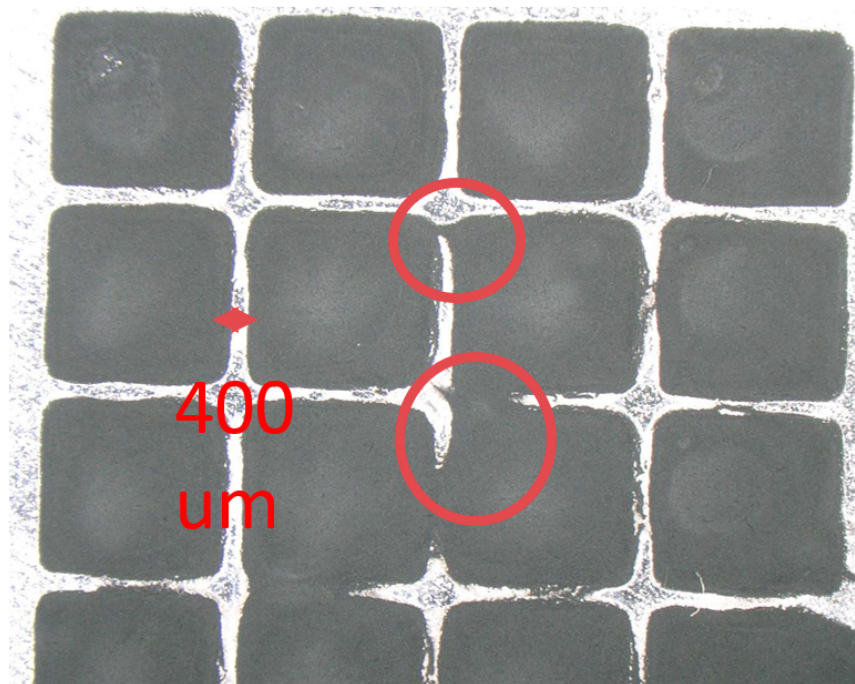


Figure 2-11 When cell spacing is 400 μm , battlets are likely to merge.

2.3 Modeling of battlet flexibility

2.3.1 Comparison of the flexibility of planar electrode and battlet

The bending stress and strain of conventional planar electrodes and battlets are studied using ANSYS Mechanical (version 21R1, 2D) as shown in Figure 2-12. For the planar electrode, the thickness of LFP is 50 μm , and the thickness of the Al current collector is 10 μm . For the battlet cell, the LFP electrode size is 2.5 mm with a spacing of 0.5 mm. The electrode thickness is the same as that of the planar electrode, which is 50 μm . The flexible current collector consists of three materials: Al (0.6 μm), parylene (5 μm), and PDMS (100 μm). The material properties are as follows: the Young's modulus of Al is 69 GPa, LFP is 8.5 GPa, parylene is 2.8 GPa, and PDMS is 2 MPa. In the Ansys simulation, these two models are applied with a force on the surface of the electrode to conform to a 5 mm radius rod to simulate the bending status.

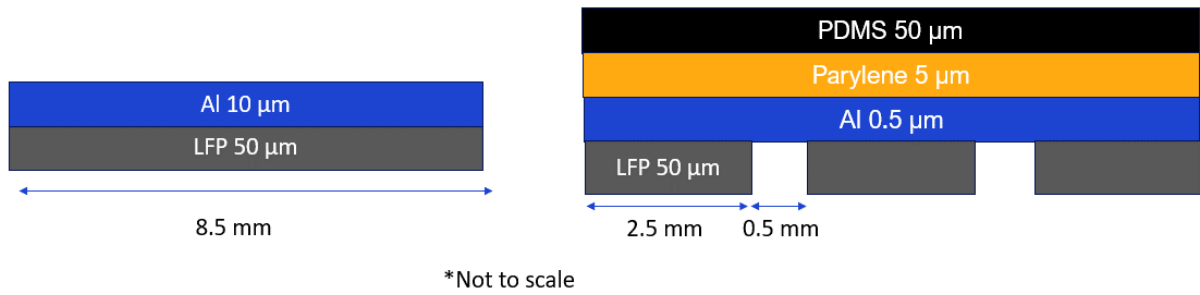


Figure 2-12 Ansys model of a planar electrode and a battlet electrode.

Figure 2.15 shows the stress and strain plot of the planar electrode at a 5 mm bending radius. During bending, the current collector experiences tensile stress, while the LFP layer undergoes compressive stress. The neutral plane lies within the electrode layer. The current collector layer has a higher bending stress than the electrode layer due to the high Young's modulus of aluminum. According to the stress plot, the maximum stress is 264 MPa on the surface of the aluminum current collector layer and approximately 60 MPa on the surface of the electrode. Stress is distributed evenly across the planar electrode structure.

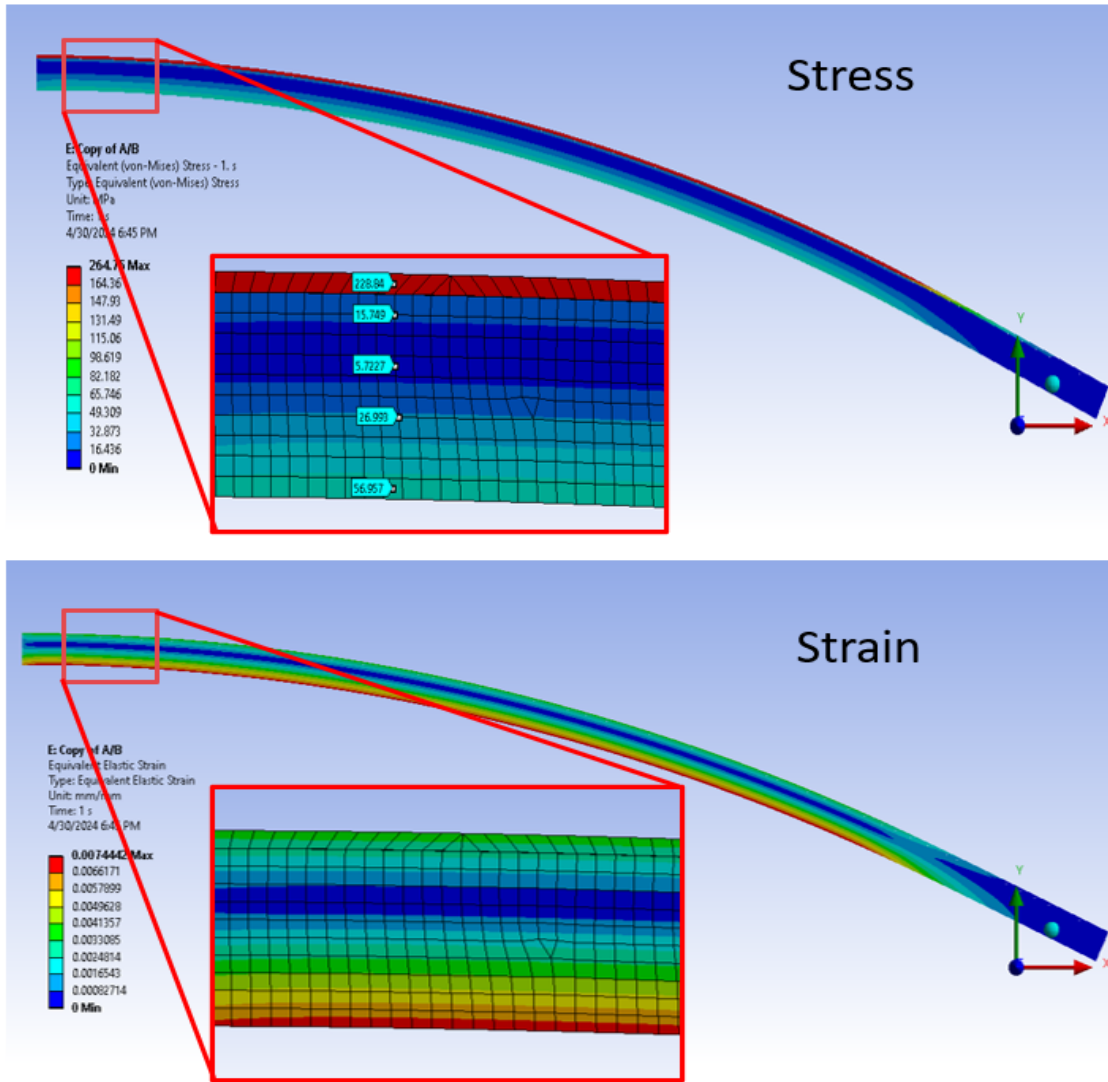


Figure 2-13 Strain and stress plot of planar electrode at 5 mm bending radius.

Figure 2-16 shows the stress and strain plot of the battlet electrode. It differs from the planar electrode under bending conditions. For the battlet, the maximum strain occurs on the surface of the current collector at the spacing between the battlet electrodes. The stress plot indicates that the maximum stress is 223 MPa on the surface of the spacing, while the stress on the LFP battlet is negligible. The strain and stress on the battlet are not significant because the battlet design reduces the deformation of the electrode during bending. Additionally, the flexible current collector deforms more due to its lower Young's modulus compared to the battlet electrode.

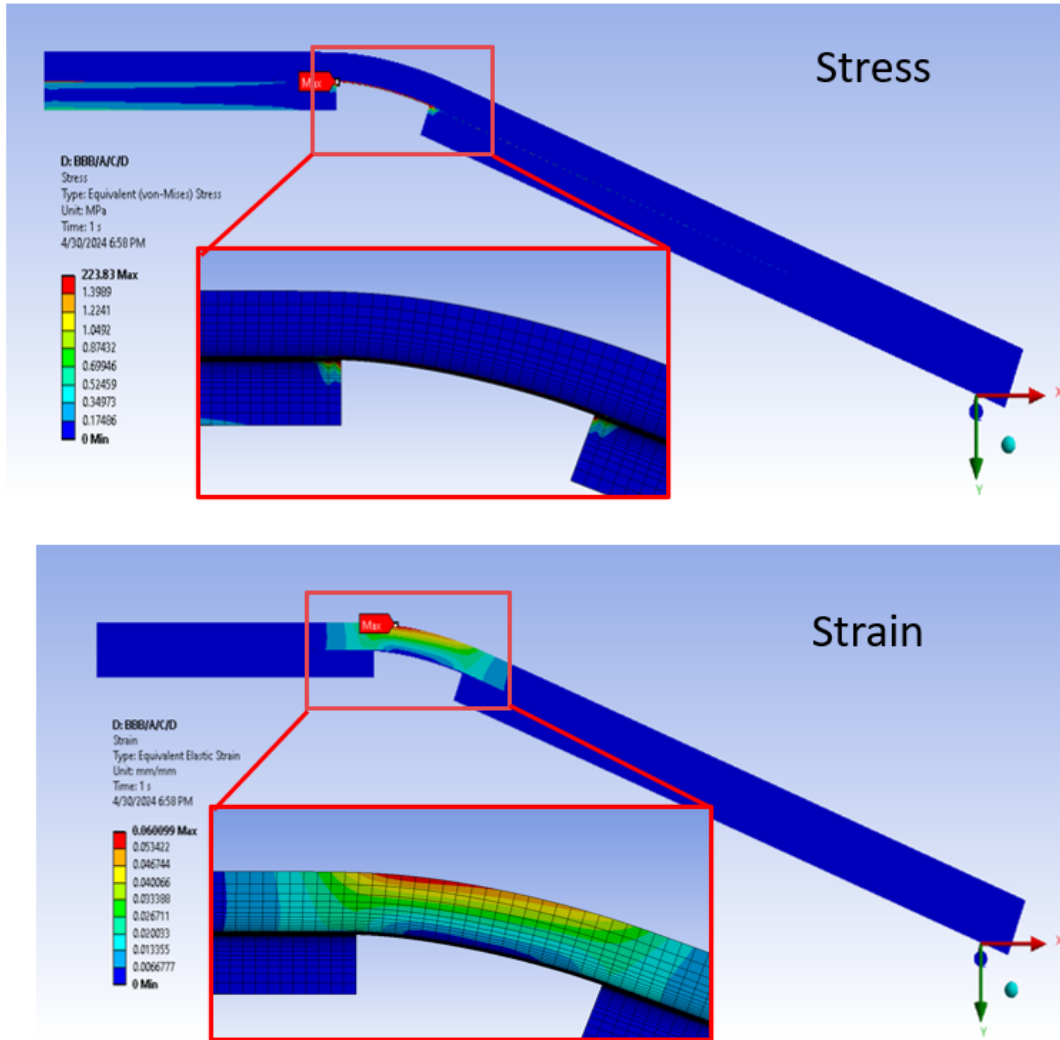


Figure 2-14 Strain and stress plot of battlet electrode at 5 mm bending radius (bend at the center of the left battlet, symmetric).

2.3.2 Impact of battlet size and spacing on electrode flexibility

The impact of battlet size and spacing on battlet flexibility was studied using ANSYS modeling. The pitch of the battlets is kept at 3 mm, while the spacings are 0.5 mm, 0.25 mm, 0.125 mm, and 0.025 mm, respectively. Consequently, the battlet sizes are 2.5 mm, 2.75 mm, 2.857 mm, and 2.975 mm, respectively. Other parameters are the same as mentioned in the previous section. All the models are bent to conform to a 5 mm radius rod.

Figure 2-17 shows the stress distribution of the battlets, and Figure 2-18 plots the stress on the surface of the spacing. The results indicate that as the spacing decreases from 500 μm to 100 μm , the stress increases from 46 MPa to around 500 MPa. Figure 2-19 shows the strain distribution of the battlet electrodes. The results demonstrate that the smaller the battlet spacing, the higher the strain on the current collector.

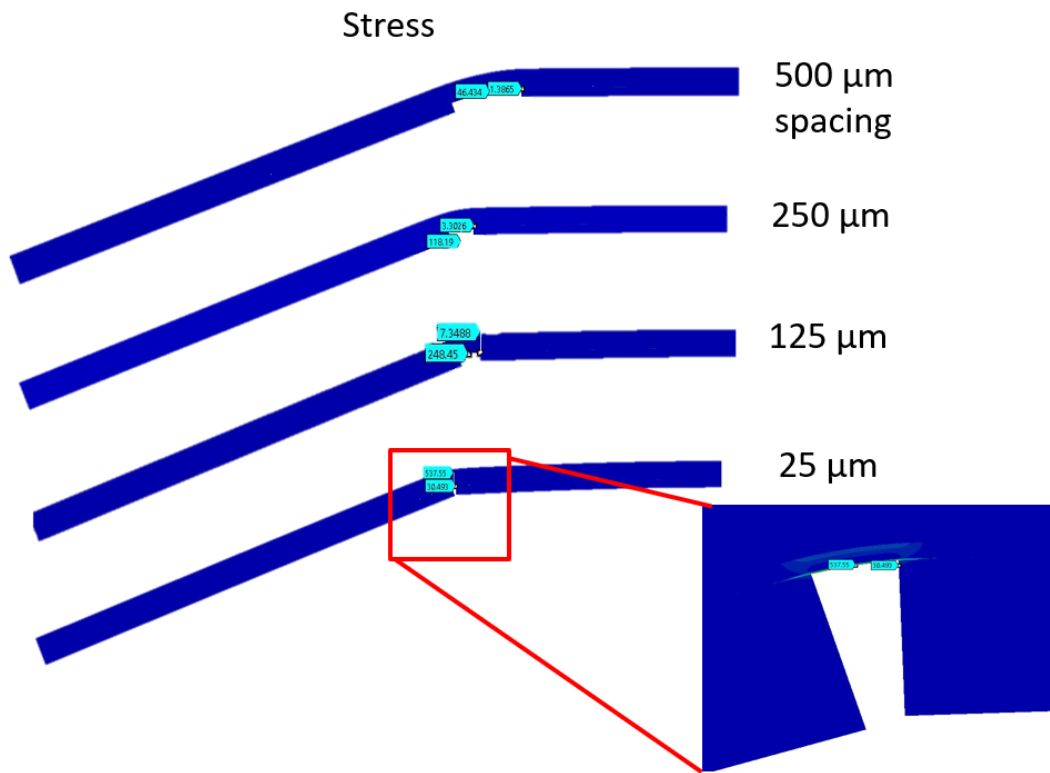


Figure 2-15 Stress plot of different battlet electrode geometries at 5 mm bending radius

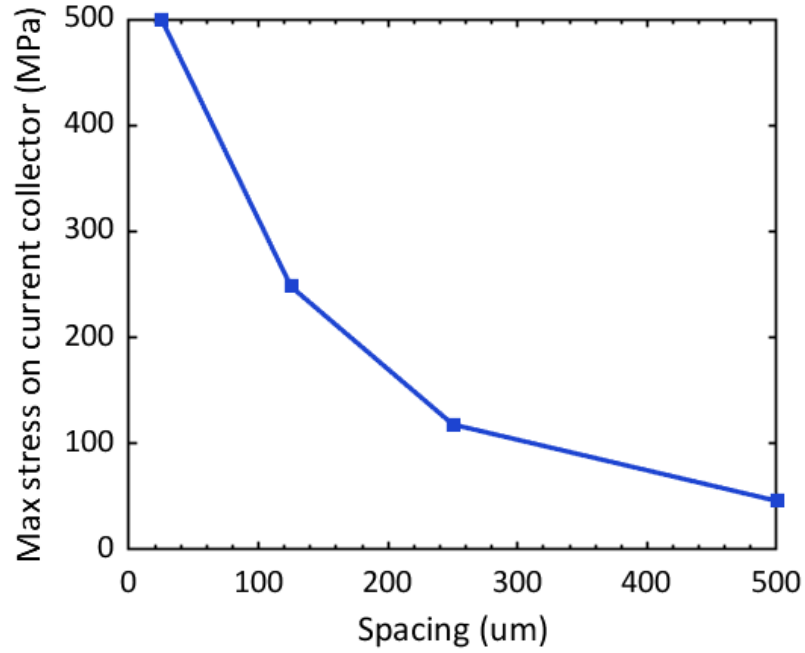


Figure 2-16 The maximum stress of the flexible current collector in different battlet spacing during bending

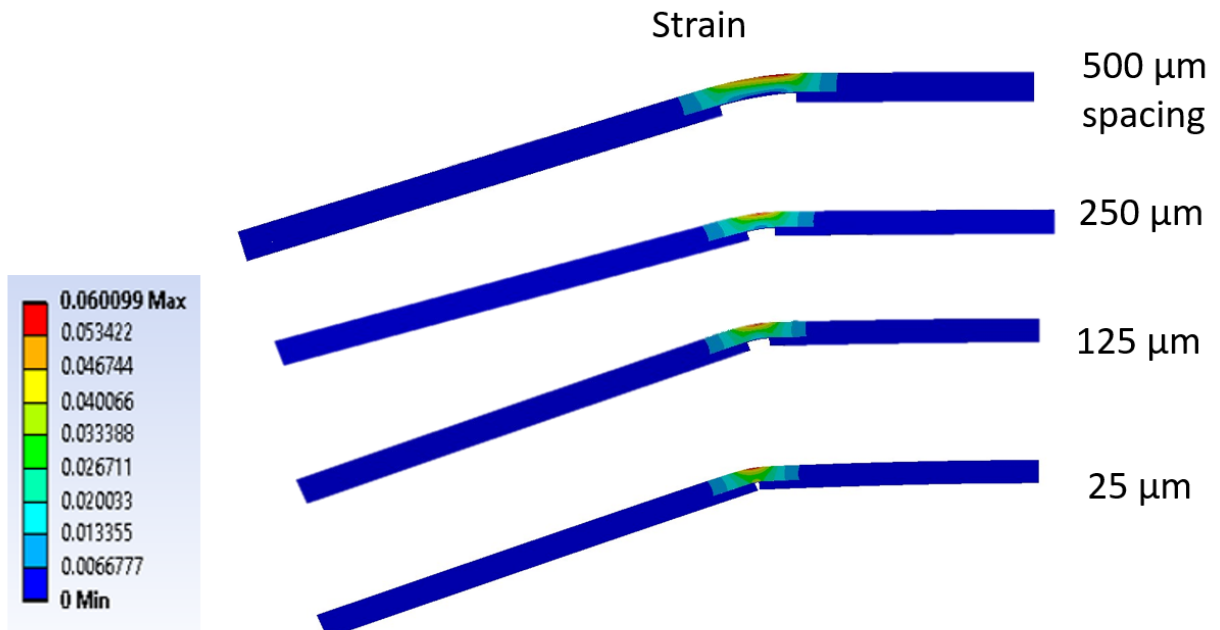


Figure 2-17 Stress plot of different battlet electrode geometries at 5 mm bending radius

In addition, we analyzed the maximum bending of the battlet electrode with a 2.5x2.5 mm electrode size and 0.5 mm spacing, as shown in Figure 2-20. The model indicates that the

maximum inward folding radius is limited by the thickness of the electrode layer, which is 50 μm . The maximum outward folding radius is limited by the thickness of the flexible current collector layer, which is 100 μm . Therefore, the current design of the battlet (2.5x2.5 mm electrode size, 0.5 mm spacing) is sufficient for a 5 mm bending radius, providing adequate flexibility.

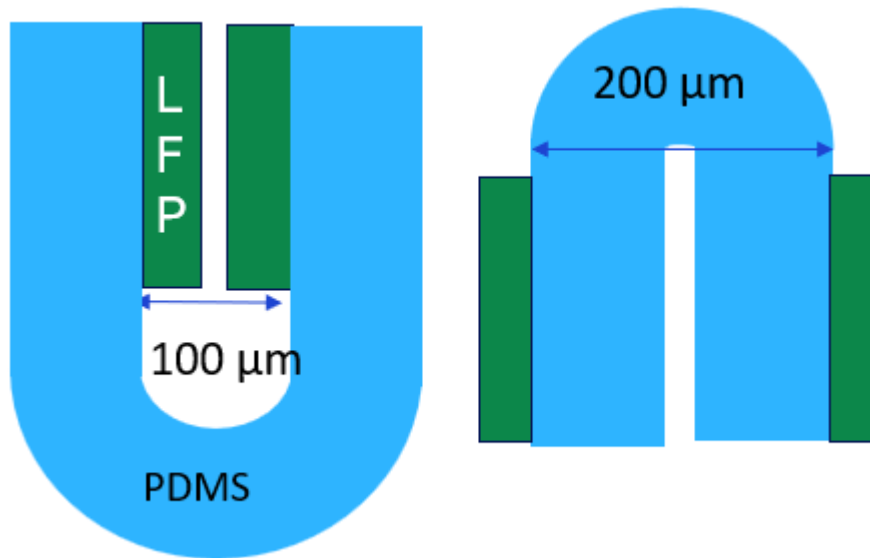


Figure 2-18 Inward and outward folding of a battlet

2.4 Fabrication of battlet battery

2.4.1 Fabrication process

Figure 2-19 shows the fabrication process of the full battlet battery. Initially, a double-sided thermal release tape is laminated onto a 4-inch glass wafer followed by spin coating the PDMS at 2000 rpm on the substrate and curing it at room temperature. The PDMS coating is about 100 μm thick. After PDMS is cured, a 5 μm Parylene C layer is deposited on the PDMS via chemical vapor deposition as a buffer layer to mitigate the CTE mismatch of PDMS and current collectors. Subsequently, 600 nm of Al is sputtered on the Parylene layer as the cathode current collector. The sheet resistivity of Al film is 4 $\mu\Omega\text{-cm}$. Simultaneously, a 30/600 nm Ti/Cu film is sputtered on

another substrate as the anode current collector. The stencil printing process is then used to deposit the battery materials onto the flexible current collectors. After removing the stencil, the electrode slurry is vacuum dried at 100 °C, and a double-sided polyimide ring is applied at the cathode and anode edges as a seal and electrolyte reservoir. The glass fiber separator is then placed on the electrode, and the ionic liquid electrolyte (LiFSI: PYR14FSI = 2:3 with 5wt% VC) is added. ILs are novel liquid materials composed only of anions and cations with unique properties such as very low saturated vapor pressure [49], good ionic conductivity [48], good thermal stability [50], non-flammability, and wide electrochemical window. These properties not only create new opportunities for the design of new Li-ion battery materials with higher energy/power density, better long-cycle stability, and safety, but also offer new possibilities for innovation with new type of battery forms, especially for wearable devices. Finally, the battery cathode and anode are sealed with double-sided polyimide tape, completing the flexible battery after releasing the PDMS from the wafer handler.

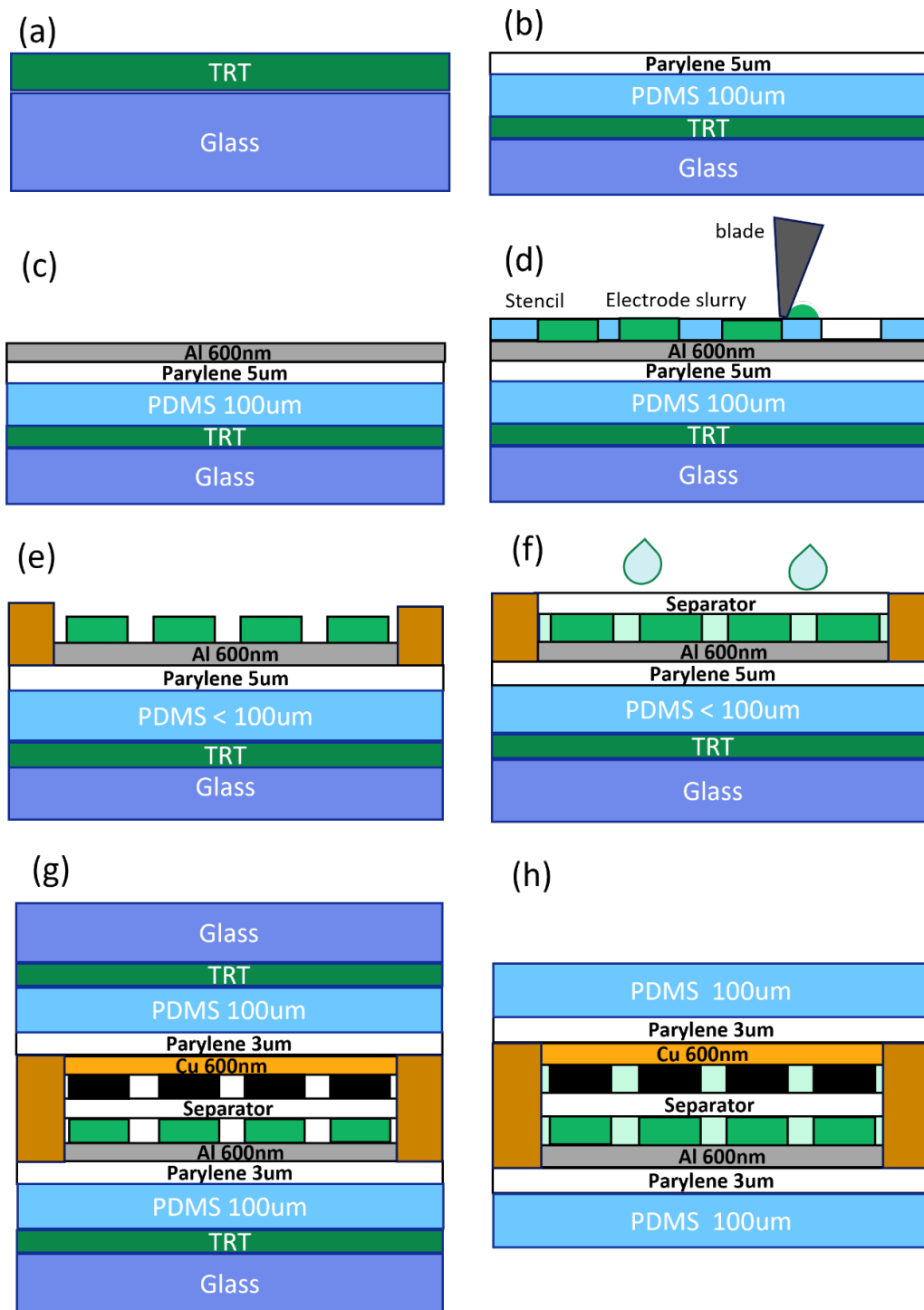


Figure 2-19 Fabrication process of the battlet battery: (a) Lamination of thermal release tape. (b) Deposition of 5 μm Parylene C. (c) Sputtering 600 nm Al/Cu and etch pattern. (d) Screen printing slurry, wet coating thickness (100-200 μm). (e) Dry slurry and laminate double side PI tape as reservoir. (f) Place separator and dispense electrolyte 100 μL . (g) Assembly the full cell (cathode and anode). (h) Release of the substrate.

2.4.2 Surface uniformity

Figure 2-20 (a) and (b) (© 2024 IEEE) shows the cathode and anode optical images, respectively. Each cathode cell is 2.4 x 2.4 mm with 0.5 mm spacing, and each anode cell is 2.5 x 2.5 mm with 0.4 mm spacing. Anode cells are 0.1 mm wider than cathode cells to reduce the Li over plating on the edge of the anode. Figure 2-20 (c) presents the cathode cells' surface profile and height map, with an average thickness of 30-40 μm and a capacity loading of about 1 mAh/cm², equivalent to 6.67 mg/cm² of LFP. The cross-section indicates that the cell edges are about 5-10 μm higher than the center due to the stencil printing process. The anode's average thickness is about 20 μm , with a weight loading of about 1.5 mAh/cm², equal to 4.2 mg/cm².

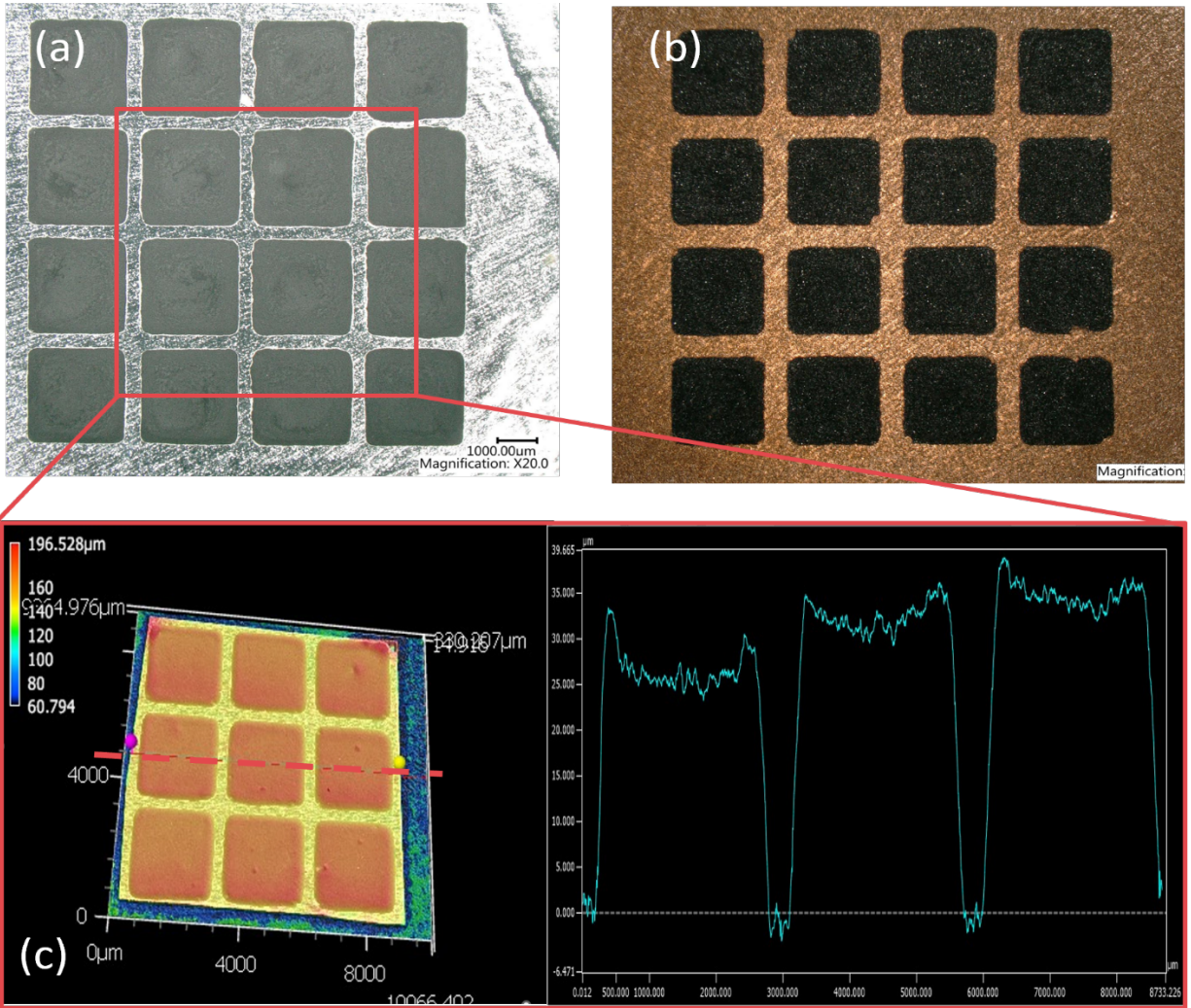


Figure 2-20 optical images of 4x4 (a) battlet cathodes and (b) battlet anodes before bending. (c) Confocal microscope images of the surface profile of the cathode electrodes

2.4.3 Electrode bendability

Figure 2-21 (© 2024 IEEE) demonstrates the cathode and anode optical images before (d) & (f) and after (e) and (g) 1000 bending cycles at 5 mm. The images reveal bending traces between cells, expected due to the lower Young's Modulus of the substrates (PDMS + Parylene C + metal current collectors), indicating bending occurs between the battlet electrodes, thus reducing electrode stress. Figure 2-22 (© 2024 IEEE) presents the SEM images of the LFP battlet at various positions following bending. The center, edge, and corner of the battlet are depicted in (a), (b), and

(c), respectively. These SEM images display the surface of the LFP battlet layer without any evident cracks. Additionally, some bending-induced wrinkles are visible on the surface of the current collector after cycling as shown in (d), yet no fractures or cracks are apparent on the surface. Compare with conventional planar electrode after bending shown in Figure 2-5, it shows the battlet electrode improves the bendability of the cell.

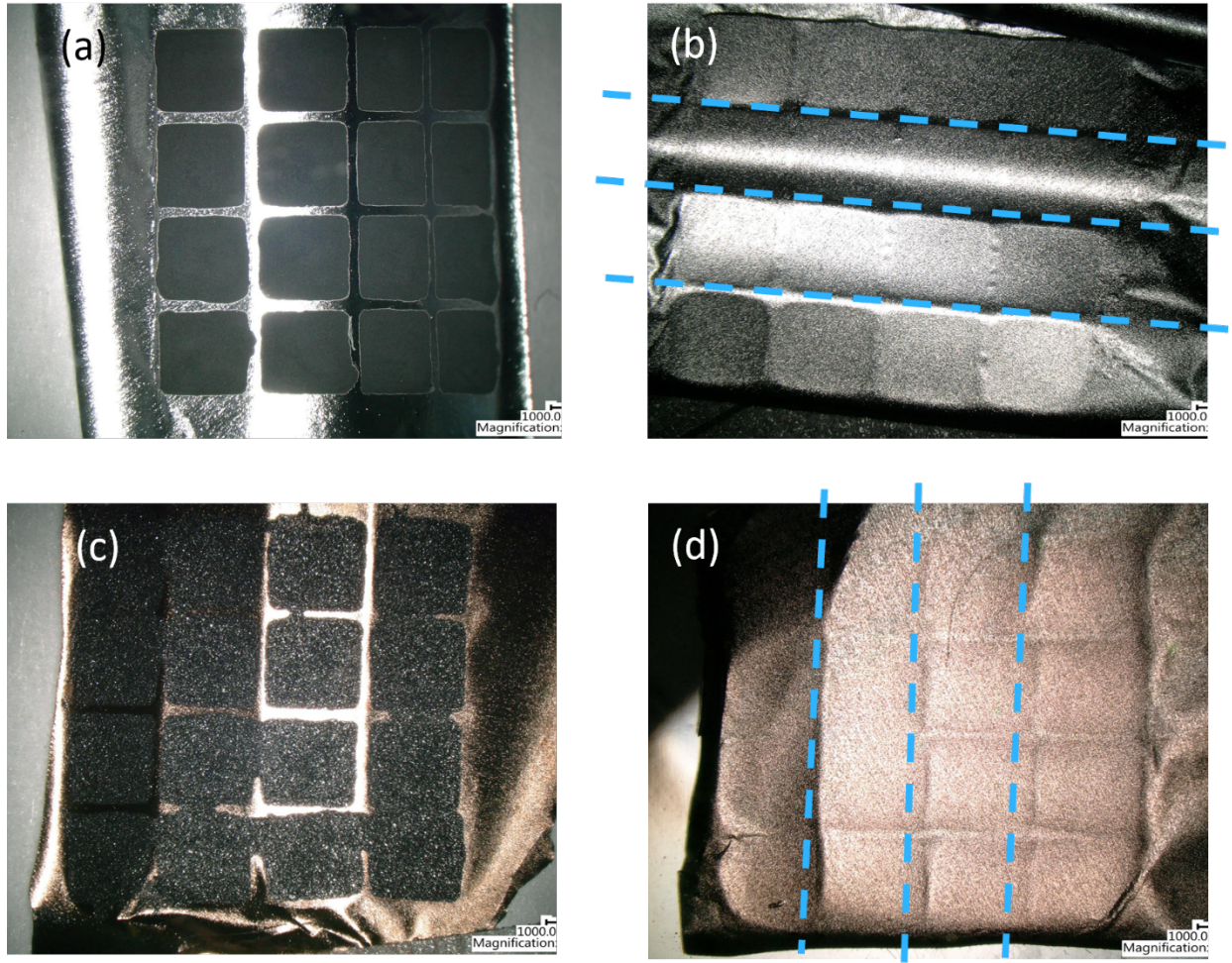


Figure 2-21 optical images of (d) cathodes and (f) anodes after bending test; (e)(f) backside of the cathode and anode showing the bending traces in between each battlet.

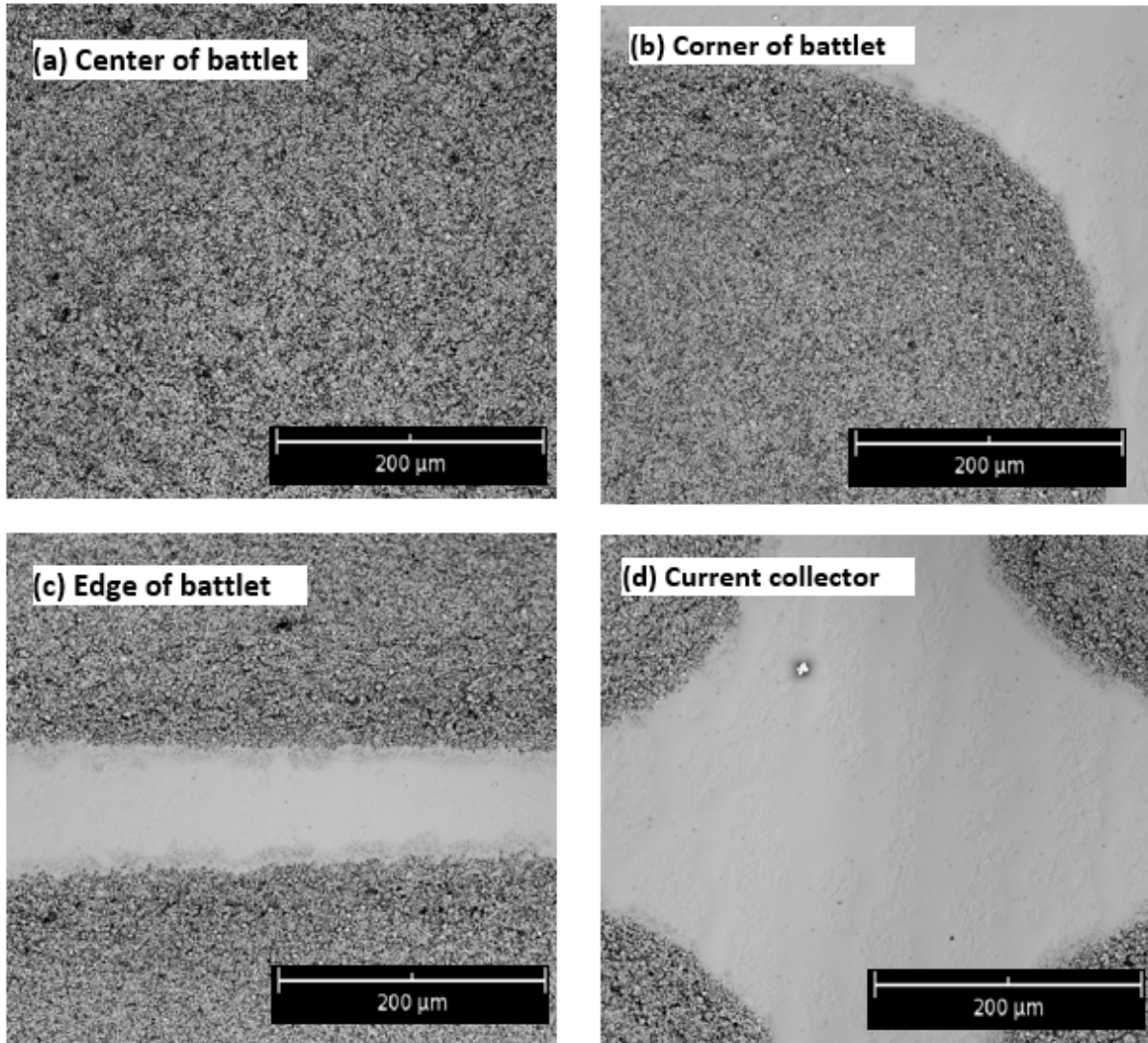


Figure 2-22 SEM images of battlet electrode at different positions after 1000 bending cycles

2.4.4 Porosity

Figure 2-23 illustrates the surface of cathode and anode battery electrodes. For the cathode, the distribution of the LFP size, with a D90 of less than 1 μm , results in a smoother surface characterized by higher porosity. From the surface, it shows a uniform and smooth distribution. At the corner, there is a distinct separation between the spaces, indicating that the cells are well segmented and not interconnected. For the anode, as shown in Figure 2-23 (c) and (d), the corners

are also clearly defined, and the cells are well segmented. In Figure 2-23 (d), the size of the graphite powder, ranging from 20-30 μm , is significantly larger than that of the LFP. The graphite grains are intact without any cracks. Additionally, the surface of the electrode exhibits a network-like mesh structure, which is attributed to the PVDF binder material.

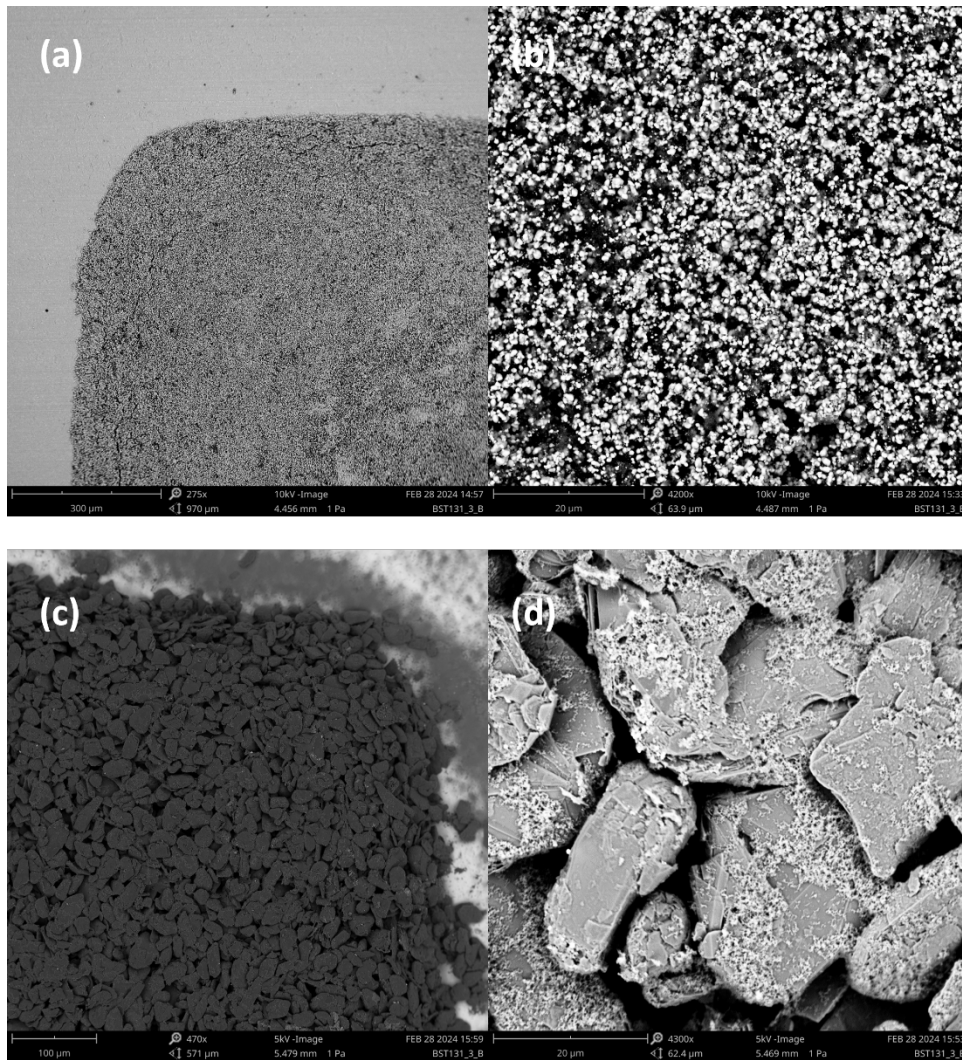


Figure 2-23 SEM images of the surface of the (a) cathode battlet electrode at the corner and (b) zoom-in image. (c) anode battlet electrode at the corner and (d) zoom-in image.

Porosity measurements were also conducted to evaluate the cross-section and porosity of battlet electrodes. Figure 2-24 illustrates the cross-section of the cathode at (a) spacing and (b) on the electrode. From (a), it is observed that there is a slope that appears flattened due to the

properties of the LFP cathode, while the street remains clean, and the electrodes are segmented. Figure 2-24 (c) presents the cross-section of the electrode, and the images were processed using ImageJ to calculate the porosity, as shown in Figure 2-24. Table 2-1 lists the parameters of the calculation by Image J. The average LFP size is 1.112 μm , which aligns closely with the specifications. The porosity of the LFP cathode is 51.868%, comparable to that achieved by the conventional doctor blade method.

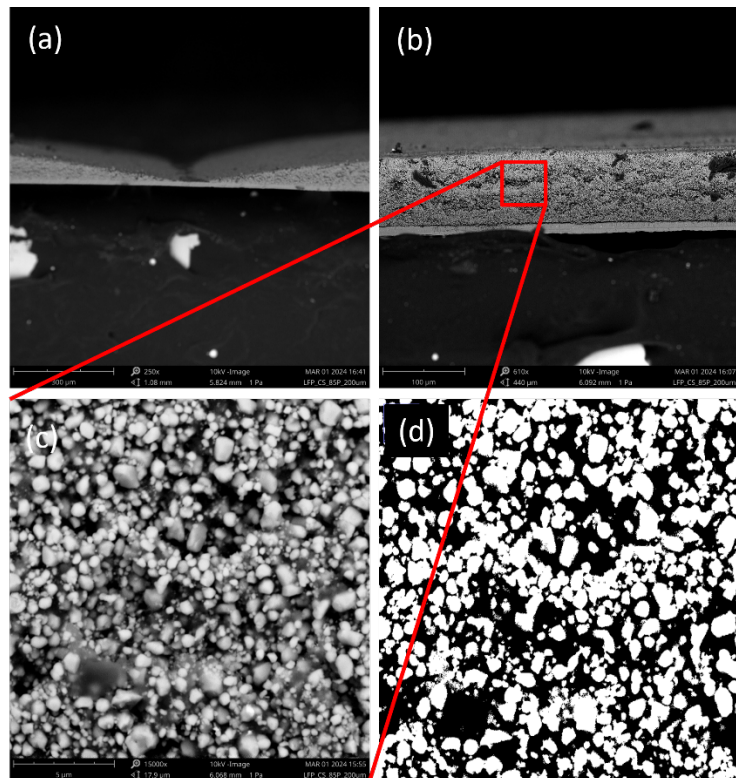


Figure 2-24 cross-section of LFP cathode (a) in between of electrode (b) and (c) center of the electrode. (d) processed image for porosity measurement

Table 2-1 Statistical results of LFP cathode cross-section by Image J

Selected size	count	Total area	Average size	%area	%porosity
> 0.1 μm^2	132	146.74 μm^2	1.112 μm	48.132	51.868

Figure 2-25 also displays the cross-section of the anode electrode at (a) spacing and (b) on the electrode. From (a), it is noted that there is a sharper slope compared to that of the LFP, due to the larger size of the graphite grains. Figure 2-25 (c) shows the cross-section of the electrode, with images processed using ImageJ to calculate the porosity, as depicted in Figure 2-25 (d). Table 2-2 provides the parameters for the calculation. The average graphite size is 73.915 μm , and the porosity of the graphite anode is 35.68%. These results indicate that the screen-printing method produces a similar electrode structure in terms of porosity.

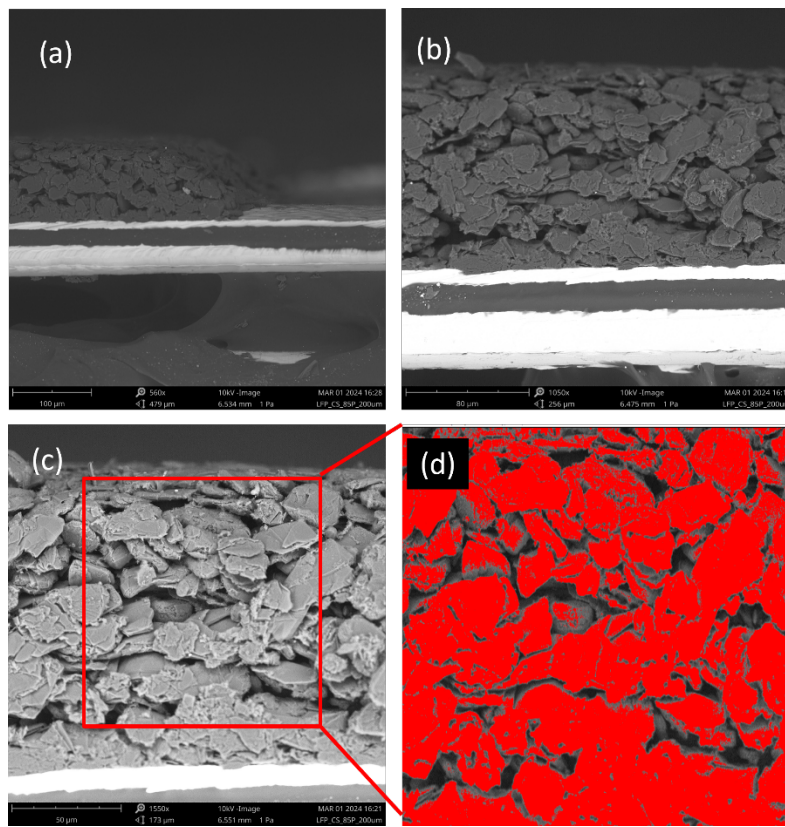


Figure 2-25 cross-section of LFP cathode (a) in between of electrode (b) & (c) center of the electrode. (d) processed image for porosity measurement.

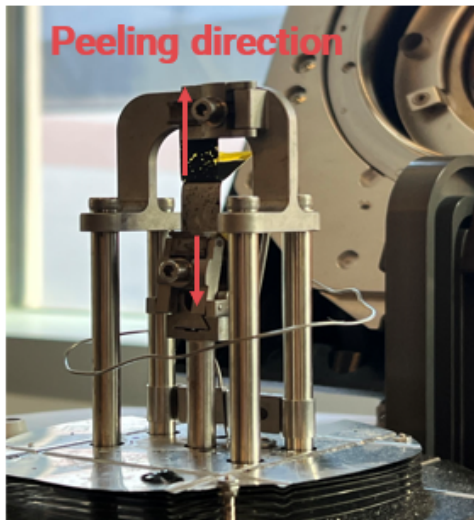
Table 2-2 Statistical results of graphite anode cross-section by Image J

Selected size	count	Total area	Average size	%area	%porosity
---------------	-------	------------	--------------	-------	-----------

> 9 μm^2	28	14770.1 μm^2	73.915 μm	64.14	35.86
---------------------	----	-------------------------	----------------------	-------	-------

2.4.5 Adhesion test

The surface roughness of as-rolled aluminum foil is typically high, as indicated in Figure 2-26. Consequently, the adhesion between the electrode and substrate during fabrication is generally not a major concern. However, the low surface roughness (7.1 nm) of the sputtered current collector poses challenges, leading to weak adhesion at the current collector/electrode interface.



T-peeling test setup

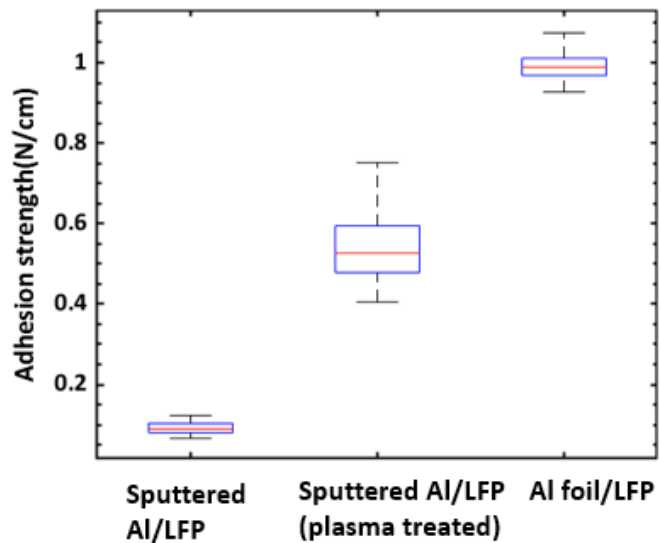


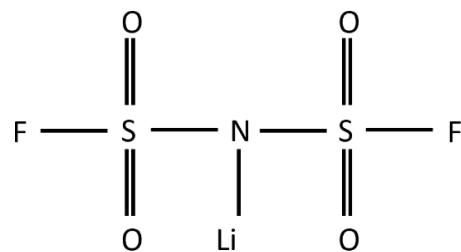
Figure 2-26 (left) T-peeling test step (right) comparison of the electrode layer - current collector layer adhesion strength

To address this issue, we implemented a plasma cleaning method to enhance substrate adhesion. This involved employing Ar plasma to cleanse the surfaces of both aluminum and copper metals before slurry coating, leveraging the principles of plasma coating. Results from peeling

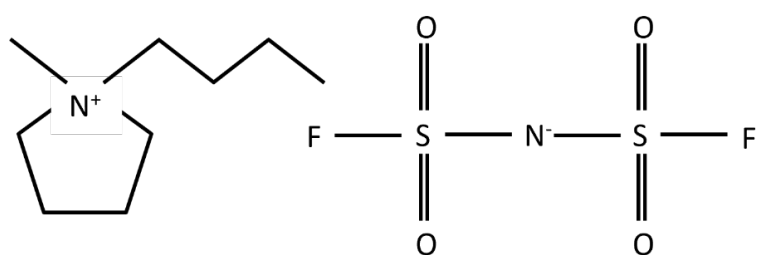
tests revealed a significant improvement in adhesion strength, soaring from 0.1 N/cm to 0.5 N/cm, a 500% increase in strength.

2.4.6 Comparison of ionic liquid and organic electrolytes

Ionic liquids (ILs) are new liquid materials composed only of anions and cations with unique properties such as very low saturated vapor pressure [48], high ionic conductivity (close to conventional liquid electrolyte) [50], good thermal stability [51], non-flammability, and wide electrochemical window, which not only create new opportunities for the design of new Li-ion battery materials with higher energy/power density, better long-cycle stability, and safety, but also offer new possibilities for innovation of new type of battery forms, especially for wearable devices. In this work, 1M LiFSI + PYR14FSI with 5% VC is utilized as the ionic liquid (IL) electrolyte. The structure of this electrolyte system is depicted in Figure 2-27 (© 2021 IEEE). The contact angle between the ILs and the LFP film was measured and compared with water, as illustrated in 2-28 (© 2021 IEEE). The contact angle of the IL on the LFP film is 15°, indicating good wettability which enhances the ionic mobility of the IL. It is noteworthy that the wettability of organic electrolytes is typically close to 0.



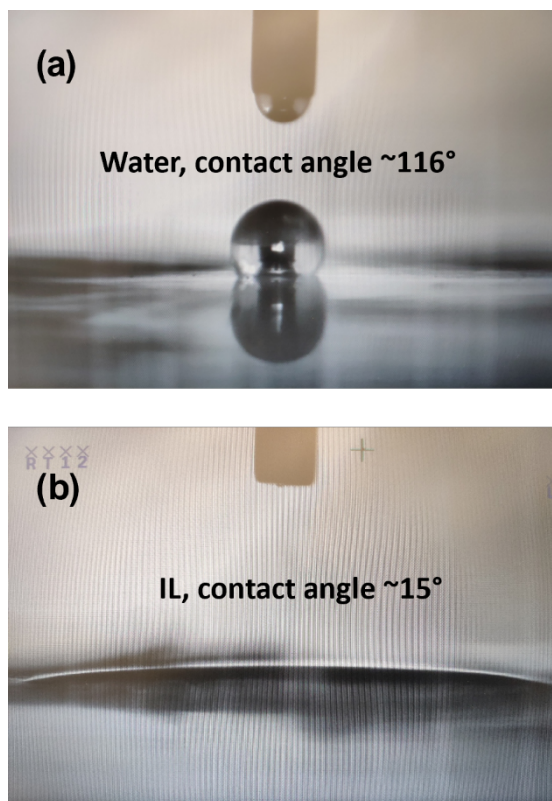
LiFSI



PYR₁₄⁺

FSI⁻

Figure 2-27 Chemical structure of LiFSI as battery ionic liquid electrolyte an PYR14FSI as solvent for the ionic liquid



2-28 Contact angle measurement indicating the wettability of the ionic liquid on the surface of the LFP electrode.

To evaluate the electrochemical performance of the LFP battery in the ionic liquid electrolyte, 2032 coin cell batteries were assembled and tested under various charging and discharging rates as shown in the Table 2-3. The cathode, anode, and electrolyte were LFP (0.5 cm^2), Li-metal (0.38 cm^2), and 1M LiFSI PYR14FSI ($100 \mu\text{L}$). LFP slurries were coated ($300 \mu\text{m}$ thick wet film) on Al foil and the loading density of LFP is 6.3 mg/cm^2 , which provides an areal capacity of 1 mAh/cm^2 based on a theoretical capacity of 170 mAh/g for LFP. Therefore, the total theoretical capacity of the testing battery sample is 0.5 mAh . To further compare the electrochemical performance of the ionic liquid with traditional organic electrolytes, coin cells with 1M LiPF₆ in DEC : EC : DMC = 1 : 1 : 1) were also tested.

Table 2-3 Electrode performance test parameters and value.

Parameters	Value
LFP cathode	170 mAh/g
Loading density	6.3 mg/cm ²
Loading capacity	1 mAh/cm ²
Cathode	0.5 cm ² (= 0.5mAh)
C/3 rate	0.16 mA
1C rate	0.5 mA
2C rate	1 mA

Figure 2-29 (a) and (b) (© 2024 IEEE) show the charge and discharge curves at various C rates (C/3, 1C, and 2C) for the ionic liquid and organic electrolyte batteries, respectively. Given a capacity of 1 mAh/cm², the corresponding currents densities at these three different C-rates are 0.33 mA/cm², 1 mA/cm², and 2 mA/cm², respectively. Each current rate is cycled 12 times. The results show that the ionic liquid battery provides 0.8 mAh/cm² at C/3, 0.7 mAh/cm² at 1C, and 0.65 mAh/cm² at 2C rate, which is 80%, 70%, and 65% of the theoretical loading capacity, respectively. For the battery with 1M LiPF₆ DEC:EC:DMC electrolyte, capacities of 0.95 mAh/cm² at C/3, 0.87 mAh/cm² at 1C, and 0.8 mAh/cm² at 2C were obtained, which is 95%, 87%, and 80% of the theoretical capacity. Greater polarization is observed in the ionic liquid electrolyte battery as indicated by the increased overpotential and sloping feature of the redox plateau at higher C rates.

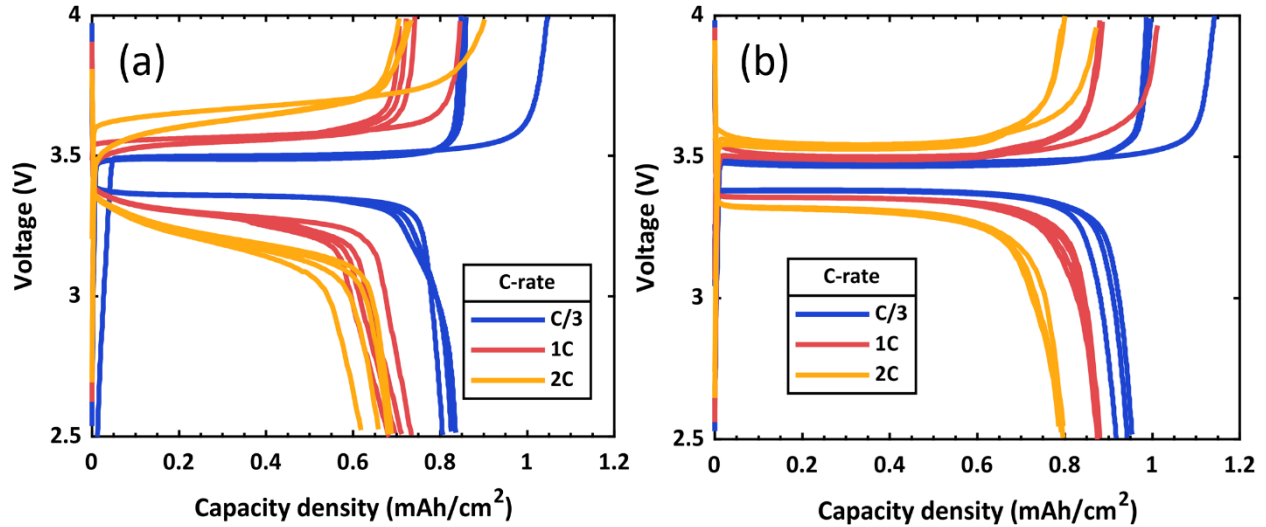


Figure 2-29 Testing results of LFP/ionic liquid electrolyte/Li metal battery system: Charging/discharging cycling at different C-rates for (a) ionic liquid electrolyte and (b) organic electrolyte

Figure 2-30 (a) and (b) (© 2024 IEEE) show the discharge capacity as a function of cycling (blue points) and the corresponding coulombic efficiency (red points) at 2C for the ionic liquid battery and organic electrolyte battery, respectively. The average coulombic efficiency across 20 cycles for the ionic liquid electrolyte and organic electrolyte is 89.15% and 98.26% respectively, while the capacity decay of each type of battery is 75.04% and 93.74%. The ionic liquid battery exhibits a larger capacity decay and lower Coulombic efficiency relative to the conventional organic liquid electrolyte.

Considering the above testing results, including capacity, capacity decay rate, and Coulombic efficiency on both ionic liquid electrolyte and organic electrolyte, we find that the electrochemical performance is lower than the organic electrolyte. The main reason for this is due to ionic liquid electrolyte having lower ionic mobility (ionic conductivity) than conventional organic electrolyte due to higher viscosity of the solvent at room temperature [52]. On the other hand, although the capacity decays faster for ionic liquid, it also became more stable after 10 cycles

than that of the organic electrolyte. Therefore, considering optimization possibility and safety, using the ionic liquid electrolyte for wearable batteries is a more useful for the application.

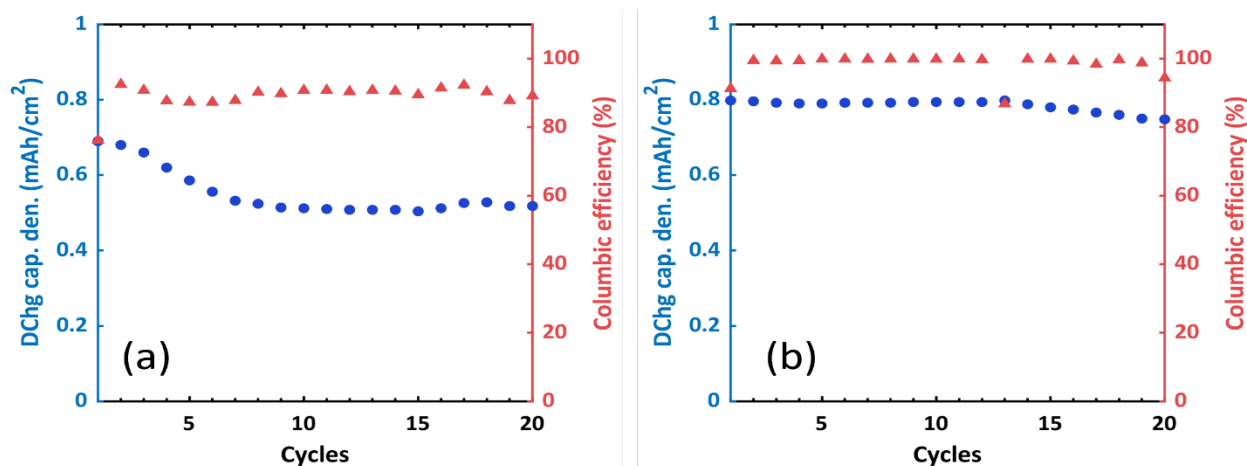


Figure 2-30 Discharge capacity density and columbic efficiency for 20 cycles at 2C rate for (c) ionic liquid electrolyte and (d) 1M LiPF6 in DEC:EC:DMC (1:1:1) organic electrolyte.

2.4.7 Thickness optimization for reducing the surface crack

In the pursuit of enhancing our Li-ion battery's capacity, which is limited by the LFP cathode (150 mAh/g) as opposed to the graphite anode (370 mAh/g), we have identified two potential methods for enhancing the capacity of the cathodes considering the cathode structure as shown in Figure 2-31:

Increasing electrode coating thickness: An increased coating thickness of the electrode could lead to higher capacity. However, this method carries a potential downside as the higher diffusion length of ions and electrons could lead to increased ionic and electronic impedance.

Increasing LFP (active ingredients) percentage in slurry: Elevating the percentage of Lithium Iron Phosphate (LFP) in slurry could also contribute to improved cathode capacity. However, this approach comes with two drawbacks: the reduction of Carbon black, which could

lead to higher film resistance, and the reduction of PVDF, which could result in lower electrode-to-current collector adhesion strength.

Given these options and the accompanying trade-offs, we are now exploring the delicate balance between improving battery capacity and maintaining an acceptable peak discharge current.

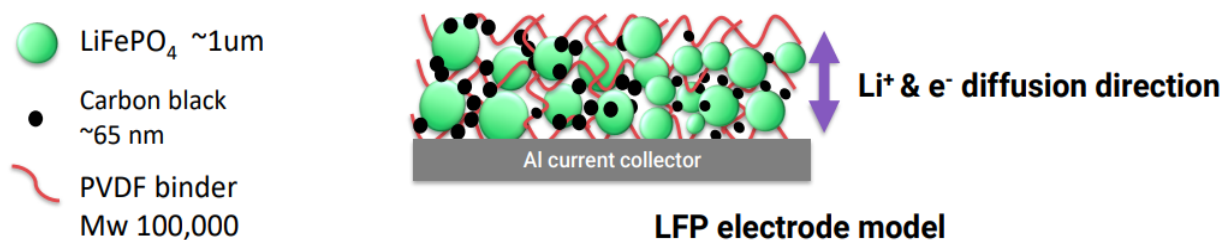


Figure 2-31 structure model of LFP electrodes (not to scale)

Building on the outcomes of our previous investigations and experimental framework, we examined eight different composition ratios and coating thicknesses for the LFP cathodes, as illustrated in Table 2-4. The ratios of LFP : Carbon : PVDF ranged from 8 : 1 : 1 to 9 : 0.5 : 0.5.

Key parameters show in Figure 2-32 and Figure 2-33 including electrode thickness, loading density, theoretical capacity, and final area capacity were measured for each sample, revealing several crucial insights. Firstly, electrode thickness becomes a significant factor impacting performance when it exceeds 60 μm . Most samples demonstrated a measured capacity of approximately 90% of the theoretical value. However, a decline in capacity was observed for the 955-1/2 samples, which was attributable to their increased thickness and sub-optimal quality. Notably, commercial LFP electrodes typically exhibit capacities between 1-1.5 mAh/cm^2 . The study found that the optimal coating thickness and composition are 8.5:0.8:0.7 at 100 μm , achieving 1.15 mAh/cm^2 . These observations will be instrumental in the ongoing optimization of our flexible battery technology.

Table 2-4 Design of experiment for the optimization of the electrode slurry optimization

Sample ID	LFP : Carbon : PVDF (weight ratio)	Coating thickness (um)	LFP loading density (mg/cm²)
811-1	8 : 1 : 1	100	5.5
811-2	8 : 1 : 1	200	8.11
8587-1	8.5 : 0.8 : 0.7	100	6.46
8587-2	8.5 : 0.8 : 0.7	200	7.99
8515-1	8.5 : 1 : 0.5	100	8.5
8515-2	8.5 : 1 : 0.5	200	9.69
955-1	9 : 0.5 : 0.5	100	10.34
955-2	9 : 0.5 : 0.5	200	13.1

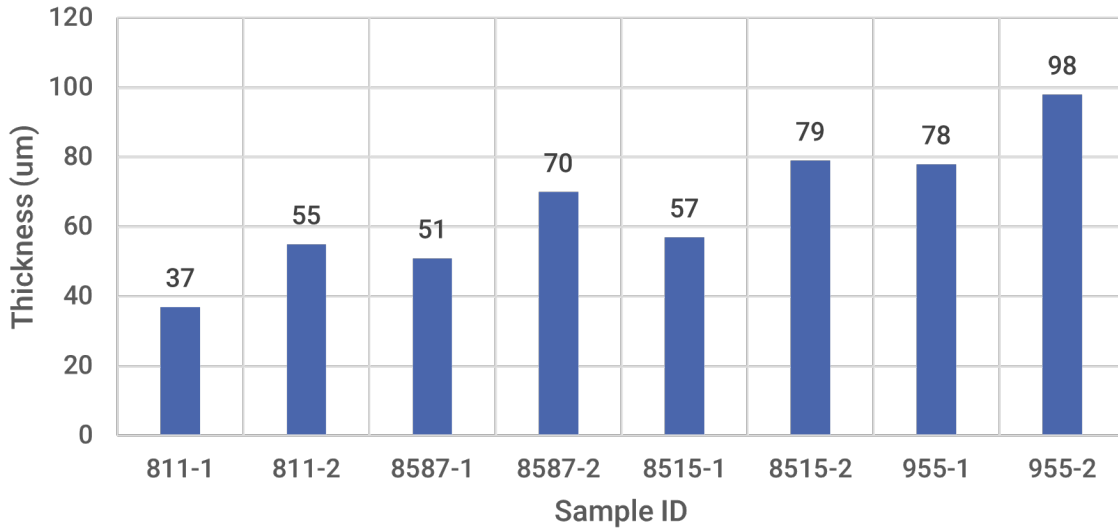


Figure 2-32 Electrode thickness in different slurry compositions and stencil thicknesses

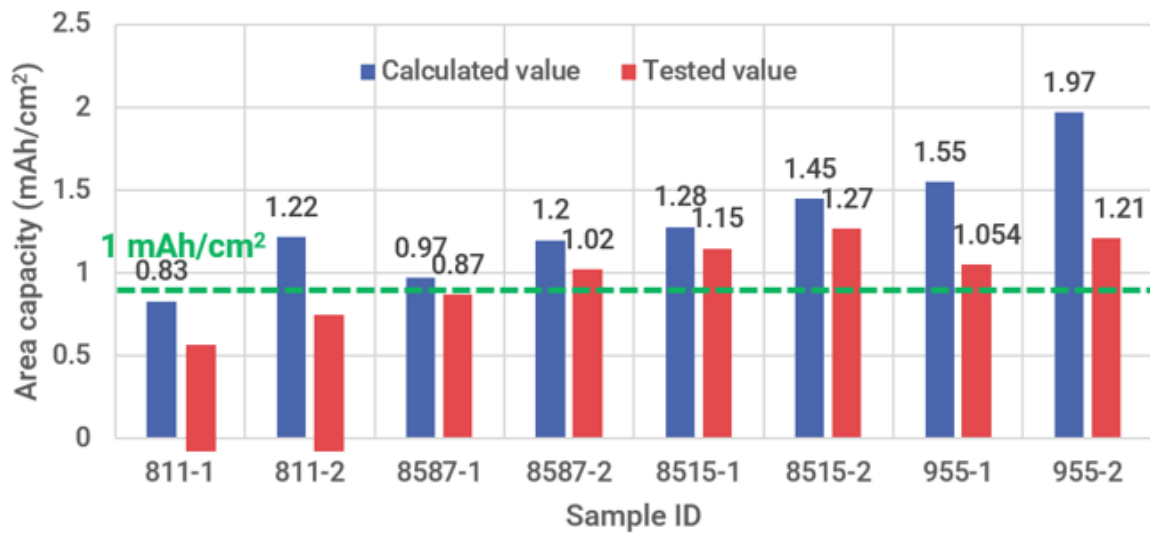


Figure 2-33 Calculated capacity of the electrode and the tested capacity of the electrode in different compositions and stencil coating thickness.

Furthermore, we carried out an analysis of the film coating thickness and composition ratio in Figure 2-34, with the corresponding results presented below. Our findings suggest that at a coating thickness of 100 µm, the film remains intact with no observable cracks. However, increasing the thickness to 200 µm results in the formation of cracks in the dry electrode. These

cracks are attributed to internal stress arising during the drying process due to the increase of ununiform thickness of the battlet layer. Therefore, present screen printing process uses the 100 μm PDMS stencil thickness for printing the battlets.

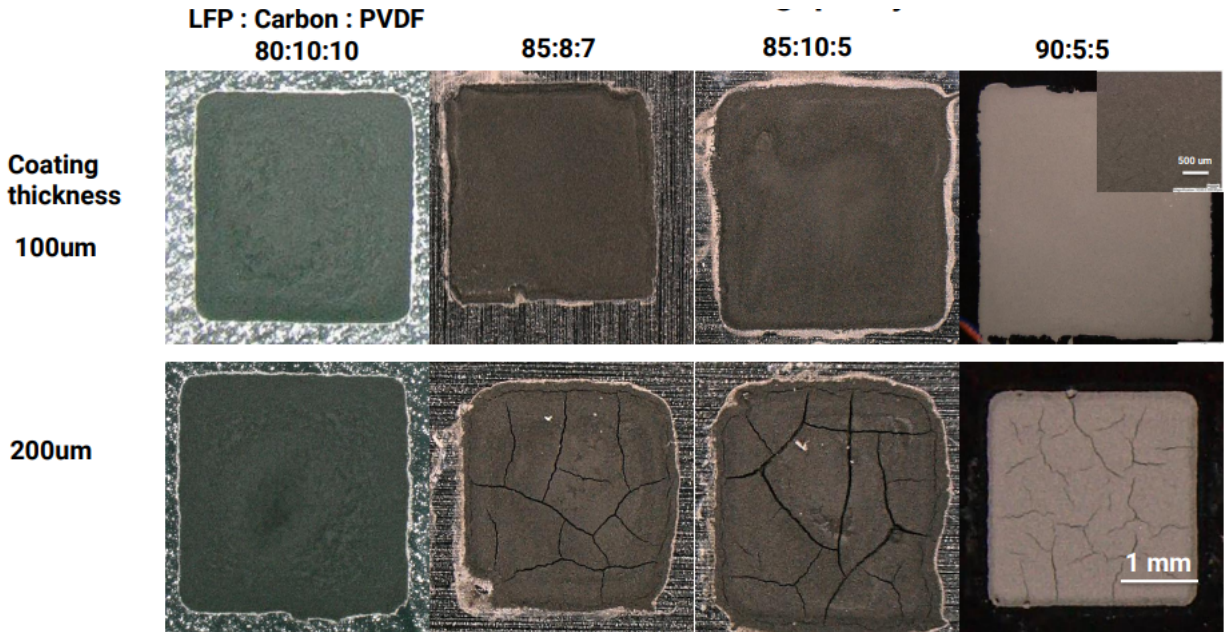


Figure 2-34 Optical images of the electrode under different compositions and stencil coating thickness.

2.4.8 Flexibility and reliability of full cell

Figure 2-35 (© 2024 IEEE) shows the assembled battery in a static bending state on a 5 mm and a 10 mm radius rod. The output voltage is read by multimeter. In both cases, it maintains a stable 3.24 V output, aligning with the designed nominal voltage, indicating the batteries' functionality at 3.24V.

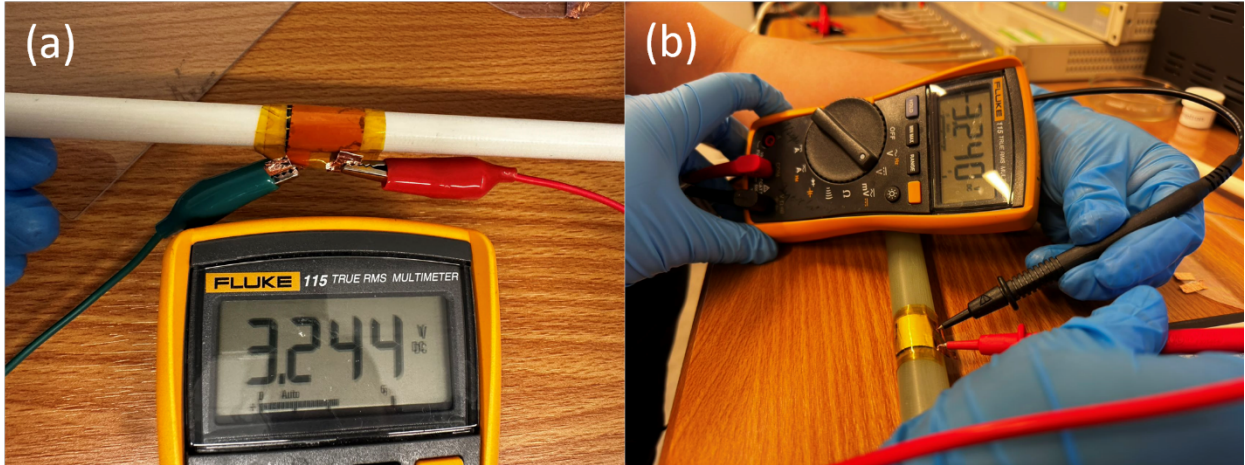


Figure 2-35 Batteries at static state at (a) 5 mm bending radius (b) 10 mm bending radius.

Figure 2-36 shows the assembled battery in a dynamic bending status from flat to folding state by hands. The voltmeter read is 3.245 V initially and remain constant 3.24 during folding test until completely folded (< 1 mm). To further explore the performance of the battery, we tested the performance using the battery tester and compared it with the conventional designed battery.

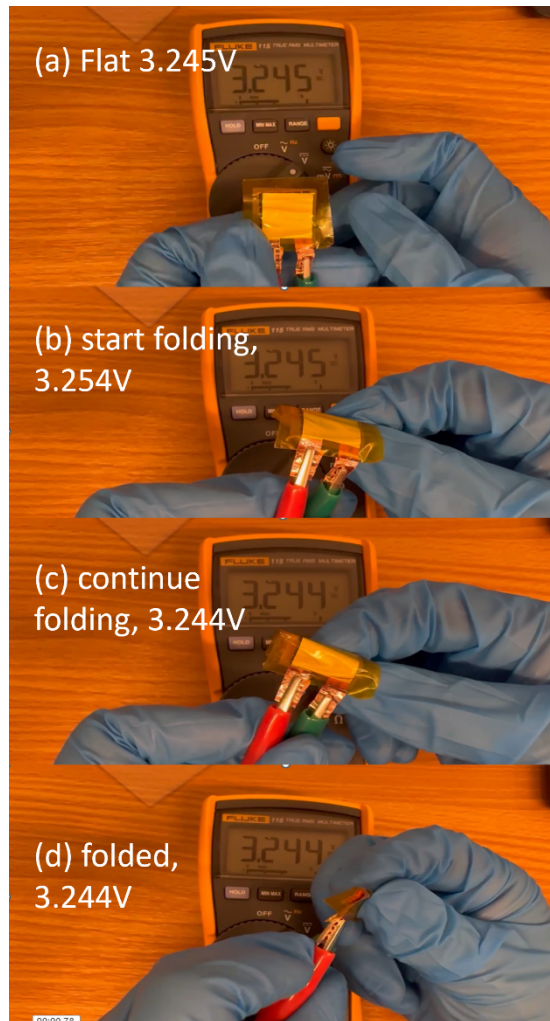


Figure 2-36 Output voltage at dynamic bending test

To evaluate the performance of the battlet electrode design, we prepared both battlet and "planar" (no-battlet design) electrodes and cycled them at different rates from 0.2 C to 2 C, as shown in Figure 2-37 (a) (© 2024 IEEE). The results indicate that for the unbent sample, the battlet design maintains identical performance across different C rate tests with average performances of 99%, 95%, 88%, and 88% at 0.2 C, 0.5 C, 1 C, and 2 C, respectively. However, after the bending test, the planar electrode exhibits significantly more performance decay especially at higher cycling rates. For the bent planar battery at 0.5 C, the capacity retention is 81%, and at higher cycling rates of 1C and 2C, the capacity drops to 47% and 12%, respectively. Conversely, for the

battlet battery, the capacities at 0.2 C and 0.5 C remain nearly unchanged from before bending test. At higher cycling rates of 1C and 2C, the capacity decreases to 79% and 45%, respectively, which is 1.68 and 3.7 times higher than that of the planar battery after bending.

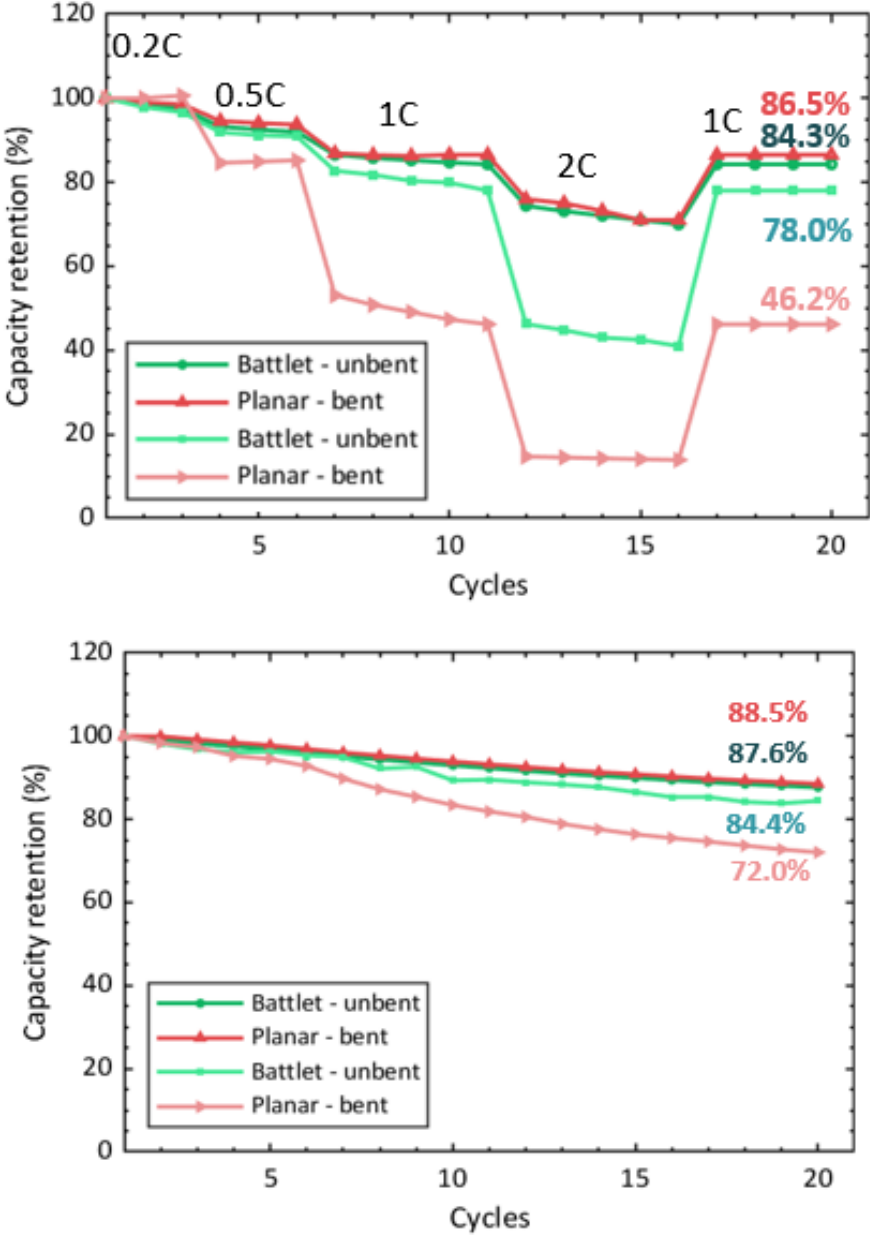


Figure 2-37 (a) comparison of the rate performance of the battlet battery and planar electrode battery in different C rates. (b) comparison of the cycling performance of the battlet battery and planar electrode battery

2.4.9 Reliability test

Figure 2-38 presents the open-circuit voltage change of the battlet batteries during resting. The batteries were pre-charged to 3.5 V under constant voltage charging, then measured for open-circuit voltage. This test considered two different packaging and resting environments: flexible packaging and coin cell packaging, under both argon gas and air environments (20 °C, and 40% humidity). Initially, all batteries exhibited a voltage drop due to the cell polarization during charging. However, during the 50-hour aging test, the voltages of the flexible batteries remained stable in both argon and air environments, matching the voltage performance of the coin cell. This outcome suggests that flexible packaging provides effective sealing against oxygen and moisture, comparable to that of the coin cell.

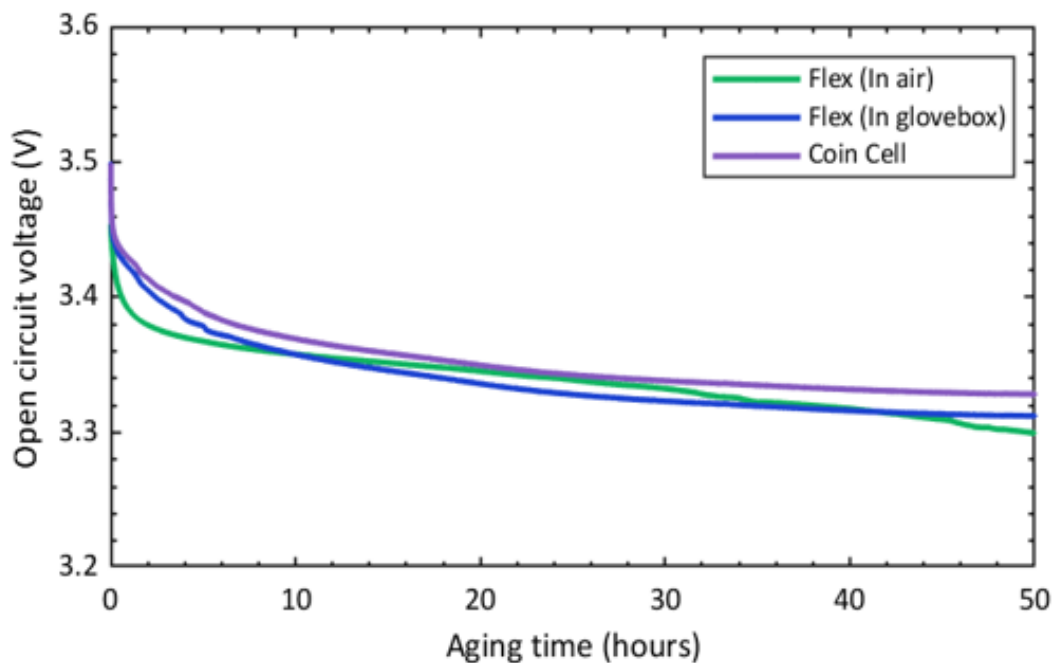


Figure 2-38 Comparison of the open circuit voltage variation in 50 hours aging time of the assembled full cell with flexible package and coin cell package in Ar gas environment and in lab environment.

Figure 2-39 presents the humidity test results for the battlet battery. Three samples are charged to 3.5 V and exposed to different humidity environments (50%, 60%, 70%, and 80%),

with each condition lasting for 10 hours. The open-circuit voltage is measured hourly using a voltmeter. The results indicate that two samples failed at 80% humidity, and one sample failed at 70% humidity. This failure is suspected to be due to moisture diffusion through the packaging, which then reacted with electrolyte.

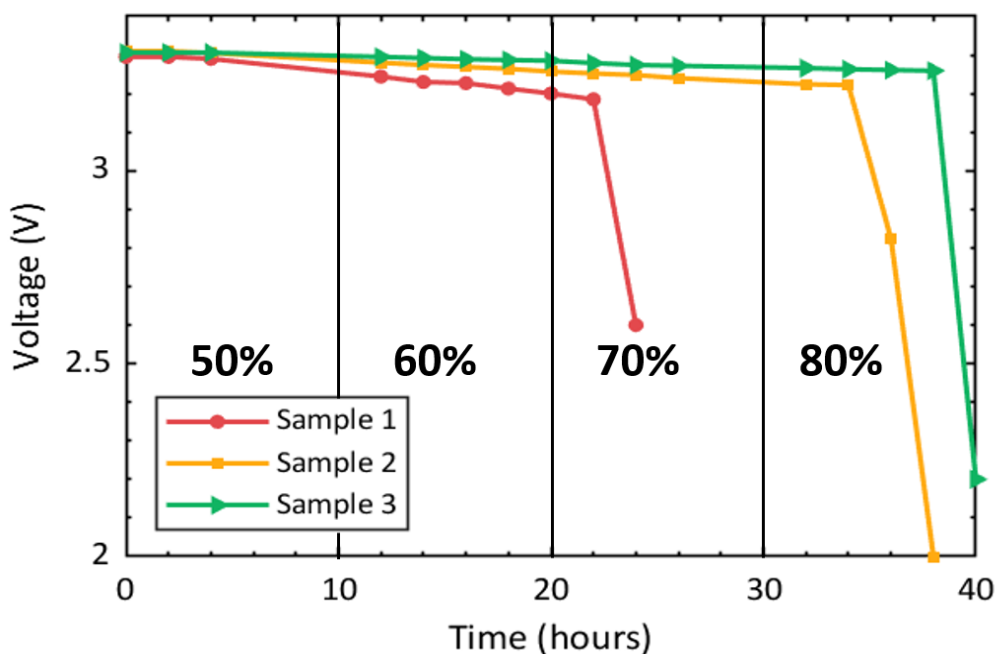


Figure 2-39 Open-circuit voltage of battlet battery under different humidity environment.

Figure 2-40 shows the thermal stability test results of a battlet battery. A sample is charged to 3.5 V and its open-circuit voltage is measured in real-time over 100 hours. Concurrently, the battery is placed on a hot plate with temperatures set sequentially at 25 °C, 45 °C, 55 °C, 65 °C, and 75 °C, each maintained for 10 hours. The results indicate that at temperatures above 65 °C, the increase in open-circuit voltage drop suggests accelerated internal leakage, likely due to the decomposition of vinylene carbonate.

These reliability test results show that the fully assembled flexible battery has similar internal leakage compared with coin cell package. And the battery is stable up to 55 °C and 60-70% humidity.

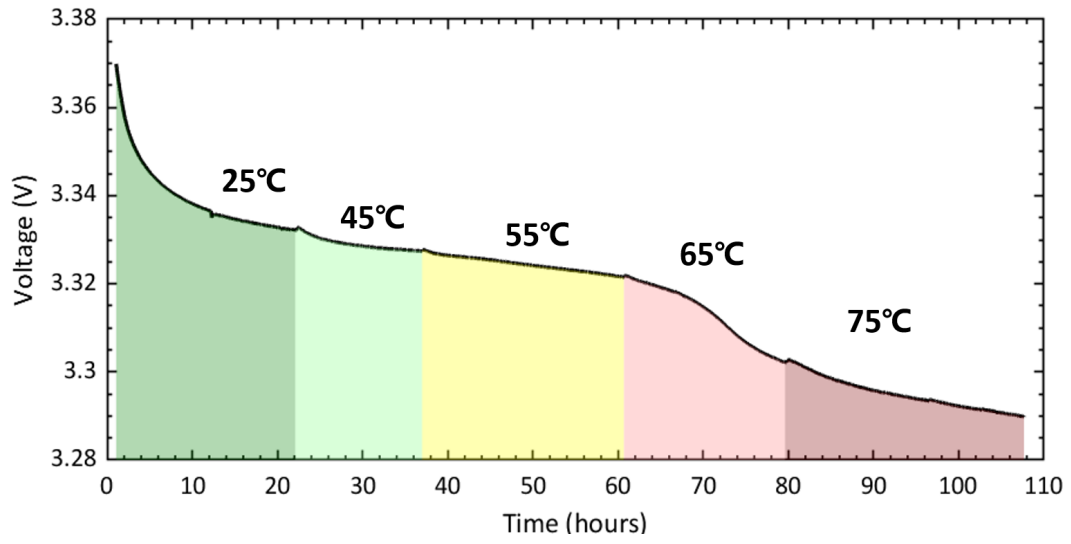


Figure 2-40 Open-circuit voltage of battlet battery in different temperature environment.

CHAPTER 3 **Development of Flexible Wireless**

Chargers

This chapter describes the fabrication and performance of flexible wireless charger based on FlexTrate™ to charge the battlet battery. The design of the wireless charger is optimized from a previous wireless power transfer device to charge the battery at constant voltage. Additionally, the fabrication process and charging ability of the wireless charger are presented.

3.1 Design of wireless power transfer device for charging batteries

Based on previous designed resonant magnetic wireless power transmission (WPT) [12], the design is optimized for charging the battlet battery (LFP/Graphite system) at an optimal frequency of 13.56 MHz. In this work, a thin, highly flexible resonant magnetic wireless power transfer link for Li-ion battery charging was developed on the FlexTrate™ platform [10], [65]. This device integrates commercially available components with a resonant magnetic coupling coil and achieves a 3.3 V output for wireless charging. The device's maximum charging power reached 3.97 mW with 5 V V_{pp} at 13.56 MHz input for a commercial Li-ion coin cell battery, and maintains performance without degradation after 1000 bending cycles at a 5 mm radius, demonstrating its potential for integration into flexible wearable technology.

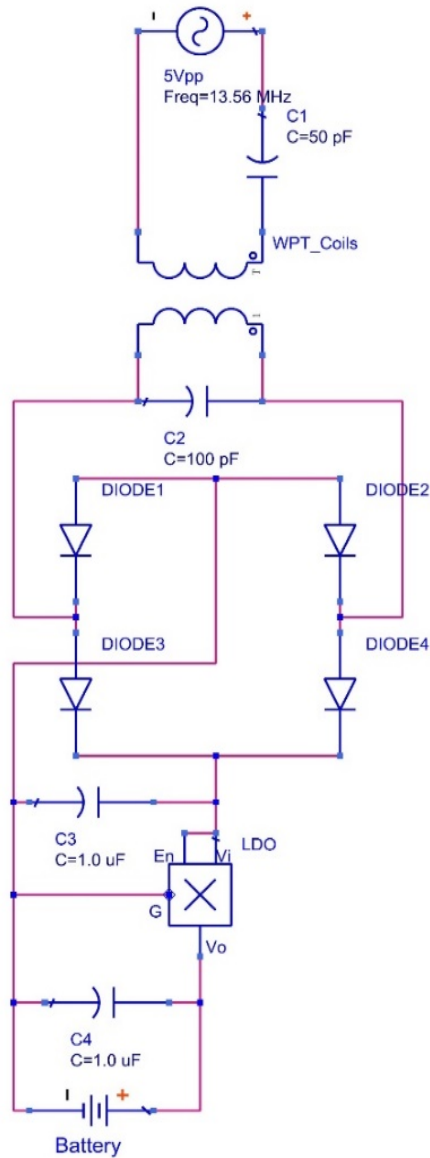


Figure 3-1 Circuit design of the wireless charging system.

The external flexible coil is in 3 cm diameter and has 8 turns as listed in Table 3-2. It is operated under 13.56 MHz with 5 Vpp. The receiving coil is 2 cm diameter and has 5 turns as listed in Table 3-2 Design of the transmission and receive coils.. In the circuit design of shown in Figure 3-1 (© 2022 IEEE). The transmitting and receiving coils require 50 pF series capacitance and 100 pF parallel capacitance to tune the transmitting coil for resonance at a designed frequency. The fabrication process of two flexible coils is based on FlexTrate™ platform and will be discussed

in the next section. Four Schottky diodes are used to build a full wave rectifier bridge to convert the AC output to DC, and a 3.3 V output Low-dropout regulator (LDO) is used to control the output voltage and provide a constant voltage charge device for Li-ion battery with a nominal voltage at 3 V and cutoff voltage at 3.3 V. Two 1 μ F capacitors are placed in parallel at the input and output of LDO as suggested by the LDO specification as decoupling capacitors. The specs and images of the integrated components are listed in Table 3-1 and Table 3-2 (© 2022 IEEE).

Table 3-1 List of components utilized in this study.

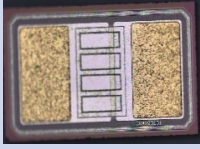

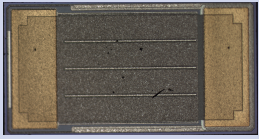
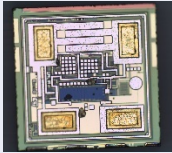

No.	Image	Component	Dimension (L x W x T μ m)	Pad Size (μ m)
1		100 pF Si DT-Cap	1260 x 760 x 400	500 x 300
2		BAT6202-LS (Diode)	620 x 320 x 310	260 x 200
3		1 μ F Si DT-Cap	3460 x 1850 x 400	1600 x 600
4		LDBL20-33R	480 x 480 x 200	114 x 65
5		Li-ion Battery	R = 6270	NA

Table 3-2 Design of the transmission and receive coils.

Feature	External Coil (μm)	Gain Coil (μm)
Inner Diameter	20000	15000
No. of turns	8	5
Wire Spacing	250	100
Line width	400	400
Line Thickness	20	20

3.2 Fabrication process

In the fabrication of the flexible wireless charger as shown in Figure 3-2 (© 2024 IEEE), we employed the FlexTrate™ process [12]. The charger coil design is adapted from our previous work [13]. Initially, thermal release tape is laminated onto the surface of the glass wafer handler. Then, using a pick-and-place tool, functional and passive dies are placed facing down. Next, uncured PDMS is dispensed and molded with a second silicon handler also laminated with thermal release tape. After a 24-hour room- temperature cure of the PDMS, the first handler is released, and the wafer is flipped, positioning the dies facing up. Now, the sample is ready for subsequent wiring processes. In the fourth step, a 1 μm Parylene layer is deposited as a buffer layer, followed by a 5 μm SU8 spin-coat serving as the first dielectric layer for wiring. Following the dielectric layer process, the fifth step involves using 300 W O₂ plasma RIE to open contacts on the dielectric layer. Subsequently, a 20/300 nm Ti/Cu seed layer is patterned, and the wires are thickened to approximately 7 μm by electroplating. This process is repeated to fabricate the second Cu wiring

layer, with SU8 patterned atop the second wiring as the passivation layer. Finally, the second handler is released, yielding a final flexible wireless charger.

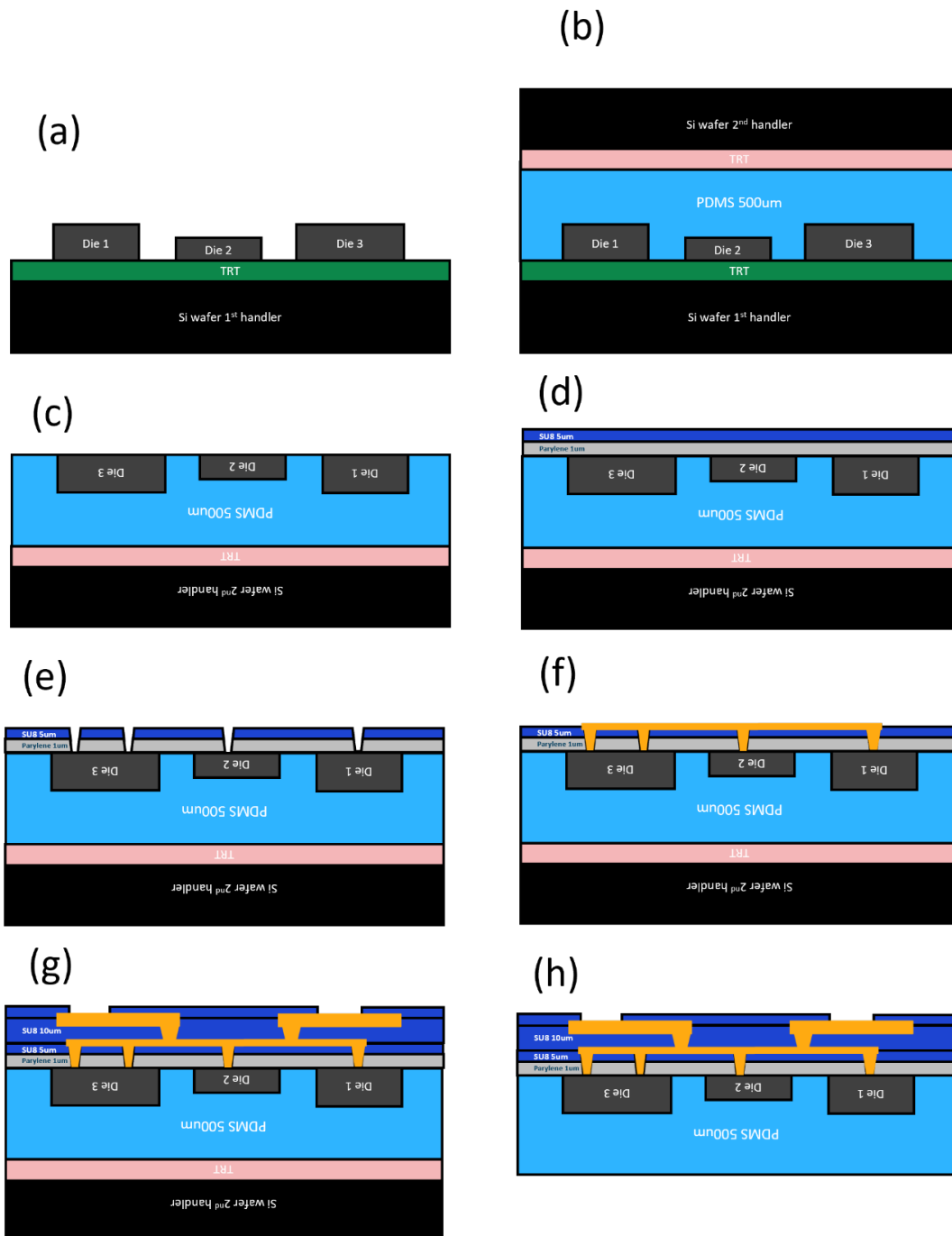


Figure 3-2 Fabrication process of the wireless charger. (a) Die placement on thermal release tape laminated on a silicon handler. (b) Dispense DPMS and mold with 170 °C TRT on 2nd silicon handler. (c) Release of 1st silicon handler.

handler. (d) Deposition of parylene and spin-coat SU8 dielectric layer. (e) Contact opening using RIE dry etch process. (f) Electroplating Cu interconnects. (g) Fabrication of 2nd layer interconnects. (h) Thermal release of the 2nd handler

The fabricated coils are shown in Figure 3-3 (© 2022 IEEE), the total thickness of these flexible wireless charge transmission coil is 525 μm , and the PDMS substrate is 500 μm . The coils can be further thinned down by using thinner teflon ring during molding PDMS process. External wires and sockets are soldered on the exposed pads for connection.

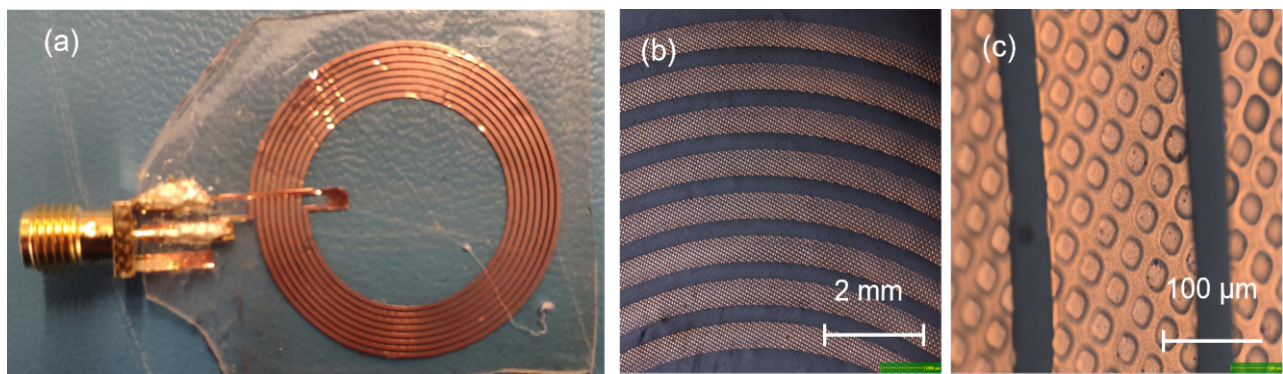


Figure 3-3 Optical image of wireless power transfer coils. (a). transmitting coil; (b) and (c) 8 turns of the transmitting coil, the width is 100 μm while the spacing is 50 μm between each turn.

Figure 3-4 displays different components of the fabricated wireless charger. The LDO image within the figure reveals that the finest wire pitch is approximately 40 μm (20 μm L/S), and the wire thickness is about 7 μm , both fabricated using the electroplating method. Accurate die placement ($< 1 \mu\text{m}$) ensures good alignment across all contacts.

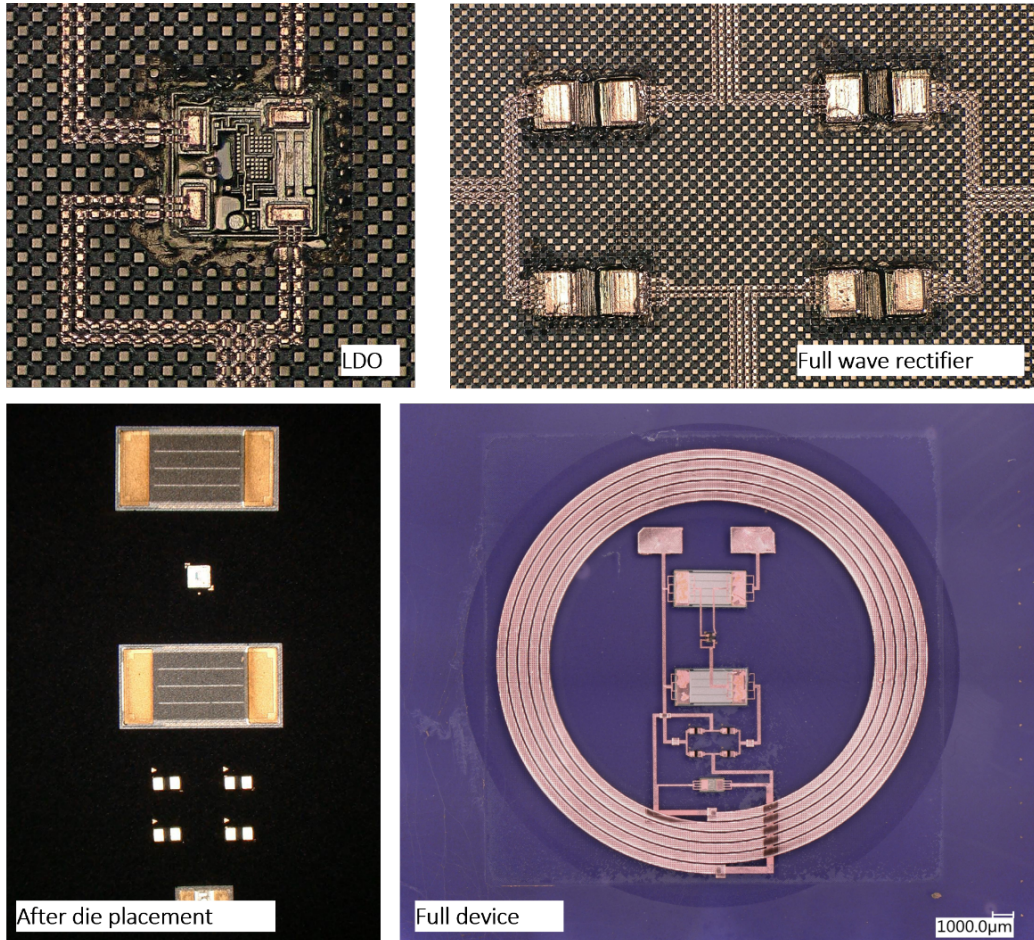


Figure 3-4 Optical images of the fabricated wireless charger. (a) LDO. (b) full-wave rectifier using four diode. (c) Dies align to the substrate with $< 1 \mu\text{m}$ shift after pick-and-placement. (d) fabricated device.

3.3 Electrical performance

The electrical performance of the wireless charger is detailed in Figure 3-5 (© 2024 IEEE). Figure 3-5 (a) illustrates the output voltage of the receiving coil across various coupling frequencies (ranging from 0 MHz to 30 MHz) of the transmission coil, as well as across different coupling distances (0.5 mm, 1 mm, 2 mm, 3 mm). Owing to the LDO design, the wireless charger's maximum output voltage is capped at 3.3 V, with a minimum enabled voltage of approximately 1.1 V. The working frequency range of the wireless charger increases as the coupling distance decreases. At a 0.5 mm coupling distance, the receiving coil demonstrates the widest working

frequency range, from 11.5 MHz to 18.6 MHz, which ensures a steady 3.3 V output voltage and aligns with the designed coupling frequency of 13.56 MHz. At coupling distances greater than 2 mm, such as at 3 mm, the maximum output voltage drops to 1.6 V due to efficiency losses, which fails to meet the battery charging requirements. Consequently, the design's maximum coupling distance is established at 2 mm. Figure 3-5 (b) shows the wireless charger's bendability by keeping the transmission coil flat while bending the receiving coil at various radii to simulate real-world conditions. All tests are conducted at 5V V_{pp}, 13.56 MHz, and a 0.5 mm coupling distance. The results indicate that the wireless charger survives at 3.3 V output up to a 15 mm bending radius. Beyond this radius, the output voltage gradually declines to 0 V at a 5 mm bending radius. Previous studies have demonstrated that the FlexTrate™ process supports up to 1 mm of mechanical bendability, suggesting that the limitations of the flexible wireless charger are electrical rather than mechanical.

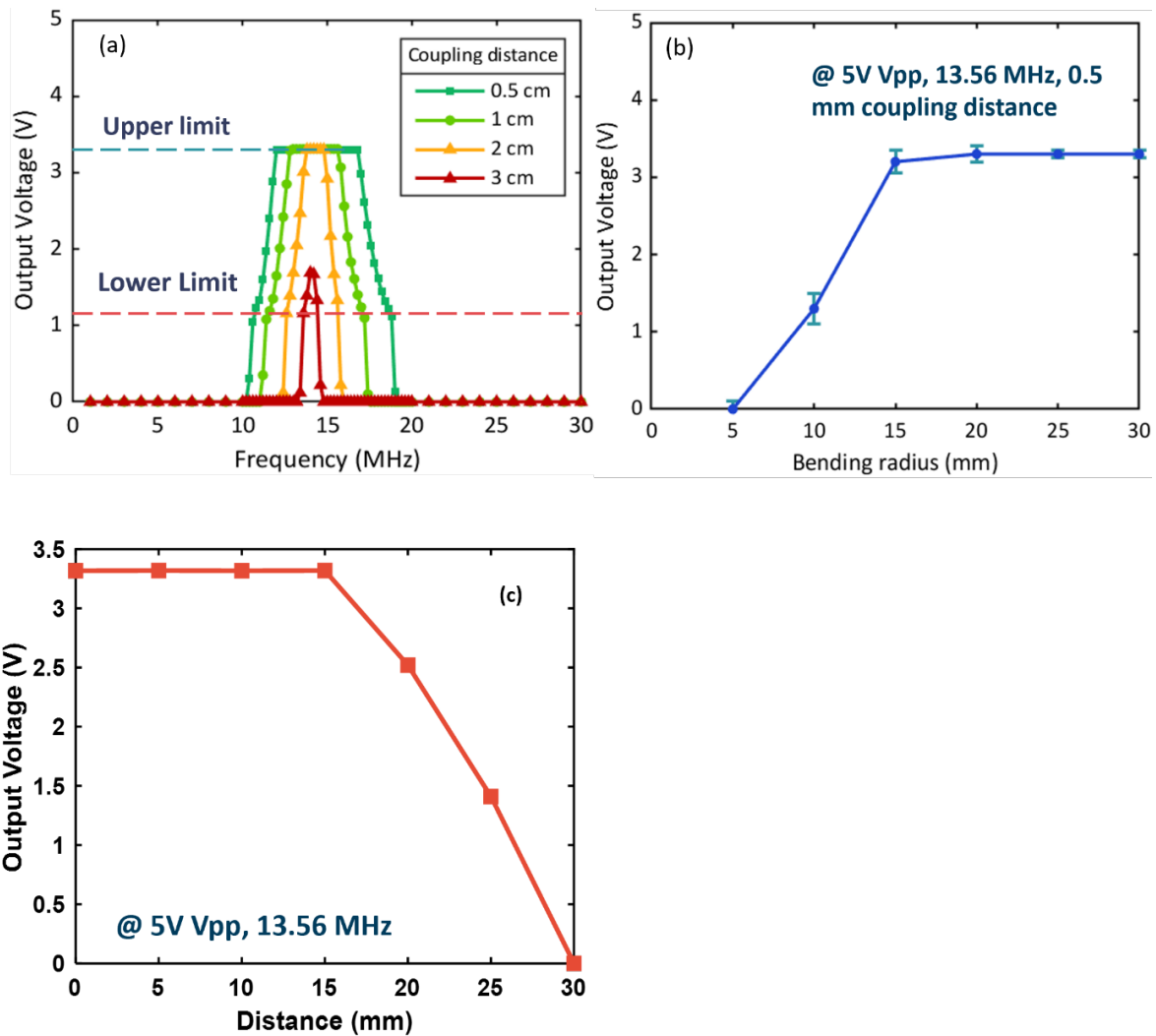


Figure 3-5 Electrical performance of the wireless charger (a) output voltage in different coupling frequencies and coupling distances; (b) Output voltage vs. bending radius; (c) Output voltage vs. coupling distance.

In addition, the effect of the offset on the output voltage is measured. As illustrated in Figure 3-6 (© 2021 IEEE), the output is plotted as a function of the offset. The output voltage maintains a constant level at 3.319 V. Once the outer circumference of the external coil passes the center of the receiving coil, the output voltage begins to drop. The maximum offset distance is 30 mm, at which point the two coils are completely separated from each other. Figure 3-6 (a) to (d) displays the various offset modes of the two coils.

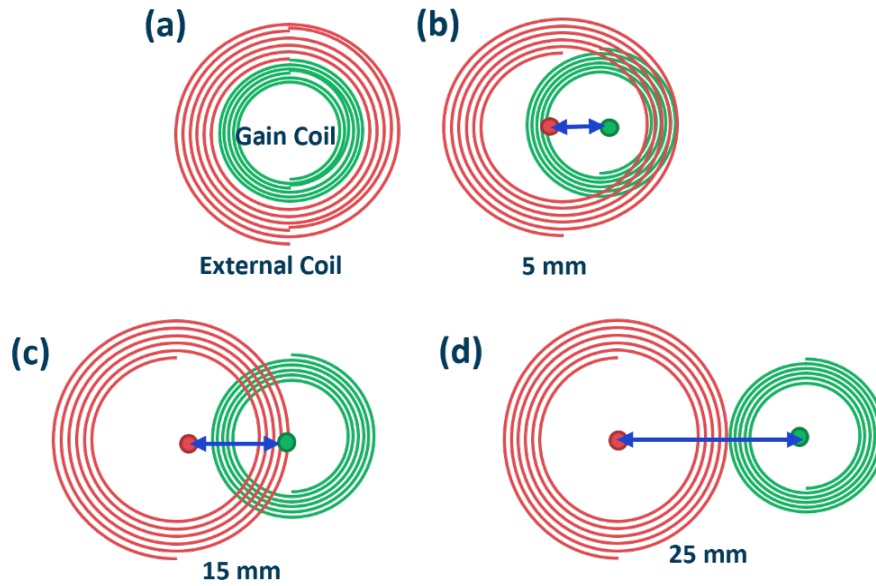
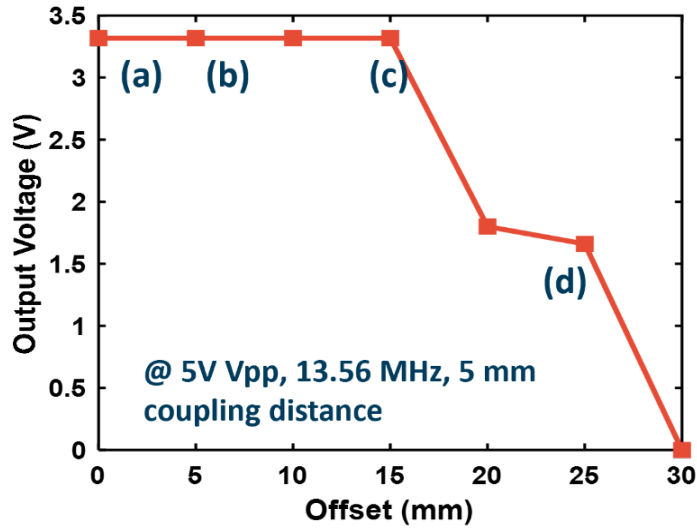


Figure 3-6 Output voltage at different offset distance at 5V Vpp, 13.56 MHz (top) output voltage vs offset. (bottom) Illustration of different offset mode (a) 0 mm, two coils are concentric; (b) 5 mm, two coils are internally tangent; (c) 15 mm, external coil passes the center of internal coils; (d) 25 mm, two coils are externally tangent. Orange coil is the external coil while the yellow coil is the gain coil.

3.4 Bendability

The bendability of the flexible coils was assessed by measuring the resistance of both coils. Figure 3-7 (© 2021 IEEE) presents the measured resistance during bending. The initial resistance is 5.69 Ω for the external coil and 2.37 Ω for the receiving coil. The external coil exhibits higher

resistance due to the greater total wire length compared to the internal coils. According to Figure 9, there is no significant change in resistance after bending both coils. The variations in resistance are 6.2% for the receiving coil and 3.4% for the external coil. These results indicate that the flexible wireless charging coils possess excellent mechanical bending reliability.

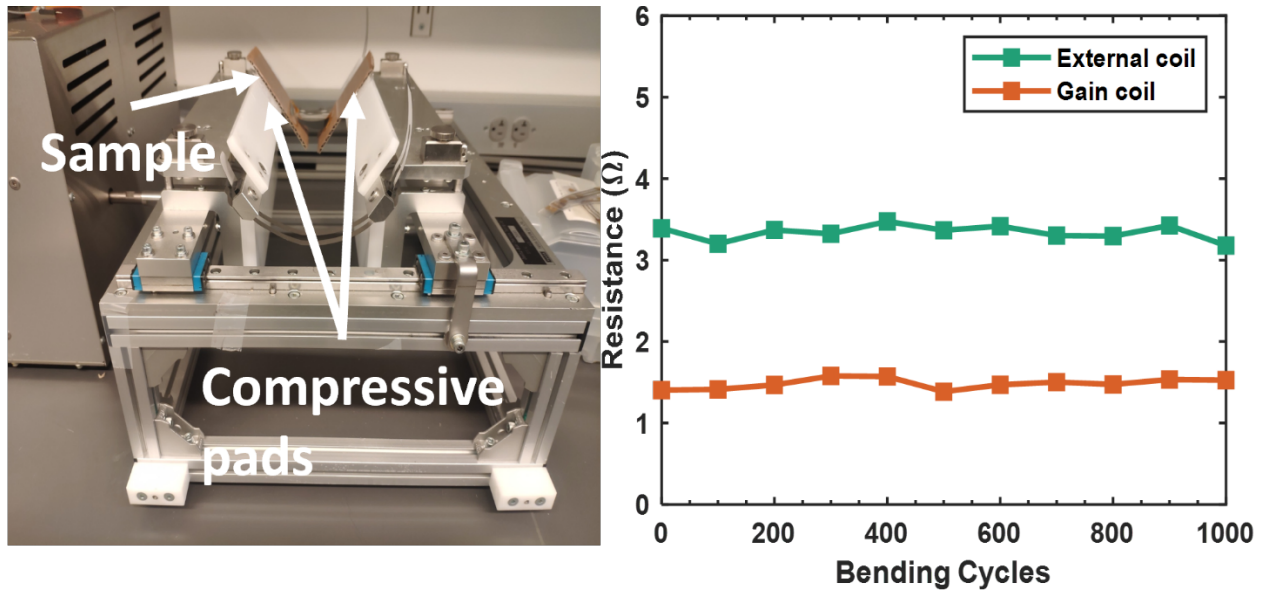


Figure 3-7 Bending test of the wireless charger. (left) test setup. (b) The resistance of two power transfer coils bended in 5 mm bending radius in cumulative number of bending cycles up to 1000 times

3.5 Charging ability

Figure 3-8 (a) (© 2024 IEEE) displays the output voltage and passthrough current of the charger across different loading resistances from 100 ohms to 10,000 ohms. At 100 ohms, the current peaks at 2.5 mA and the voltage at 1.1 V. As loading resistance increases, the output voltage rises to 3.3 V and the current decreases to 1.3 mA at 2200 ohms. Further increasing the loading resistance maintains the output voltage constant, while the rate of current drop slows down. This indicates that the charger can initially charge the battery in constant power charge mode (3.9 mW), and as the battery reaches full capacity (3.3 V), the charger can transition to a 3.3 V constant voltage charge to prevent overcharging. Figure 3-8 (b) (© 2024 IEEE) shows the charging profile

of the device when charging a coin cell Li-ion battery. The supply voltage of the transmitting coil is under V_{pp} at 5V and 13.56 MHz. The Li-ion battery is discharged to a state of 1.9 Voc (open circuit voltage). The charging current and the output voltage is measured by a multimeter. The profile shows 3 stages of charging Li-ion battery. In the first stage (Stage I, 0 – 30 mins), the output voltage is linearly increasing from 2.85 V to 3.3 V, while the charging current linearly decreases from 1.39 mA to 1.1 mA. The maximum charging power is 3.9 mW at the beginning of the charging. In the second stage (Stage II, 30 – 400 mins), output voltage reaches the upper limit, due to the increasing of chemical potential, the current is still decreasing while the decreasing rate is also reducing. Finally, at the stage III (400 – 600 mins), the charging current reaches cutoff current 0.02 mA, and the battery is considered fully recharged.

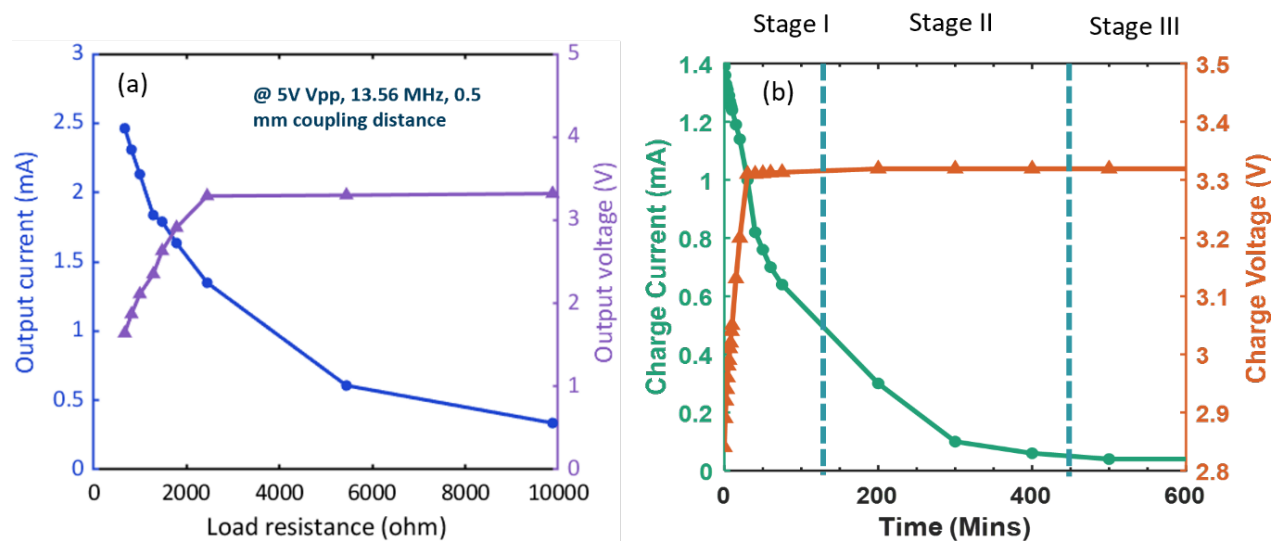


Figure 3-8 (a) Output voltage (purple) and passthrough current (blue) of the wireless charger in different loading resistances. (b) Charging voltage (orange) and charging current (green) of the wireless charger when charging a flexible battery.

CHAPTER 4 Integration of the FlexPower with wearable devices

After the development of the flexible battlet battery and flexible wireless charger the integration of these two components needs to be addressed to create a complete FlexPower solution for wearables. In this chapter, we propose two integration approaches: the 2D and 3D structures. The difference between the 2D and 3D structures is discussed in detail, and an application of FlexPower by powering microLED arrays is also presented in this chapter.

4.1 2D flexible FOWLP

4.1.1 Circuit design of integration with μ LED array

To demonstrate the functionality of the flexible battlet battery and the wireless charger, two components are integrated with a flexible μ LED display. The circuit design and the layout of the system is shown in Figure 4-1 (a) and (b). In this system, the wireless charger is connected with a flexible battery and there is a dome switch in between the battery and the microLED array to control the on/off of the 33 microLED array. The size of the battery and wireless charger are 5 mm, the size of the dome switch GX05170 is 5.3 mm from Snaptron with minimum 170 g trip force. The total size of the sample is 4 x 6 cm².

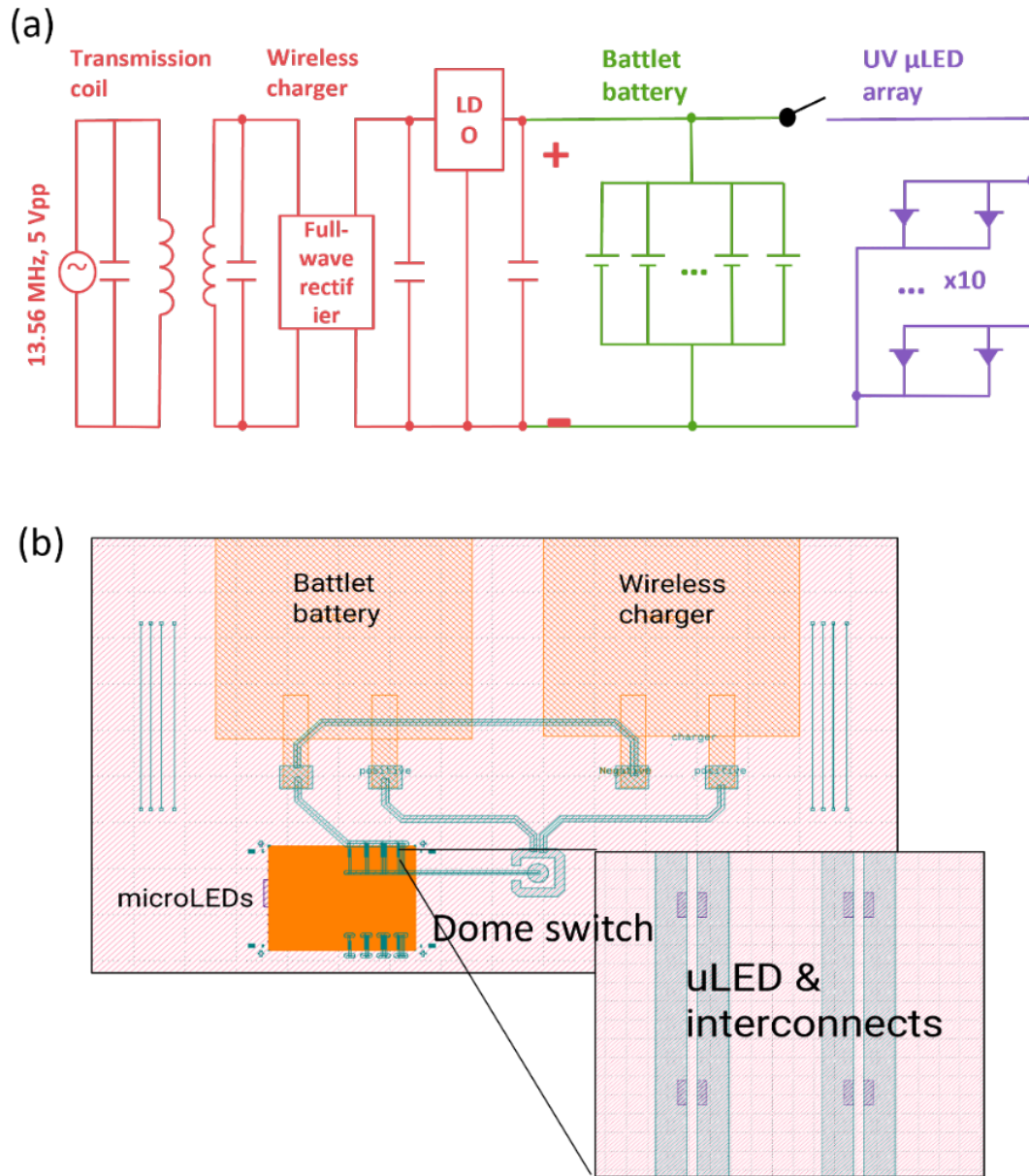


Figure 4-1 (a) Circuit design of the 2D integration of battery, wireless charger and microLEDs. (b) Design layouts

4.1.2 μLED array characteristics

Figure 4-2 (a) (© 2024 IEEE) presents an optical image of the μLED array. Each UV LED measures $30 \times 30 \mu\text{m}^2$ with a typical wavelength of near 400 nm shown in (b), designed as the backlight for the display [70]. The integration of the μLED array into the FlexTrate™ platform via the Laser Lift-Off process is detailed in the previous work [71].

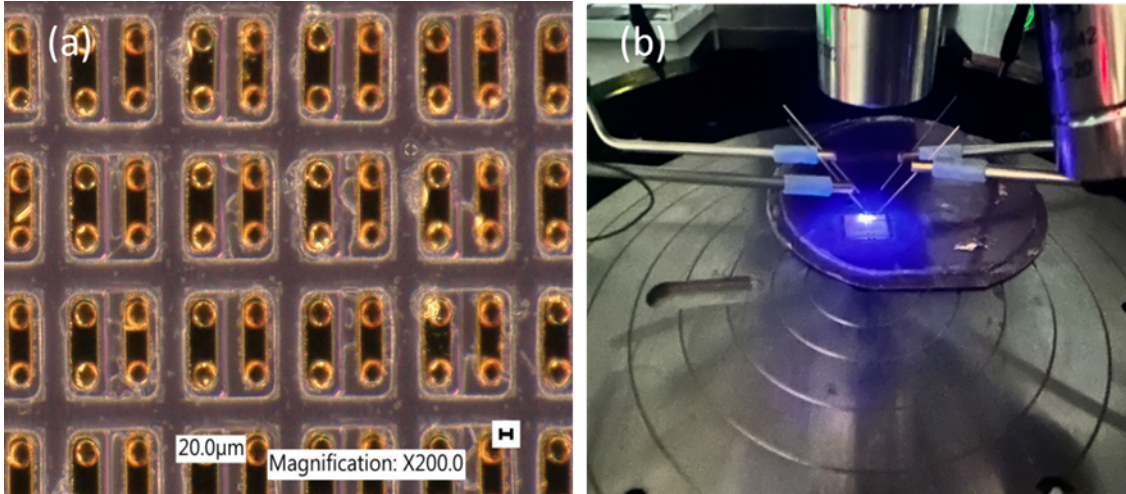


Figure 4-2 (a) optical images of the μ LED array. (b) the LEDs emit near-UV light powered by external source.

The I-V curve of each μ LED is depicted in Figure 4-3 (a) (© 2024 IEEE). The results indicate that the forward voltage of the μ LED is 2.9 V, and the current is 0.03 mA at the nominal voltage of the flexible battlet battery (3.1 V). This corresponds to a power consumption of 0.091 mW. Figure 4-3 (b) shows the relative light intensity of the LED, which increases exponentially with the applied voltage above the 2.9 V forward voltage.

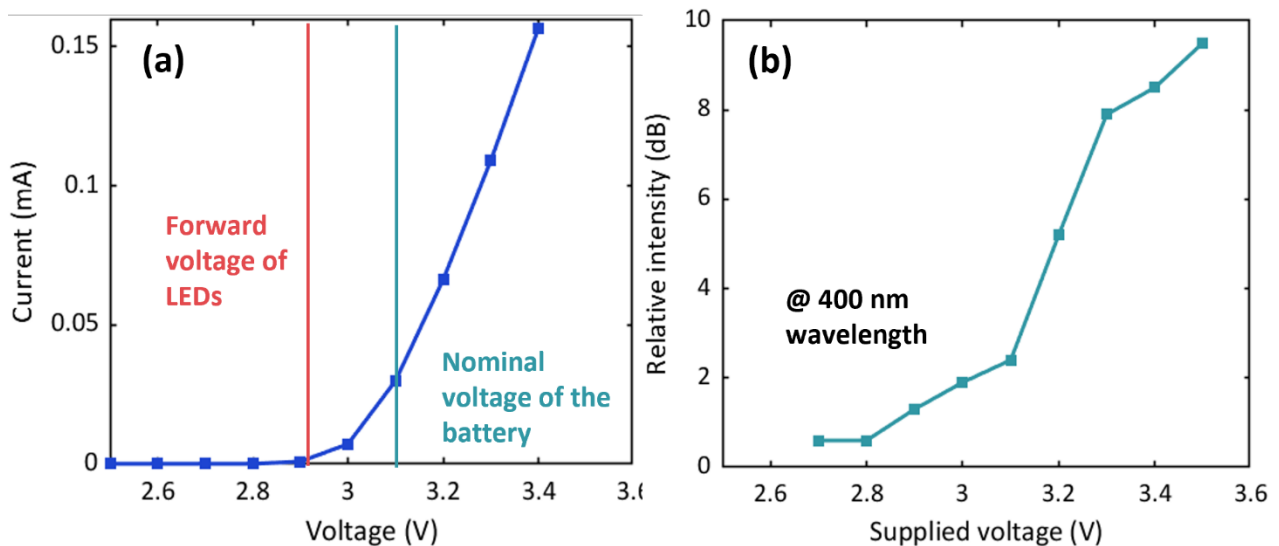


Figure 4-3 (a) optical images of the μ LED array. (b) light intensity of the μ LED in different external voltages.

4.1.3 Integration of FlexPower with μ LED array

The integrated sample, shown in Figure 4-4 (a) (© 2024 IEEE), measures 4 x 6 cm² with a total thickness of about 1 mm. Components are interconnected using low-temperature solder Sn-57Bi-1Ag, applied via inkjet printing. The contact sizes for battery-to- μ LED and wireless charger-to- μ LED connections are specified in the figure. Figure 4-4 (b) (© 2024 IEEE) displays the integrated sample in a bending state. The total power consumption of the LED array is approximately 3 mW, allowing the integrated, device at a bending state.

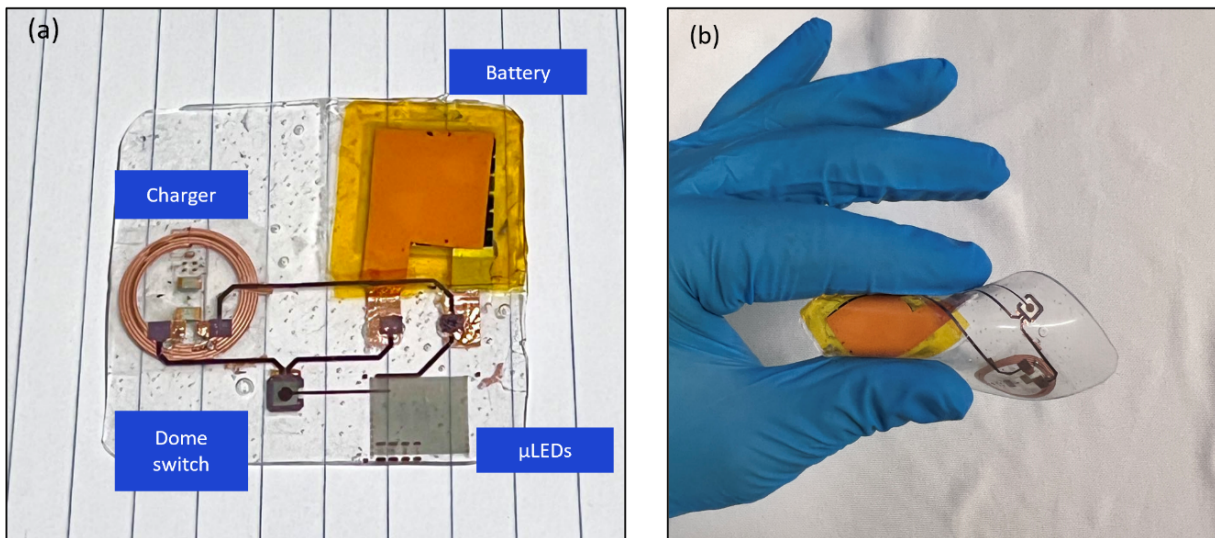


Figure 4-4 (a) optical image of final integrated sample, and (b) at bending state.

The device is integrated with a total energy of 4.5 mWh battery, which can power the μ LED array for 1.5 hours on a single charge. Figure 4-5 shows that the LEDs are lit up when pressing the dome switch and the output voltage during operation is measured at 3.03V. While the voltage comes back to 3.26 V when LEDs turn off.

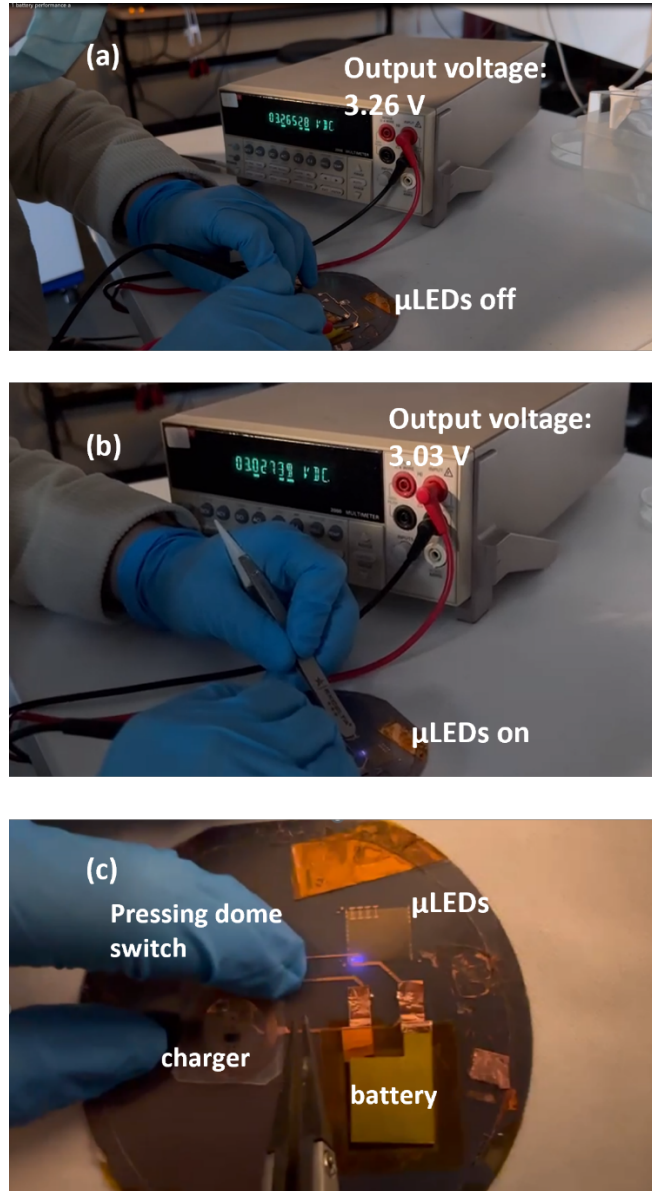


Figure 4-5 (a) Measurement of battery output voltage at microLEDs off state, and (b) at LED off state. (c) the operation of the microLEDs by pressing the dome switch

To demonstrate the capability of the wireless charger, the integrated battery was first depleted below the LED's forward voltage, rendering it unable to illuminate the LED. Subsequently, the battery underwent wireless charging. The charging protocol consisted of a cycle where the battery was charged for 15 minutes and then allowed to rest for 5 minutes to mitigate polarization effects. Following each cycle, the device was activated manually, and the light intensity was

measured using the apparatus depicted in Figure 4-6 (a) and (b) (© 2024 IEEE). The results indicate that during the initial 45-minute period of charging and discharging cycles, there was a progressive increase in light intensity corresponding to the charge time. However, beyond 45 minutes, the light intensity plateaued at approximately 2.2 dB. This behavior is characteristic of the LFP (lithium iron phosphate) battery system, wherein the voltage exhibits an initial rise during the charging process and subsequently stabilizes at a constant plateau voltage of 3.2 volts, a phenomenon attributed to the phase transition in the LFP material [72], [73].

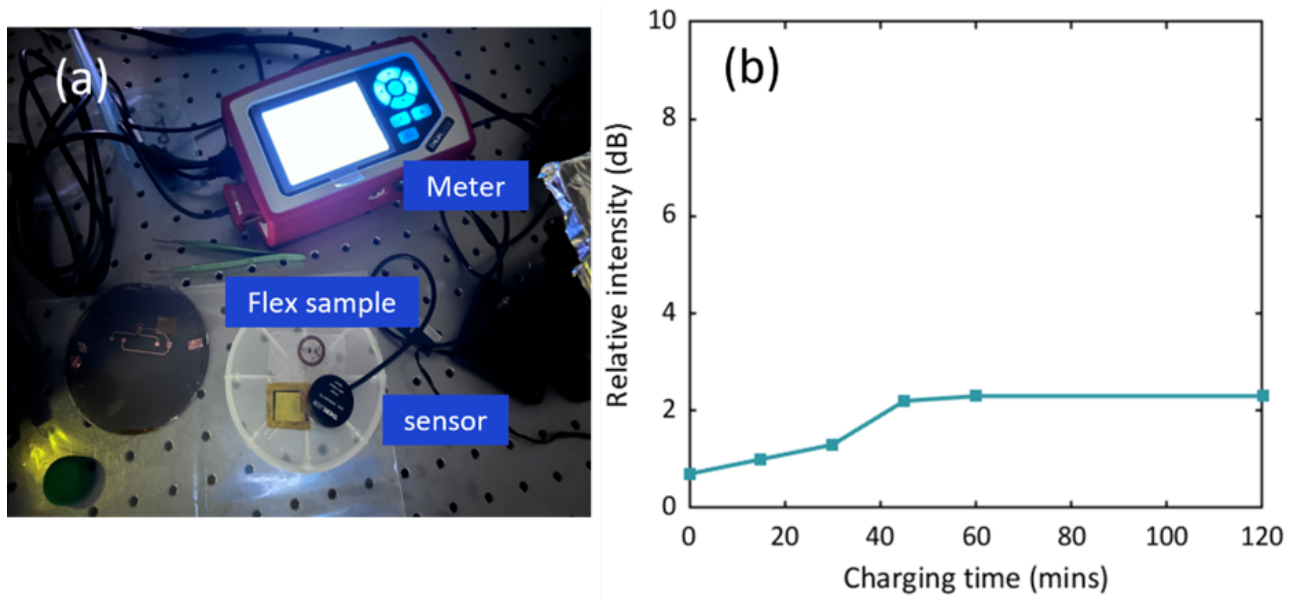


Figure 4-6 (a) Experiment setup for LED light intensity measurement. (b) LED intensity change during the wireless charging of the battery.

4.2 3D flexible FOWLP

Rigid 3D FOWLP usually entails a direct bonding of two dies which then inter-communicate by Through-Si Vias (TSVs). Alternatively, they can be interconnected by solder or wires [74], [75]. In the past, Fukushima et al. proposed to interconnect the front and back of Cu using Cu posts [76]. They treated Cu posts as a die and used a pick and place tool for the die first

process and used a soluble polymer to open backside contacts. One drawback is that the number of IOs that can be connected is reduced additionally. PDMS with better biocompatibility was not utilized.

Therefore, we propose for the first time to use TGVs as a channel for energy transfer and etch the PDMS on the backside of TGVs by dry etching to open contacts. In this architecture, the wireless charging module and the flexible Li-ion battery are on the backside of the wearable device, and through the RDL layer on the backside and TGVs, energy is transmitted to the front of the wearable device, then further transmits energy to the corresponding power-using devices through the RDL layer on the front. Compared to materials such as Cu pillar, liquid metal, or conductive polymers, the use of TGVs dies allows for lower resistance, smaller form factor, and higher package reliability.

4.2.1 Through Glass Vias

The TGVs utilized in this work are provided by 3D Glass Solutions Inc. (3DGS). TGVs are essential components in 3D integration, as they allow for the transfer of electrical signals and power between different layers of the package. In addition, the dry etch process would not damage the surface of these TGVs. Key findings indicate that the dry etch process is unlikely to cause any harm to the TGVs' surface, whereas it can potentially cause substantial damage to the silicon die surface [77], [78]. The via's dimensions are critical for its effectiveness. In this work a minimum pitch of 100 μm is chosen for optimal performance. As illustrated in Figure 4-7 (© 2023 IEEE), the die dimensions measure 1 x 1.2 mm, with a thickness of 0.3 mm, which is also the height of the vias. The vias' diameter is 40 μm resulting in an aspect ratio greater than 7.5. The minimum pitch of the via design is 100 μm .

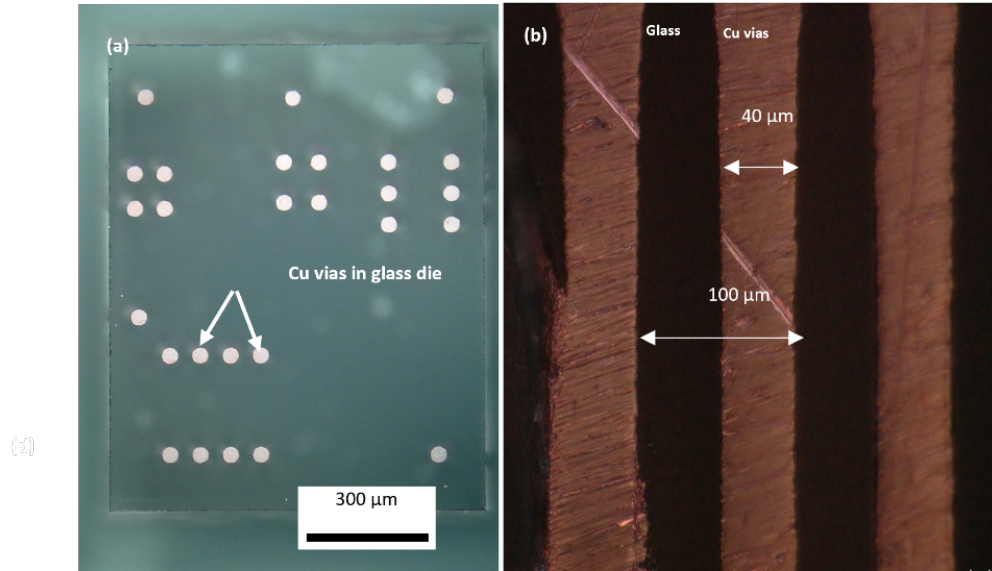


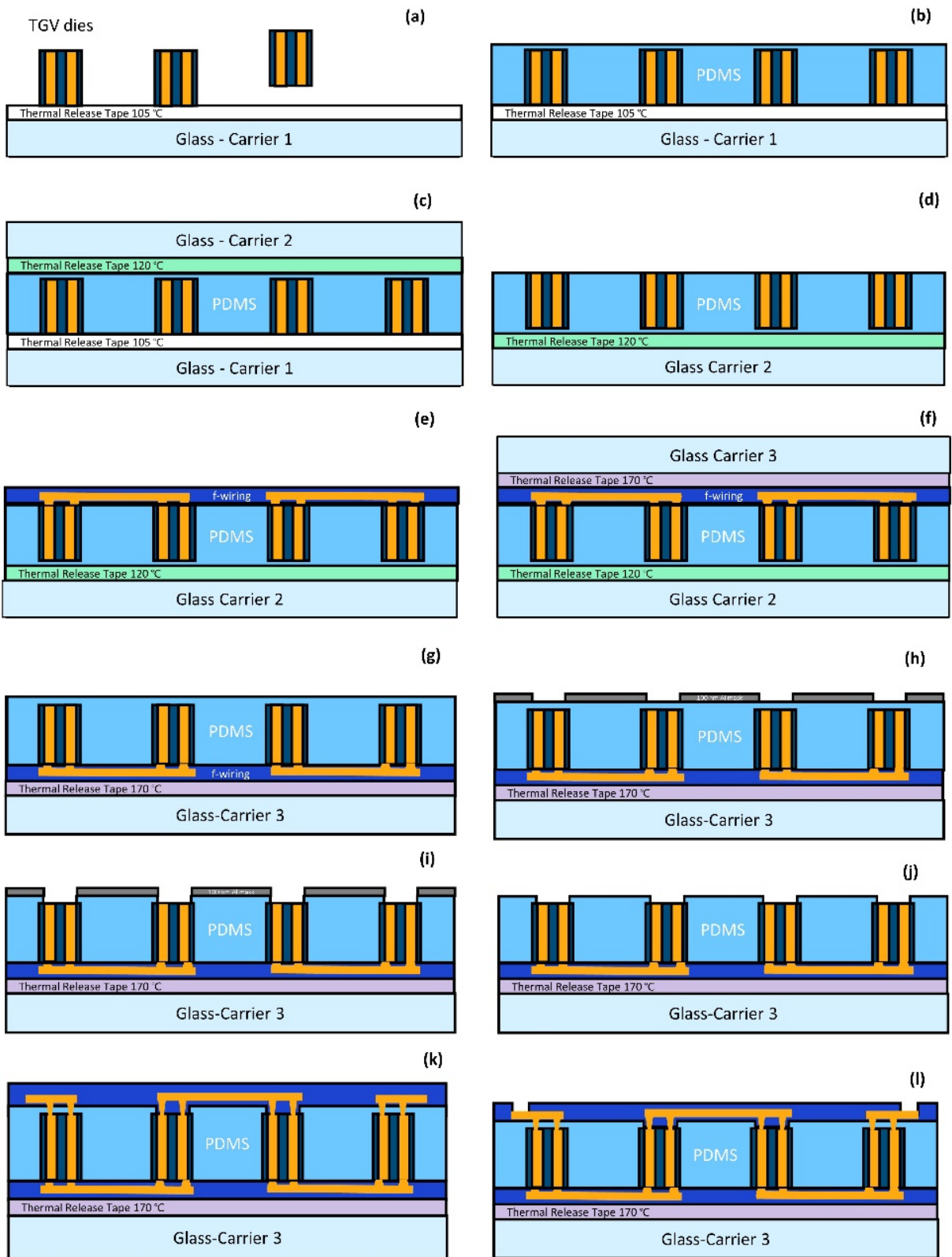
Figure 4-7 (a). The optical image of through glass die. The size of the die is 1 x 1.2 mm. Total thickness of the die is 300 μm. The Cu pillar is 40 μm diameter, and the minimum pitch is 100 μm; (b). Backside vias; Interconnection on the glass die after electroplating. The interconnection of the Cu wire is 40 μm pitches.

4.2.2 Fabrication process

The fabrication process of the flexible 3D Fan-Out Wafer-Level Packaging demonstrated in this study is depicted in Figure 4-8. Step (a) to step (e) are similar to previously defined FlexTrate™ process. First, in step (a), the TGV dies are placed on the first carrier, which is laminated with 105°C thermal release tape, following the conventional FOWLP process. In step (b) uncured PDMS with a base-to-cure agent ratio of 10:1 is dispensed on top of the carrier. The sample is then molded with a 2nd silicon carrier that is laminated with 120°C thermal release tape. In step (c) the sample is degassed and cured in a vacuum chamber at room temperature for 24 hours. After the curing process in step (d), the 1st carrier is released by heating the substrate up to 105°C for 1 mins. After released the 1st handler, the top side PDMS is etched and dies are oriented facing up. Next, in step (e) a single-layer interconnects is fabricated on top of the sample. The interconnects layer comprises a 2-μm-thick parylene C layer, which acts as a dielectric layer with

SU8 2005 corrugation design, while the metal interconnects are approximately 5 μm thick and consist of electroplated copper wire.

After the fabrication of the 1st layer interconnection, step (f) to step (k) are developed for the fabrication on the back side interconnection on 3D FlexTrate. In step (f) the sample is laminated with a third carrier layer that has laminated with thermal release tape. The 2nd carrier is released like the 1st carrier and the backside of the PDMS and TGV dies are exposed. In step (h) a 100 nm Al mask are deposited using evaporation deposition and patterned using lift-off process. In step (i) the RIE dry etch process, which utilizes Oxygen and Sulfur Hexafluoride gas, is employed to dry etch the backside PDMS and open the backside contacts, and the Al mask are removed using wet etch method shown in step (j). The details and results will be discussed in the following chapter. In step (k) the backside interconnects are fabricated using the same method as the front side interconnection layer. Finally, in steps (m) to (o) and the sample can be bonded to another sample to form a 3D structure.



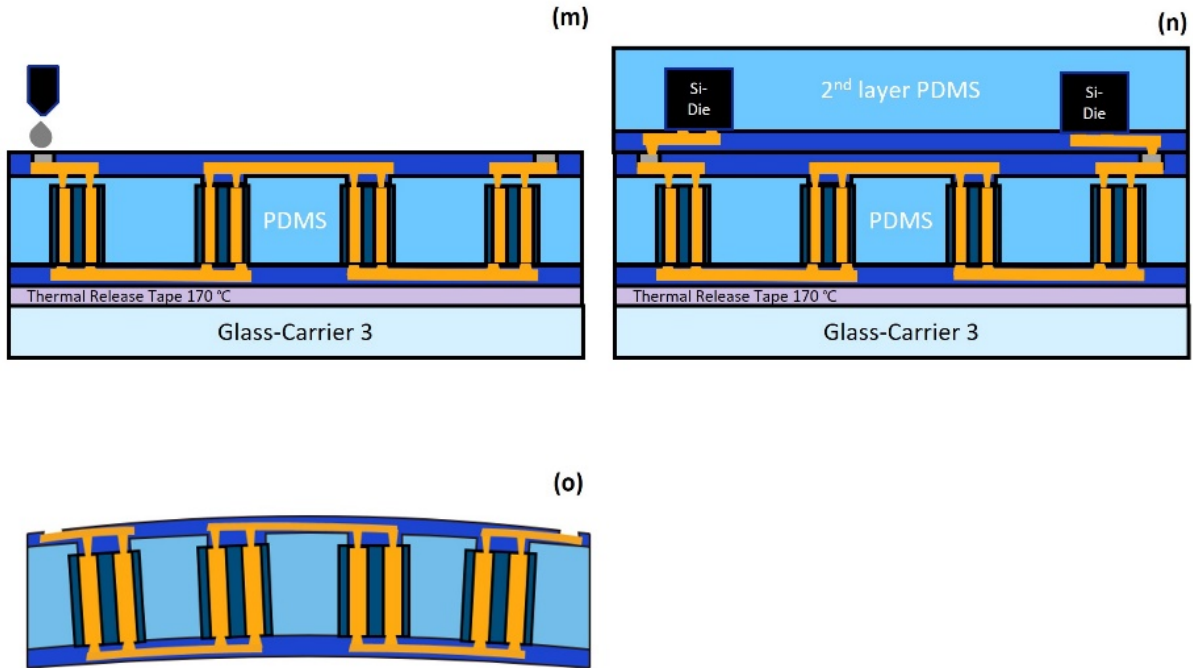


Figure 4-8 Fabrication process flow of flexible 3D integration. (a). Placement of TGVs. (b) and (c). Molding and curing of flexible PDMS polymer with the 2nd glass carrier and 120 °C. (d). Release of the 1st glass carrier by heating up to 105 °C. (e) Semi-additive process for the Cu RDL interconnection as same as FlexTrate™; (f). Lamination of 170 °C thermal release tape and 3rd glass carrier for backside RDL process. (g). Release of the 2nd carrier. (h). Deposition of 100 nm Al using lift-off method. (i). Dry etch of PDMS for opening the back side contacts. (j). Wet etch of the Al hard mask. (k). Fabrication of 2nd RDL (l). Open the contact on the interconnection by dry etch method. (m). Deposition of silver paste by Inkjet printing method. (n). Place a 2nd layer of the FlexTrate for bonding. (o). Release of the 3rd handler.

4.2.3 PDMS dry etch process

In the previous section, we discussed the importance of using a dry etch process to facilitate interconnection of different layers of devices. In this study, we investigated the RIE plasma dry etch process for dismantling the PDMS crosslinking and characterizing its effects on patterning accuracy. We used SF₆:O₂ = 80:20 sccm as the etch gas and maintained a total etch time of 30

minutes for each sample, with 1 minute of rest after 5 minutes of continuous etch to cool the samples down.

To prepare the samples, we first evaporated a 100 nm Al metal layer directly on top of a spin-coated 4-inch polished Si wafer as shown in Figure 4-9 (© 2023 IEEE). We then designed circular etch areas of varying sizes and fabricated them using the lift-off process. The diameter of the designed circular sizes was 400 μm , 350 μm , 300 μm , 200 μm , 150 μm , 100 μm , 40 μm , and 20 μm , respectively.

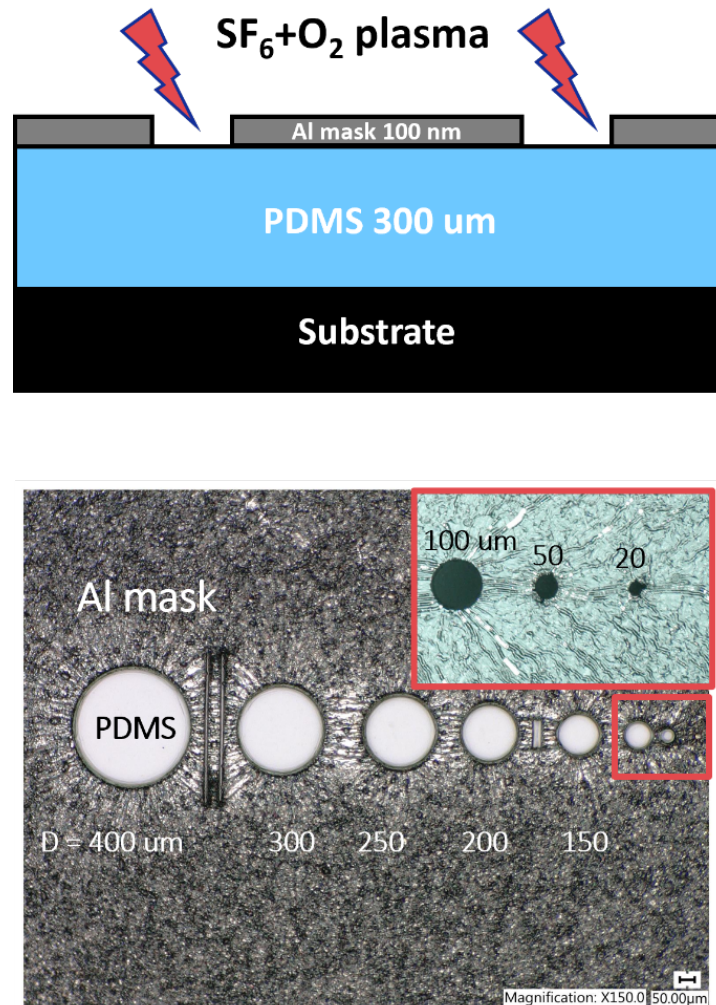


Figure 4-9 (a) Structure of test sample. spin-coated PDMS evaporated with 100 nm Al hard mask for plasma etching. (b) Top view of the prepared sample with opening contact from 400 μm diameter to 20 μm diameter.

The effect of etch power and pressure on the etch rate was explored to determine the optimal process window for best etch profile and throughput. Figure 4-10 (© 2023 IEEE) shows that the etch rate variation with different etch power. With the rates of 0.05, 0.11, 0.24, and 0.34 $\mu\text{m}/\text{min}$, the process is conducted in the power at 50 W, 100 W, 200 W, and 250 W, respectively. The figure also indicates that the etch rate is linearly proportional to the dry etch power. The etch pressure was 150 mTorr in all cases.

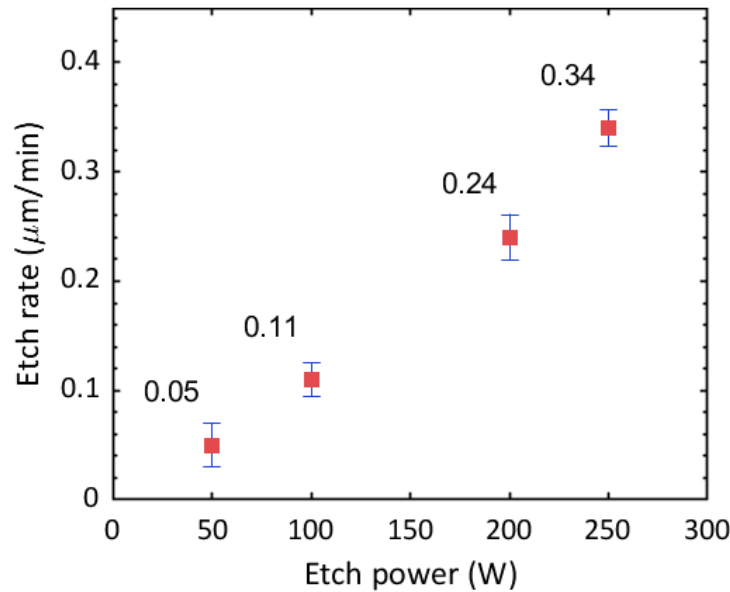


Figure 4-10 Plot of etch power vs etch rate.

Figure 4-11 (© 2023 IEEE) shows that the etch rate increases with increasing etch pressure, with rates of 0.15, 0.34, 0.40, and 0.49 $\mu\text{m}/\text{min}$ at 50 mTorr, 100 mTorr, 200 mTorr, and 270 mTorr, respectively. The maximum etch capability of our current RIE tool for this sample is 270 W and 270 mTorr.

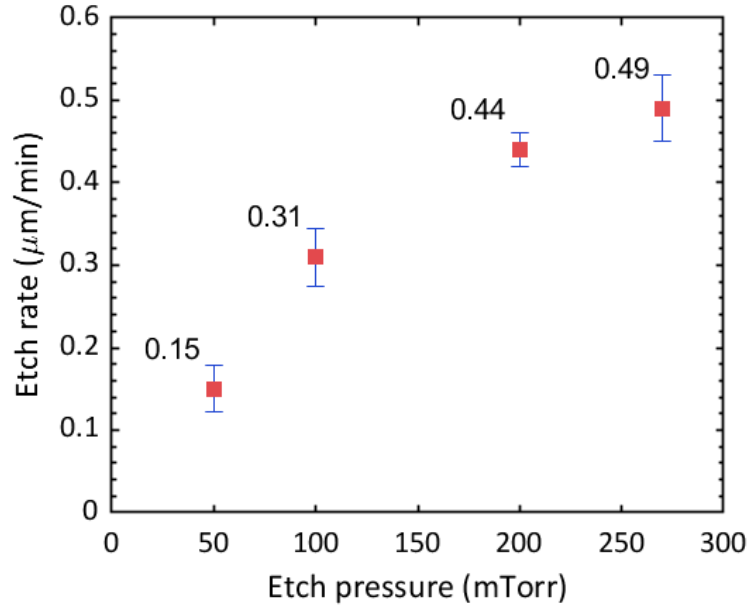


Figure 4-11 Plot of etch pressure vs. etch rate.

The etch uniformity and resolution were measured using a surface profiler, as shown in Figure 4-12 (© 2023 IEEE). Under the maximum etch pressure and power, the etch bottom is close to 90° , indicating a sharp and clear etch profile.

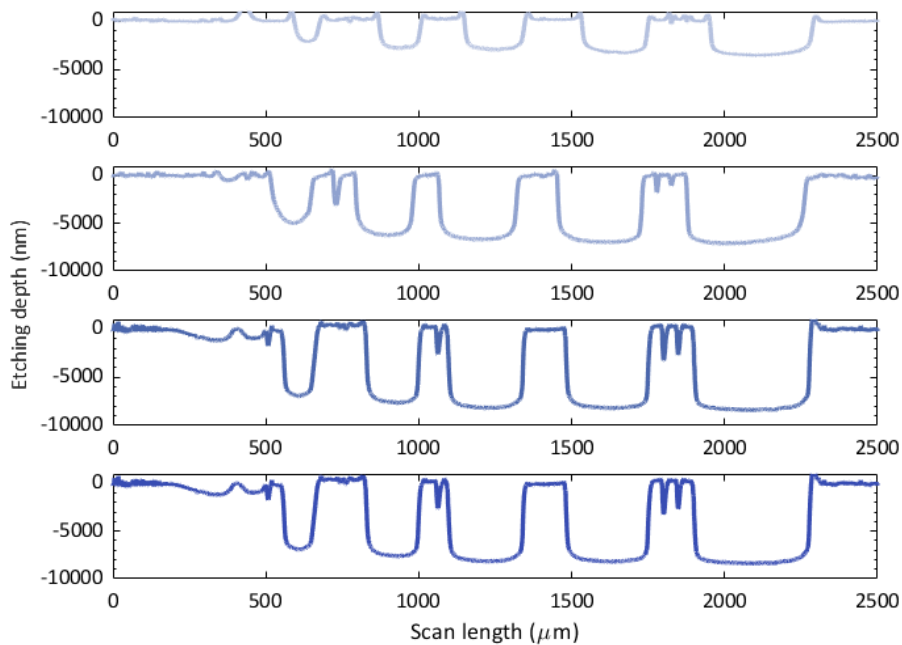


Figure 4-12 Etching profile under different etch pressure measured by surface profiler.

Figure 4-13 (© 2023 IEEE) is the optical profile under different etch pressure aligned with Figure 4-12 respectively from top to bottom. From the images, it is shown at low etch pressure, the profile has a larger etch pitch size. At 250 W and 50 mTorr, the profile has a minimum 200 μm etch pitch. For the feature lower than 200 μm , the surface of the exposed contact starts to be smooth and reflective under microscope, which indicates a non-etched surface as the PDMS surface is as smooth as pre-etch. At the 250 W etch power and etch pressure, the minimum etch feature is about 150 μm . And the etch profile is cleaner.

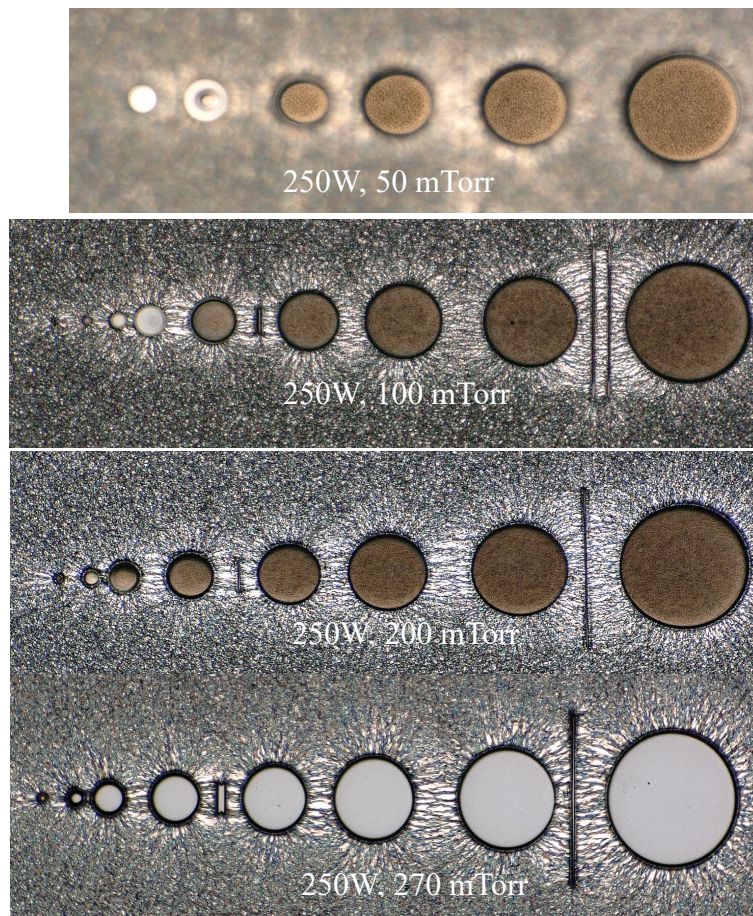


Figure 4-13 Etching profile under different etch pressure from 50 mTorr to 270 mTorr measured by optical microscope.

As shown in the optical image of the etch surface at 200 W etch power and 100 mTorr pressure in Figure 4-14 (© 2023 IEEE). For features larger than 150 μm , the unmasked PDMS is

etched uniformly. However, for features at 150 μm the edge of the PDMS is not etched well due to the shadowing effect of the metal mask and the plasma angle of the tool.

Increasing the etch power and pressure can reduce the shadowing effect, but for features smaller than 150 μm , the etch rate of the PDMS will still be slowed down.

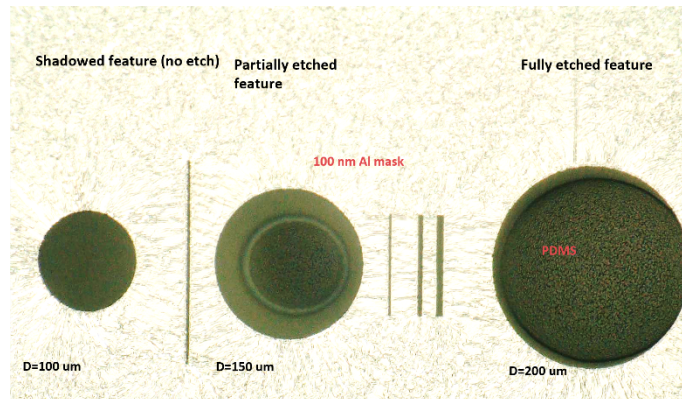


Figure 4-14 Optical image of the etched features shows shadowing issue of dry etching for feature size smaller than 150 μm diameter.

The study of the surface morphology of PDMS before and after the dry etch process is conducted using Atomic Force Microscopy (AFM), as depicted in Figure 4-15 (a), (b), and, (c) (© 2023 IEEE). Figure 4-15 (a) displays the surface roughness of the unetched PDMS, (b) represents the masked PDMS surface after plasma etch, and (c) illustrates the etched PDMS surface. The root mean square surface roughness (R_s) of the samples are measured to be 5.112 nm, 5.971 nm, and 16.52 nm respectively. The results indicate that the surface roughness of the samples does not increase after the dry etch process if the Al hard mask is used for patterning and protection, which is beneficial for subsequent RDL processes.

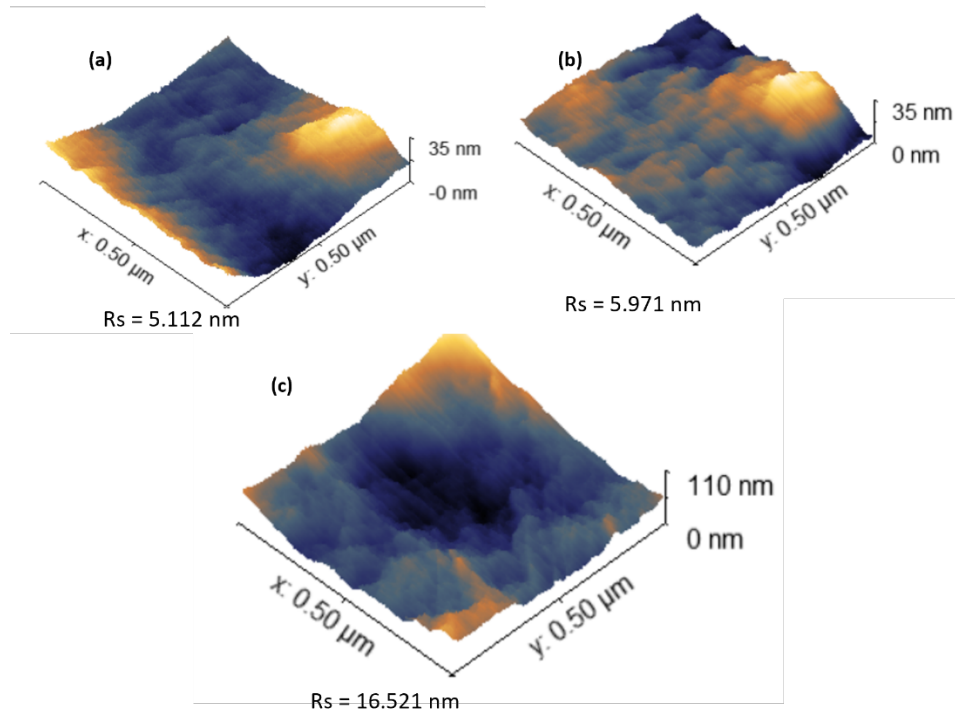


Figure 4-15 AFM results show the PDMS surface roughness (a) prior to plasma dry etch, as (b) subsequent to plasma dry etch with a masked Al metal layer, and as (c) after plasma dry etch without an Al metal layer mask.

The above results demonstrate that the RIE plasma dry etch process can effectively dismantle PDMS crosslinking and achieve high etch resolution and uniformity. The etch rate can be increased by increasing the dry etch power and pressure, but there is a limit to the etch capability of the RIE tool. To achieve sharp and clear etch profiles, high etch pressure and power are necessary. However, the shadowing effect of the metal mask and the plasma angle of the tool can affect the etch quality for features smaller than 150 μm . It suggests that the RIE plasma dry etch process with a 100 nm Al hard mask is suitable for the following RDL processes.

4.2.4 Front- and back-side interconnections on 3D FlexTrate™

Previous works on FlexTrate™ have demonstrated a reliable fabrication process for flexible FOWLIP. We successfully overcame the CTE mismatch with a 40 μm wire pitch and a 1

mm bending radius for 1000 of bending cycles. Therefore, this work utilized this technique to fabricate Cu interconnects on the front and back sides of PDMS as a test vehicle. To reduce the CTE mismatch and wire wrinkling issues of Cu on PDMS, a 2 μm Parylene C layer and a 5 μm SU8 corrugation design were first deposited on top of the PDMS as the dielectric materials of RDL.

Figure 4-16 (© 2023 IEEE) shows optical images of the fabricated test vehicle. This sample consists of four TGV dies. Each die has 8 Cu pillars interconnected by Cu wires. On the front side, two dies are connected as two groups, while on the back side, the interconnect connects two group dies and fanned out on the backside for testing. The sample shows good flexibility (< 5 mm bending radius) comparable to the conventional single side FlexTrate™ sample. Figure 4-16 (b) shows the cross-section of the TGV contacted with electroplated Cu wires. The plated Cu is about 9 μm thick. Figure 4-16 (c) is the backside contact after PDMS is opened. Figure 4-16 (d) and (e) are the top view of the front-side Cu interconnections and Figure 4-16 (f) is the top view of the back-side interconnections. Both sides have 40 μm wire pitch.

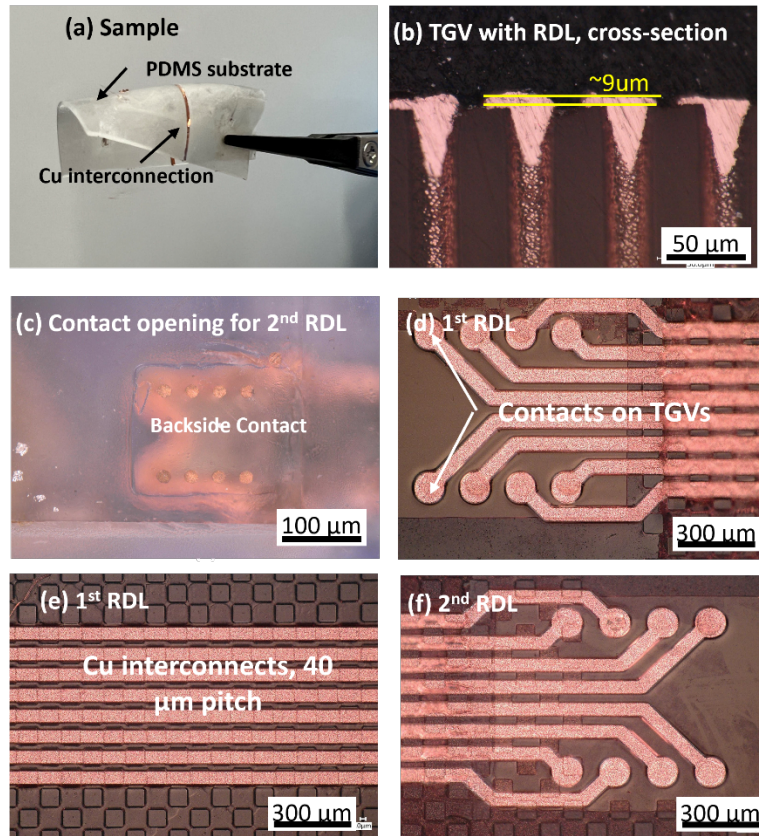


Figure 4-16 Optical images of (a) fabricated sample at a bending state. The total thickness is 300 μm . (b) Electroplated Cu interconnection connected with TGVs. (c) Backside contacts after plasma dry etching. (d) and (e) Interconnections on the TGVs contacts and with SU8 corrugation on the front interconnection. (f) Interconnections on the back side of the TGVs.

4.2.5 Reliability

To demonstrate the reliability of the front and back side RDL, four-probe measurements were conducted to measure the wire resistance on the front side RDL (named f-RDL) and backside RDL (named b-RDL) as shown in Figure 4-17 (a) (© 2023 IEEE). Mechanical reliability of the sample was measured by 2 mm bending tests for 1000 cycles. Wire resistance was compared before bending and after 100, 200, 500, and 1000 bending cycles. The results are shown in Figure 4-17 (b). The initial resistance of the Cu wire in f-RDL was 1.64 Ω , which increased to 1.68 Ω , 1.73 Ω , 1.78 Ω , and 1.74 Ω after 1000 bending cycles, representing a 6 % increase in resistance. After

connecting the two group of dies with backside RDL, the total interconnect resistance from the left pad to the right pads on the back side of the sample was 5.75Ω . During bending cycles, wire resistance increased to 5.99Ω , 6.15Ω , 6.07Ω , and 6.66Ω under 100, 200, 500, and 1000 bending cycles, respectively. The total resistance variation was 7.1 % of the whole structures.

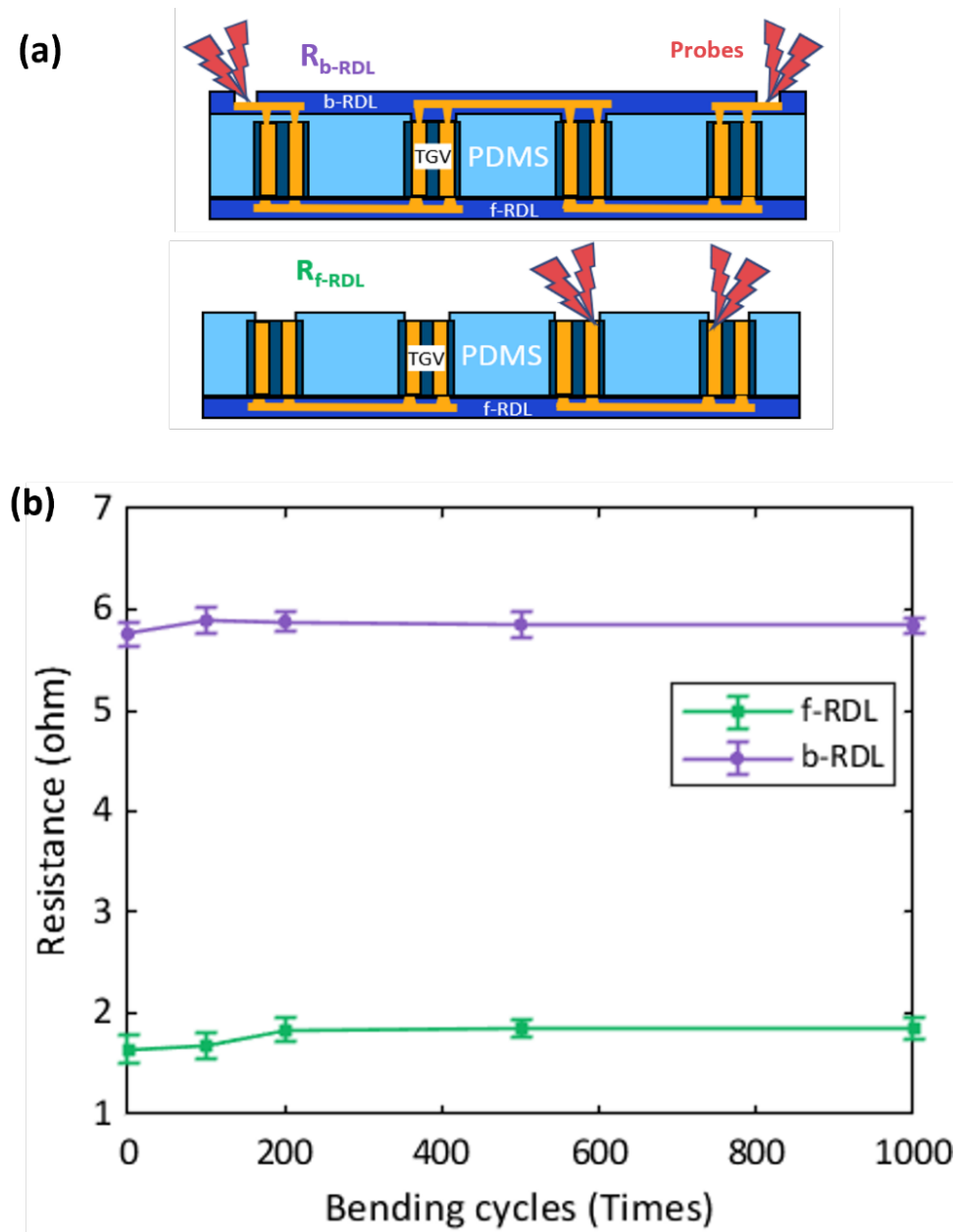


Figure 4-17 (a). Illustration of two different measurement positions front RDL (f-RDL) and back RDL (b-RDL) on the test vehicle. (b) Four-probe measurement results.

4.2.6 Inkjet printing of silver ink for integration of 3D FlexTrate™

The utilization of the Voltera NOVA tool marks a significant advancement in the field of printed electronics, particularly for the creation of interconnects on polydimethylsiloxane (PDMS) substrates. With this inkjet printing method, as shown in Figure 4-18, conductive wires made from silver ink have been successfully deposited with a precise width of 200 μm . Ensuring the functionality and durability of these conductive paths necessitates a post-printing cure and is achieved by exposing the printed silver to a temperature of 130°C for a duration of 30 minutes. The electrical performance of the resulting test vehicle is commendable, as evidenced by the total resistance measuring at a mere 0.9 Ω , indicating an effective electrical connection between the copper and the silver ink (crucial for the viability of multilayer stacking applications). Moving forward, it is an imperative to not only refine the reliability of these connections but also to extend the exploration to other inkjet printable materials, such as tin-bismuth (SnBi) ink. This optimization will likely focus on enhancing the mechanical and electrical properties of the ink-wiring interconnections, thereby expanding the potential use cases in the realm of flexible electronics.

Further work is necessary to improve the reliability of these connections and to evaluate additional inkjet materials such as SnBi ink. This would involve optimizing the physical and electrical integrity of the ink-wiring interfaces to ensure their performance in various applications.

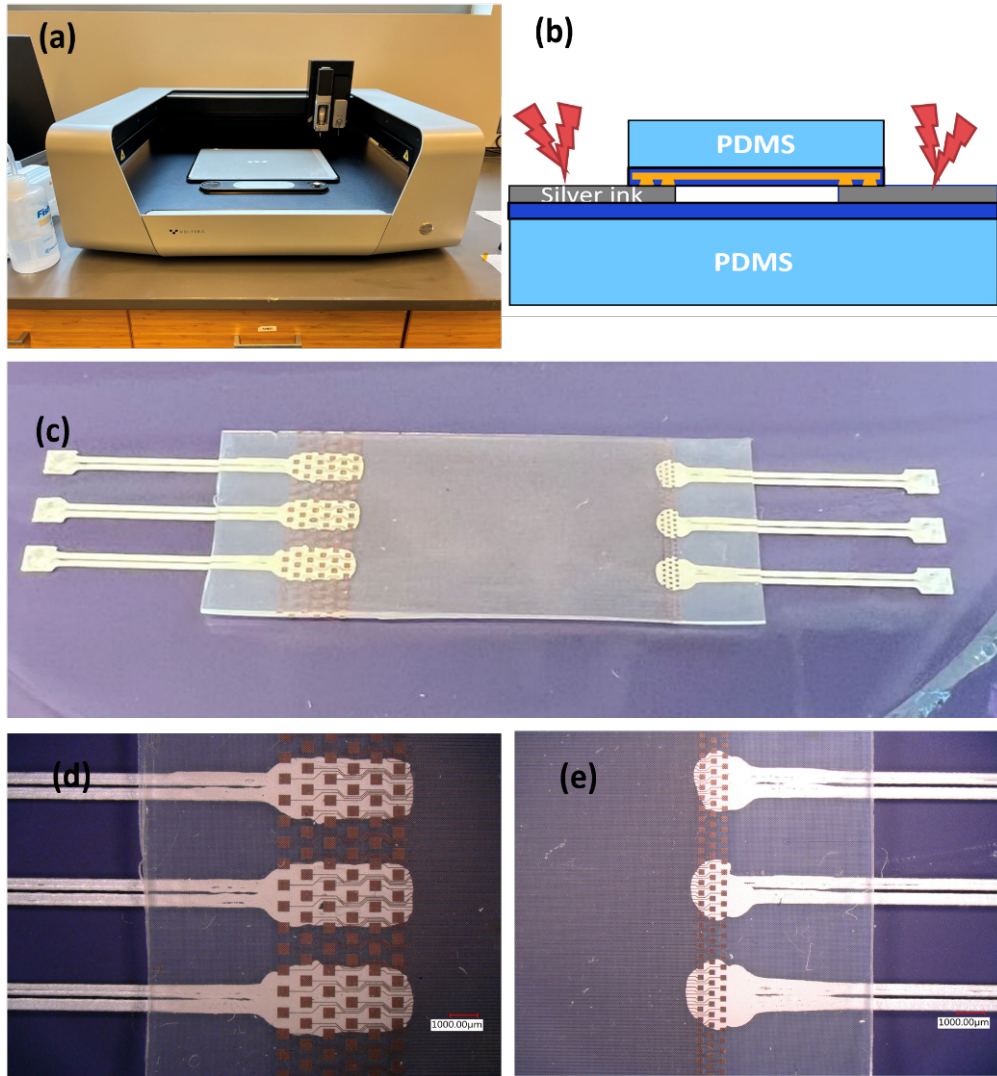


Figure 4-18 (a) Voltera inkjet printer for dispensing silver interconnect ink. (b) Schematic view of the test vehicle. (c), (d) and (e) the optical images of test samples.

4.2.7 Comparison of 3D FOWLP method with existing technologies

Within the scope of multi-layer integration technologies, a comprehensive assessment highlights the distinctions across various methodologies as shown in Table 4-1. The traditional approach of multilayer printing, which employs inkjet printing, is characterized by a homogeneous integration process. Silver conductive ink is utilized, presenting an electrical conductivity in the range of 1 to 10×10^6 S/m and a thermal conductivity spanning 5 to 200 W/m·K. Vias typically

have a pitch of approximately 100 micrometers and demonstrate considerable flexibility: evidenced by the structure's capacity to fold. Despite its cost-effectiveness, a notable limitation is the potential for stress accumulation during fabrication, that can compromise the structural integrity.

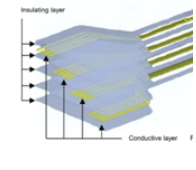
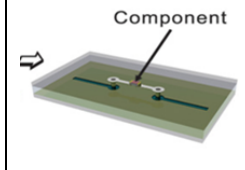
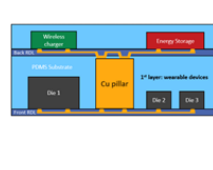
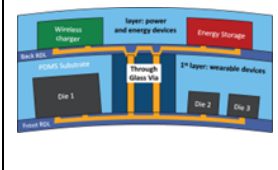
In contrast, the liquid metal via method, which employs laser drilling for via formation, leads to a heterogeneous structure. The material in use, eutectic gallium-indium (E-GaIn), provides an electrical conductivity of 3.4×10^6 S/m and thermal conductivity of 20 W/m·K. In addition to having similar via pitch to multilayer printing, this approach also offers enhanced flexibility, allowing bends of less than 1 millimeter. However, the higher material cost and concerns over the low aspect ratio, along with safety and reliability issues, present significant drawbacks.

The metal pillar technique, utilizing a pick-and-place fabrication process, also achieves heterogeneous integration with copper vias exhibiting an electrical conductivity of 59×10^6 S/m and a thermal conductivity of 401 W/m·K. The via pitch is substantially larger, exceeding 500 micrometers, yet the structure maintains flexibility comparable to that of liquid metal vias. This method's low cost is advantageous, but it is hindered by alignment accuracy issues, which are critical in precise electronic assembly.

The innovative approach presented in this work leverages through-glass vias with a pick-and-place fabrication process. Copper is employed for its high electrical and thermal conductivities, mirroring those of the metal pillar method. The technology distinguishes itself with a reduced via pitch of less than 100 μm , suggesting superior integration density. Meanwhile, the overall flexibility of devices integrated in this manner is preserved and can accommodate bends of less than 1 mm. Positioned between the lower costs of multilayer printing and metal pillars and the higher costs of liquid metal vias, this method's expense is moderate. A hallmark of this technique

is the exceptional RF performance it yields, likely attributed to the refined pitch and high-grade copper utilized, positioning it as a promising avenue for future multi-layer integration applications.

Table 4-1 Comparison of different multilayer integration methods

Methods	Multilayer printing [79]	Liquid metal via [80]	Metal pillar [76]	This work
Structure				
Fabrication process	Inkjet printing	laser drilling	Pick&place	Pick&place
Integration	Monolithic, homogeneous	Heterogeneous	Heterogeneous	Heterogeneous
Via materials	Conductive ink (Silver)	E-GaIn	Cu	Cu
Conductivity (106 S/m)	10.1	3.4	59	59
Thermal conductivity (W/m·K)	5-200	20	401	401
Via pitch (μm)	~ 100	> 100	> 500	< 100
Flexibility (mm)	Foldable	< 1 mm	< 1 mm	< 1 mm

Cost	Low	High	Low	Medium
Remark	Stress accumulation during fabrication	Low aspect ratio, safety, reliability	Alignment accuracy	Excellent RF performance

CHAPTER 5 Conclusions and outlook

5.1 Conclusions

This dissertation offers a thorough investigation into flexible powering solutions for wearable electronics, focusing on a flexible battlet battery, a flexible wireless charger, and the 2D/3D integration of these components with other electronics using FlexTrate™ technology.

Chapter 1 discusses the current developments in wearable technologies and the need for flexible, safe, and high-performance energy storage and integration solutions.

Chapter 2 proposes and develops battlet electrode structure, featuring a low Young's Modulus composite current collector to minimize bending stress and enhance the battery's flexibility. Two types of battlet batteries are explored, detailing their fabrication processes and performance. Utilizing LFP cathode and graphite anode materials along with LiFSI/PYR14FSI ionic liquid electrolyte, a total capacity density of 0.7 mAh/cm² was achieved, also addressing flammability concerns. The battlet battery displayed superior performance compared to conventional planar electrodes after undergoing a 5 mm bending radius test 1,000 times, excelling in both C-rate tests and cycle tests. The battery also features a thickness of less than 300 μm and flexible packaging, with package reliability assessed through a 50-hour aging test.

Chapter 3 introduces a flexible wireless charger developed using FlexTrate™ technology and a resonant magnetic coupling method based on previous work. This charger delivers a consistent 3.3 V output for battery charging, demonstrating a maximum coupling distance of 2 mm and bendability up to 15 mm, while maintaining functional electrical performance at a frequency of 13.56 MHz and 5 V V_{pp}. The maximum output power reached approximately 3.9 mW when charging a Li-ion battery.

Chapter 4 discusses the 2D and 3D integration methods on FlexTrate™. In 2D integration, the flexible battery and wireless charger were integrated with a 33 UV μ LED parallel array and a dome switch. The total array requires a 2.9 V forward voltage and consumes 3 mW of power at a 3.1 V supply, and the integrated battery can sustain the μ LED array for at least 1.5 hours. In 3D Fan-Out Wafer Level Packaging (FOWLP) integration, Through-Glass Vias (TGVs) are employed as interconnections from the front-interconnects to the back-interconnect. This 3D architecture significantly reduces packaging size while enhancing the robustness and safety of wearable devices compared to traditional planar devices. Notable technological developments in this chapter include a dry etching process for PDMS with an etching rate of 0.49 $\mu\text{m}/\text{min}$ and a minimum etching feature of 150 μm , under an Al hard mask without affecting the surface roughness. Reliable front and back interconnects with a 40 μm wire pitch were also successfully fabricated on a PDMS substrate. The resistance of the Cu interconnects was measured at 5.75 Ω , with only a 7% increase after a 1,000-time two-millimeter radius bending test, underscoring the effectiveness and reliability of the flexible 3D FOWLP approach using TGVs for hybrid flexible electronics.

5.2 Outlook and future work

Current work demonstrates that the battlet approach effectively enhances the flexibility of the battery. Looking ahead, several considerations are crucial for improving the performance of the battlet battery, wireless charger, and the integration.

5.2.1 Inkjet printing approach for battlet fabrication

As discussed in Chapter 2, the screen-printing approach results in a concave shape of the battlet electrode due to the surface tension of the slurry and the stencil's properties. Consequently, both cathode and anode exhibit thickness variations within each battlet. This difference in thickness can increase electrode polarization during cycling and cause nonuniform lithiation in the

electrode materials during operation, thus reducing the battery's cycling life. To address these challenges, we explored the inkjet printing method to improve electrode uniformity as illustrated in Figure 5-1.

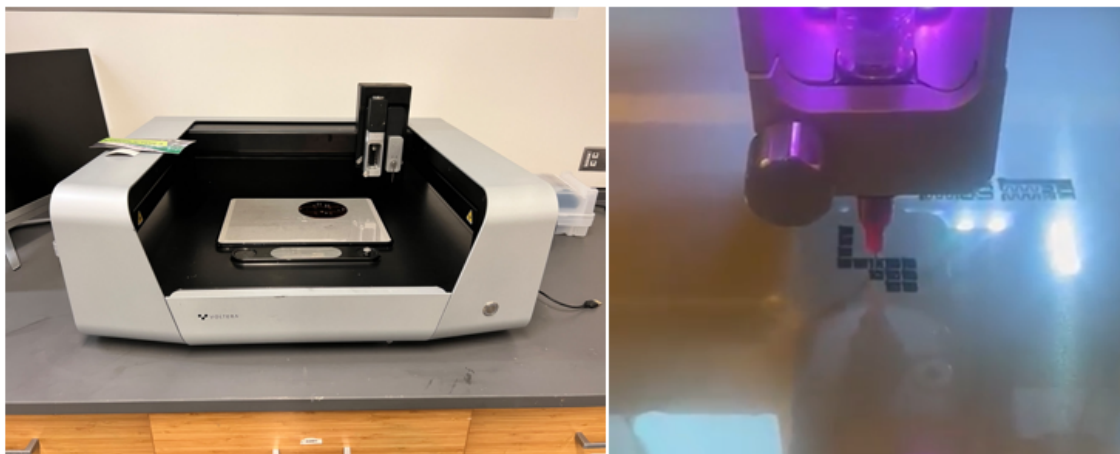


Figure 5-1 Inkjet printer and inkjet printed battlet electrodes

Figure 5-2 compares the profile of inkjet-printed battlet electrodes to those produced by screen printing (refer to Chapter 2 Figure 2-20) showing a reduction in surface roughness from $10.15\ \mu\text{m}$ to $3.56\ \mu\text{m}$. Additionally, weight loading variation decreased from 15.6% to 4.5%. These results suggest that the inkjet approach offers better slurry distribution than screen printing, although further optimization, including adjustments to slurry viscosity for inkjet printers and throughput improvements, is needed. Initial results indicate an improvement from a concave to a more uniform, slightly convex battlet profile as shown in Figure 5-4.

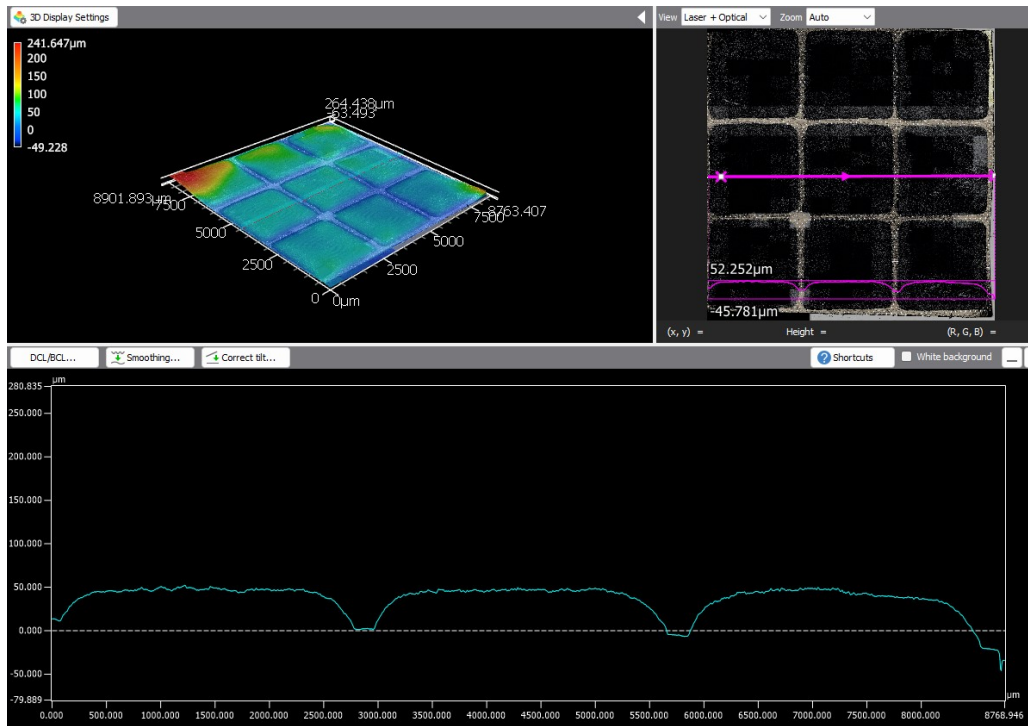


Figure 5-2 Confocal microscope results of the surface profile of the inkjet - printing cathode electrodes.

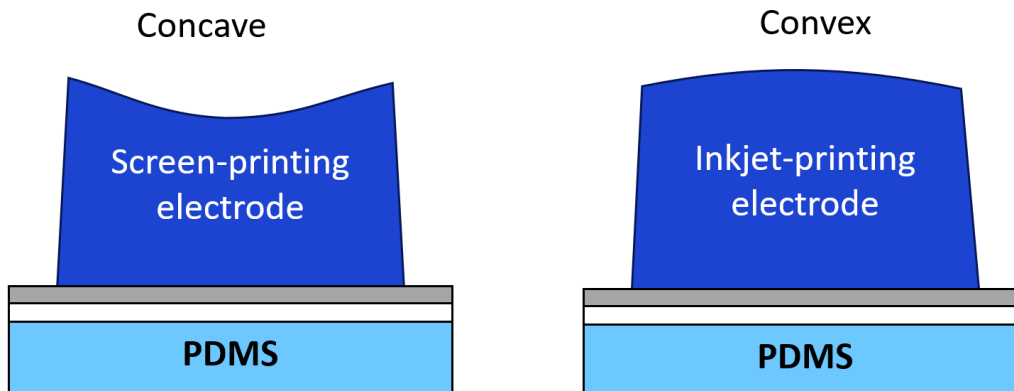


Figure 5-3 Comparison of the profile of screen-printing electrodes and inkjet-printing electrodes.

5.2.2 Co-plane cathode and anode battlet battery

In addition to optimizing battlet uniformity, rethinking the battery structure is another critical aspect of future work. The current battlet approach considers only the mechanical interaction at the electrode-current collector interface. However, interactions within the battery components are more complex, involving friction and potential delamination between electrode layers and separators [30]. This suggests a reevaluation of the traditional sandwich structure (cathode/separator/anode). A potential solution involves coating both cathode and anode battlets on the same side of a flexible substrate with a lithographically patterned current collector, as illustrated in Figure 5-4. This co-plane structure allows the elimination of the separator from the traditional battery configuration. In addition, during mechanical flexing, the friction of the layers are reduced. However, the concern of the structure is the impedance of the battery. The impedance can increase as the Li-ion must travel greater distances from tens μm (thickness of the separator) to hundreds of μm (spacing between electrodes) during cycling, which could affect battery performance.

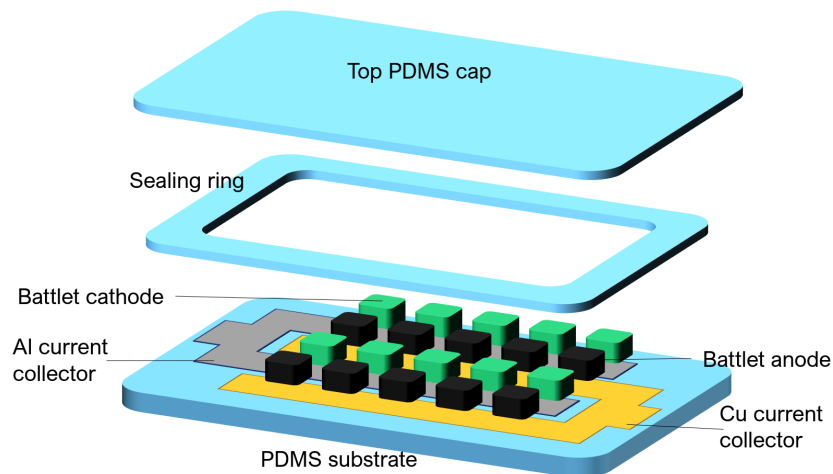


Figure 5-4 Co-plane cathode and anode battlet battery.

5.2.3 Power management on wireless charger

Current wireless charger modules only provide a constant voltage for charging. Future enhancements should focus on improving power management to allow more accurate charging and monitoring, which could extend battery life and enhance monitoring of the battery's health condition. Integration of features such as over-heating detection, short-circuit cut-off, and programmable current/voltage control should be considered.

5.2.4 Integration of the FlexPower with light sensor controller

The current integration approach utilizes a dome switch to control the circuit, which compromises device reliability. Future work proposes a no-contact method using an ambient light sensor coupled with a transistor to control the on/off states of the microLED array, as depicted in Figure 5-5. The sensor's output current, proportional to the ambient light intensity, activates the bipolar transistor to illuminate the LED array when the light exceeds a pre-set threshold, adjustable via a voltage divider resistor.

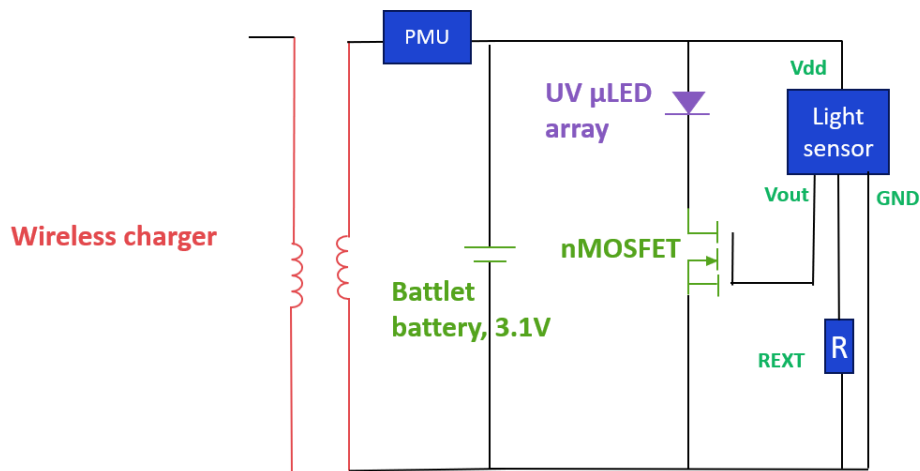


Figure 5-5 No-contact light-control switch integrated with battlet battery and LED array

Appendix A Investigation of Die Shift in FlexTrate™ Process

A.1 Introduction to Fan-Out Wafer-Level Package (FOWLP)

In the field of electronic packaging, wafer-level packages are mainly divided into fan-in and fan-out techniques as shown in Figure A-1. The traditional wafer-level package adopts the fan-in wafer-level package (FI-WLP) in which the area of the interposer is as same as die and pins are distributed in the die area. This technology is applied to dies with a small number of pins [81]. However, with the increase in the number of signal output pins and performance of dies, the traditional technology cannot cope with the requirements and thus the FOWLP was invented [82]. These technologies enables high performance computing and wearable sensing with high electrical performance and small form factor [83], [84], [85].

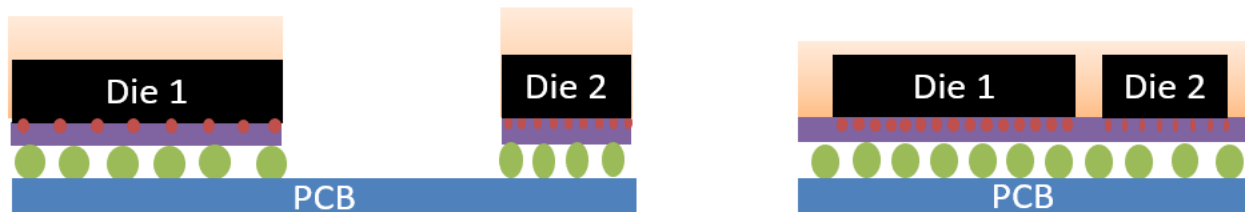


Figure A-1. Structure of FI-WLP (Left) and FO-WLP (Right).

Standard FOWLP technology involves dicing and separating the dies, then embedding dies inside an epoxy substrate as shown in Figure A-2. The procedure is to first secure the dies firmly on one handler, the die pitch meets the pitch specification of the circuit design, then casting to form an epoxy substrate embedded with dies. Later, the substrate is separated from the handler. In FOWLP, dies are precisely re-placed on a carrier. Then the carrier is reconstituted by molding

compound. Therefore, the epoxy compound with re-positioned dies is also called reconstituted wafer. It can be used in many standard wafer processes to form the required circuit.

FOWLP has three advantages. First, FOWLP can achieve a higher pin count. Epoxy covered on the die extends beyond the area of the die, thus the pins are not limited to the die area compared with FIWLP. Through Re-distribution Layer (RDL), the pins can be designed on the epoxy which is larger than the die area. Second, passive devices such as capacitors, inductors, and resistors can be placed over epoxy for lower loss. Third, FOWLP has a small form factor that increases its scalability for higher performance and better power consumption.

Taking advantage of FOWLP, FlexTrate™, a flexible electronic packaging technology based on fan-out packaging was developed.

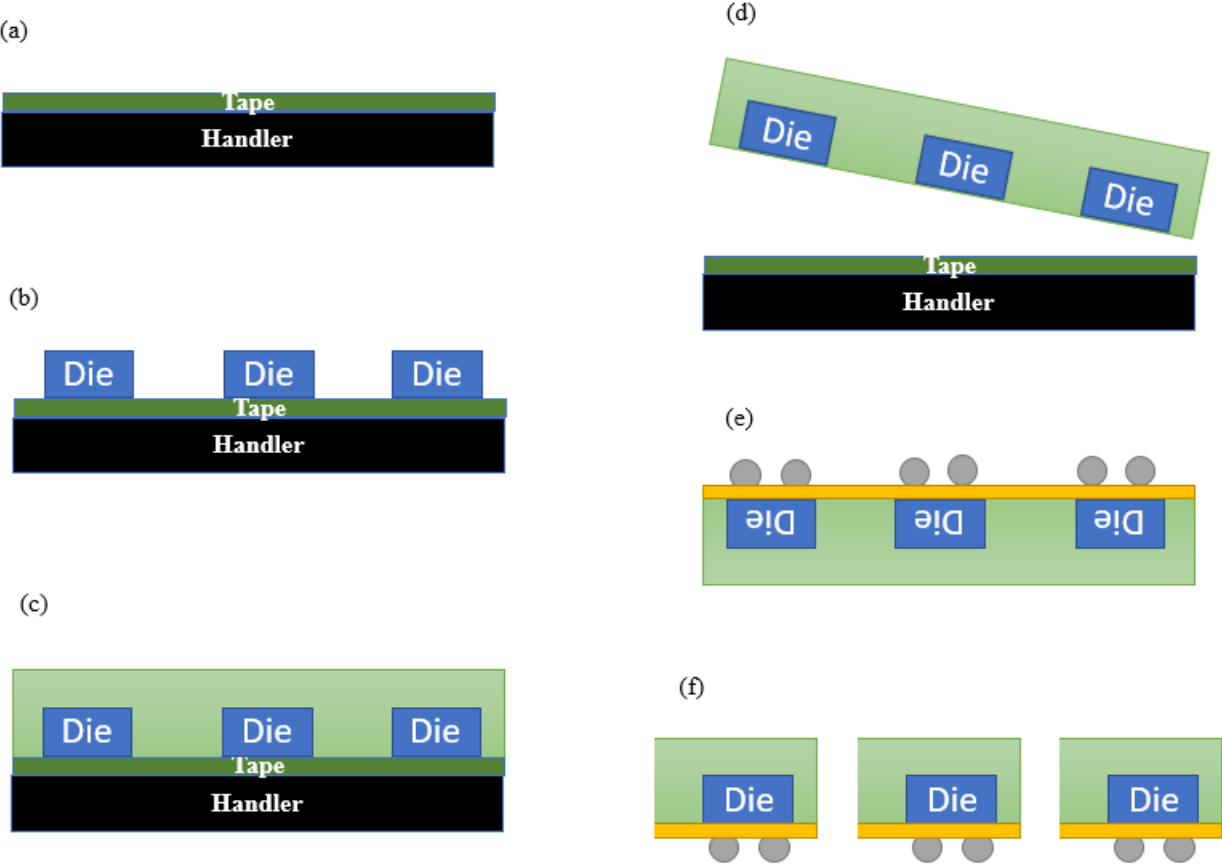


Figure A-2. FOWLP process flow: (a). Align Tape on Handler; (b). Die placement; (c). Wafer level Molding; (d). Release from handler; (e). RDL and Bumping processing; (f). Singulation

A.2 PDMS and its cure kinetic behavior

A.2.1 PDMS properties

PDMS (Polydimethylsiloxane), also known as dimethylpolysiloxane or dimethicone, is a thermoset organic material, which has high flexibility, biocompatibility, and transparency. Due to these unique properties, it has been widely used in MEMS, lab-on-a-chip, and flexible electronics as a substrate or carrier. Comparing with the epoxy molding compound (EMC) adopted in FOWLP, PDMS has a significantly low glass transition temperature [87]. Typically, the glass transition temperature of epoxy compounds is in the range of 120 to 180 °C, while PDMS is about -120 °C [88]. Therefore, to mold EMC, it requires heating above its glass transition temperature, and then cooled down to room temperature. For PDMS, it can be cured at room temperature. Lowering cure temperature avoids lots of problems such as thermal shrinkage, void formation, and wafer warpage. In addition, EMC is in the glassy state after cure and has high Young's modulus (~22 GPa), while PDMS is in rubbery state which is flexible and stretchable (Young's Modulus 0.5 MPa). Taking the advantages of PDMS, FlexTrate™ replaces epoxy molding compound materials with PDMS as substrate material.

PDMS in liquid state is a viscous liquid called "Dimethicone", which belongs to silicone oil. It is a mixture of organic siloxanes with different polymerization degree, the end and side groups are all hydrocarbon (such as methyl, ethyl, phenyl, etc.). In general, it is a colorless, odorless, non-toxic, non-volatile liquid. PDMS in solid state is hydrophobic, inert, and a non-flammable elastomer.

A.2.2 PDMS cure reaction

The process that transforms PDMS from liquid to solid is called cure or polymerization. For the cure process of PDMS, typically the liquid dimethicone base and cure agent are usually mixed by the mixer in a certain ratio (1:1 ~ 20:1), and the air bubbles in the mixture float to the surface and burst by means of vacuum. Then the mixture is put in a heat oven at different temperatures (25°C ~ 170°C) for a certain time (10 mins ~ 24 hours) which depends on the oven temperature.

During the curing process, the monomers of PDMS crosslink with each other [89] [90]. The proportion of the crosslinked molecules in the total monomers is called the degree of cure which is in a range of 0 ~ 1.

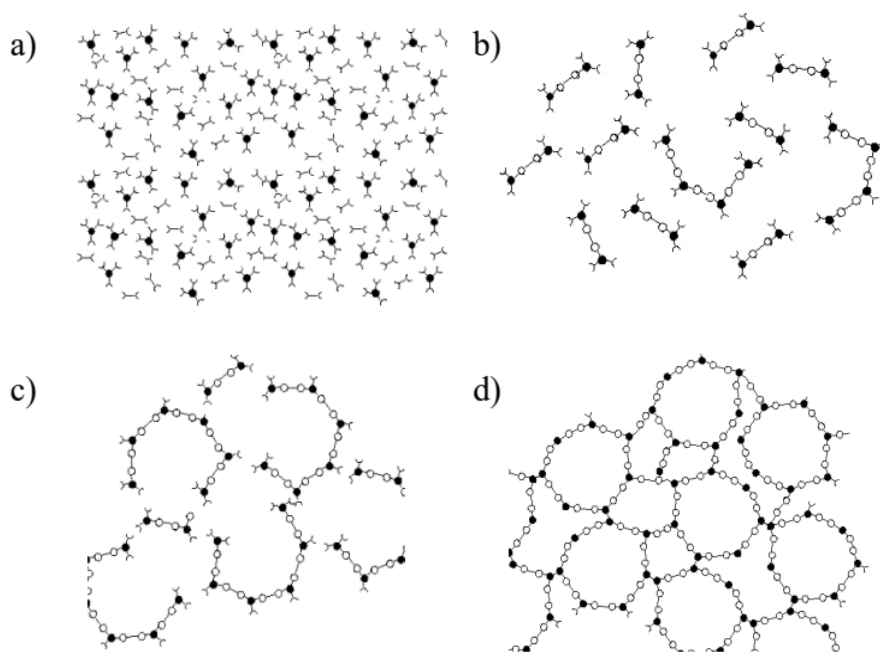


Figure A-3. Cure process of PDMS. (a). Monomer; (b). Monomer starts reaction; (c). Network formation; (d). Fully cured.

Network formation is a bond-to-bond additive reaction. When two monomers form a larger molecule, two bonds in each monomer combine into one bond, and heat will be released during this process because it lowers the total bond energy. Ideally, assuming each bond to bond formation

will release the same amount of heat, the degree of cure can be estimated by using the portion of released heat Q in total heat Q_T the process will release, namely [11]:

$$\alpha = \frac{Q}{Q_T}$$

α is the degree of cure, Q is released heat during the curing process, and Q_T is the Total released heat until PDMS is fully cured. Therefore, the cure rate is in the form:

$$\frac{d\alpha}{dt} = \frac{\dot{Q}}{Q_T}$$

\dot{Q} is the instantaneous heat release rate, and t is the time. This parameter can be measured via Differential Scanning Calorimetry experiment. In addition, the cure rate can also be expressed in the form:

$$\frac{d\alpha}{dt} = \frac{dT}{dt} \frac{d\alpha}{dT} = k_0 e^{\frac{-Ea}{RT}} f(\alpha)$$

$$f(\alpha) = \alpha^m (1 - \alpha)^n$$

$$m + n = 2$$

k_0 is a pre-exponential factor, Ea is the activation energy of cure following the Arrhenius equation. T is the temperature in Kelvin and R is the ideal gas constant. $f(\alpha)$ is in the form of second-order autocatalytic model, and $m + n = 2$ for second-order reaction [91].

The autocatalytic model is adopted for describing this thermosetting cure reaction [92]. In chemistry, autocatalytic reaction refers to a kind of reaction in which the product of the reaction is a reactant for the next stage reaction. Generally, most epoxy cure processes widely follow the autocatalytic model. For PDMS, the base part is divinyl terminated polydimethylsiloxane that contains two carbon-carbon double bonds at the end of the chain. They can combine with silicon hydride through additional reaction under the catalysis of the platinum complex. This process is also known as the hydrosilylation reaction [93].

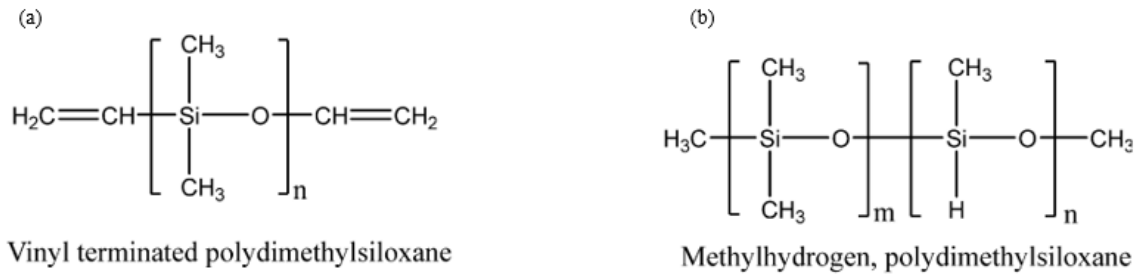
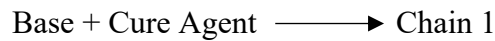


Figure A-4. Two parts of PDMS. (a). Base structure; (b). Cure Agent structure.[11]

Therefore, the crosslink reaction of PDMS can be described as follow:



Thus, PDMS cure process follows the second-order autocatalytic model.

A.3 Die shift problem

The die position difference before the molding process and after release from the carrier wafer (first handler in FlexTrate™) is called die shift. As stated in the previous section, due to the unique process of the FOWLP, die shift is one of the critical problems to be addressed. When compression molding the compound and after release from anchors, it is necessary that the position of the die does not shift, because the RDL which are defined using lithography, will experience misalignment due to the shifted die position.

A.3.1 Die shift analysis on FOWLP

There are two main reasons for the die shift problem. One is fluid flow (FF) factor, another is thermal mechanical (TM) factor [94]. For FF, the epoxy, which is the packaging dielectric material on top of dies, will flow out from the center to the edge of the wafer during casting. In this process, epoxy materials exert tensile and shear stresses on the sides of dies. Because of the asymmetric stress, dies detach from tape and shift from center to edge. For TM, curing epoxy

process and release process need a high temperature, during this time frame the thermal expansion of epoxy and the handler cause die shift. Epoxy cure shrinkage and thermal shrinkage are TM reasons as well. FF and Thermal Expansion make dies to shift outward of the wafer while cure shrinkage and thermal shrinkage make dies to shift inward. Since dies shift towards the edge in FOWLP, most researchers have considered FF and thermal expansion as the main reasons for die shift analysis.

Chee et al. stated that die shift is caused by shear stress on dies when epoxy flows out from the center to the mold edge [95]. They studied the relationship between die shift and die thickness, mold compression velocity, die pitch distance, and die placement pattern. Results show that the die shift is inversely proportional to the die thickness for wafer-level molding. Reducing die pitch distance and compression molding velocity will also help to reduce die shift while die placement pattern does not. Lin et al. found the die shift at the edge of the wafer is nonlinear, while the CTE effect exhibits a linear trend [96]. They stated that the joint effect of CTE and mold flow should be considered. They also proposed some other strategies, for example lowering the initial diameter of the molding compound, increasing the thickness of the molding compound, and reducing the flow speed, to optimize die shift. Sharma et al. developed a methodology to measure die shift and create die shift map on an 8-inch wafer [97]. By using pre-die-shift method, they reduced the maximum die shift from 633 μm to 79 μm . Yang et al. established a 1 D viscous flow model to analyze the relationship between compression velocity and stress distribution [98]. Han et al. established a model to systematically study the effect of each step. They concluded that the TM effect and FF effect account for 70% and 30% of die shift in FOWLP. Similarly, Cheng et al. also established a multi-physical finite element model to analyze the factors that affect die shift [99].

A.3.2 Die shift analysis on FlexTrate™

In FlexTrate™, though a similar process is adopted, the model is different. First, in FOWLP, there is no support layer after epoxy release from thermal release tape, while in FlexTrate™, the RDL is constructed with a holding handler still anchored to the PDMS as it is in the rubbery state. Second, the viscosity of PDMS is lower than Epoxy. In the flowing step, the viscosity of EMC is about 400 Pa ·s, while PDMS is about 60 Pa ·s [100]. Therefore, combining with 24 hours slow curing process, the stress can be ignored due to viscoelastic relaxation. Finally, the cure temperature of PDMS is 30 °C, which is far below the temperature of EMC curing. The glass transition temperature of PDMS is -120 °C, while the glass transition temperature of epoxy is 120-160 °C. This low cure temperature significantly relieves the thermal expansion of polymer, thus reducing the outward die shift.

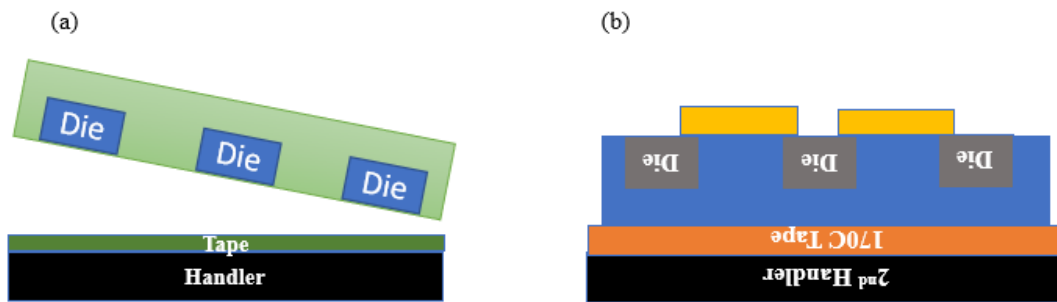


Figure A-5. RDL layer construction. (a). FOWLP, epoxy is free without support handler; (b). FlexTrate™, PDMS is held by a wafer handler.

Considering the above reasons, die shift in FlexTrate™ is not to the edge of the wafer but to the center. When the stress of PDMS flow on dies is lower than the adhesion strength (3.7 N/mm) of the tape, which is used to fix dies, dies do not move during compression molding. However, during the crosslinking reaction, properties of PDMS change, along with changes in density. Thus, when the anchors are released, the PDMS starts to shrink, this causes dies to move along with

direction of PDMS shrinkage. PDMS shrinkage has been discussed and considered in microfluidic area, but it still lacks discussion in flexible packaging process. Therefore, it is necessary to conduct both experimental and theoretical study on the effect of PDMS shrinkage on die shift.

A.4 Experimental setup and methodology

A.4.1 Flow diagram of the work

Figure A-6 shows the flow diagram of this work. In the beginning, two routes are adopted for getting simulation parameters. The left route is the DSC experiment for finding the thermal kinetic behavior of PDMS. This kinetic equation is used in ANSYS Transient Thermal Project to simulate the degree of cure of PDMS in FlexTrate™ process. The right route is experiment for getting the physical shrinkage of PDMS. PDMS samples with alignment marks are fabricated by using FlexTrate™ process. After release of the handlers, PDMS shrinkage ratio is measured by Nanotronics nSpec tool and is fed to ANSYS Static Structural Project. Subsequently, the Transient thermal and Static Structural model are coupled in ANSYS to simulate PDMS Shrinkage and Die Shift. Both the models are equipped with ANSYS Composite Cure Simulation. Finally, the simulation results of die shift will be discussed and one of the applications of this theoretical model is demonstrated through FlexTrate™ sEMG system.

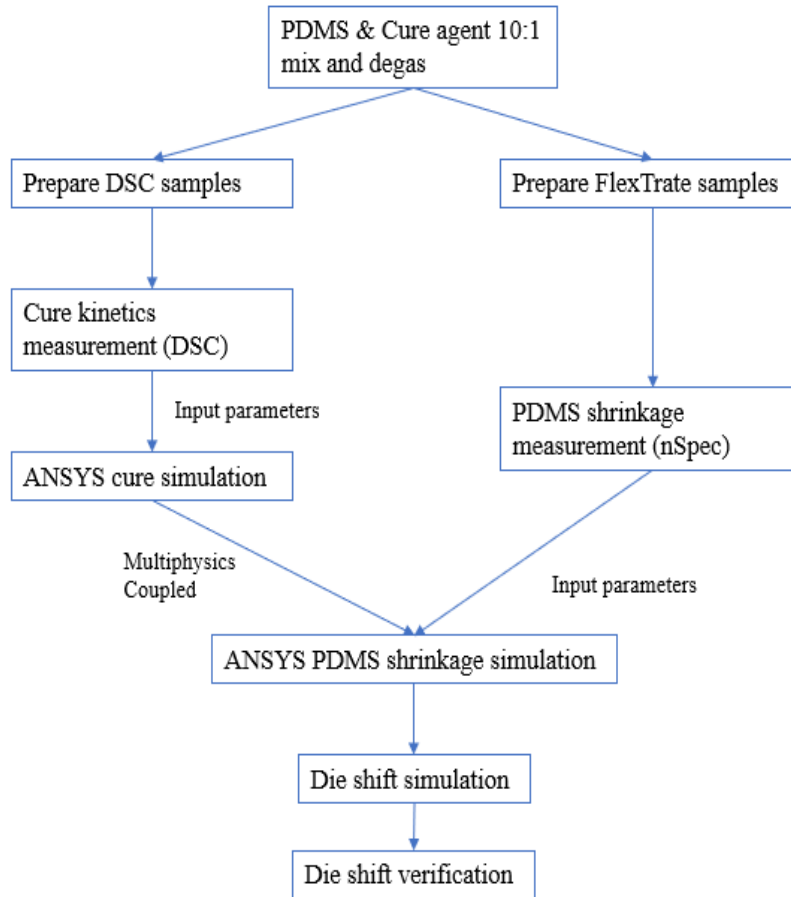


Figure A-6. The flow diagram of this work.

A.4.2 Differential scanning calorimetry test of PDMS cure kinetics

Differential scanning calorimetry (DSC) is a thermal analysis method in material science. The basic principle of DSC is that heat is absorbed and released as the sample undergoes phase changes, glass transition, and chemical reactions. The compensator can then measure how much heat flow is to be increased or decreased to keep the sample and reference temperatures consistent. It can measure various thermodynamic and kinetic parameters of materials such as specific heat capacity, reaction heat, transition heat, phase diagram, reaction rate, crystallization rate, polymer crystallinity, and sample purity. The curve recorded by the differential scanning calorimeter is called the DSC curve. DSC experiment can be conducted over a wide temperature range (-

175~725°C). It has high resolution, requires small sample size, and is suitable for both inorganic materials and organic compounds.



Figure A-7. Perkin Elmer DSC 8000

In this work, we use Perkin Elmer DSC 8000 (Figure A-7), which is provided by UCLA Chemistry and Biochemistry Department, Molecular Instrumentation Center, to measure PDMS cure Kinetics. The selected parameters of DSC 8000 tool are listed in Table 5-1.

Table 5-1 Selected specs of DSC 8000

DSC Type	Calorimetric Performance				Temperature	
	Dynamic Range	Precision	Range	Accuracy	Heating Rate	Cooling Rate
Double-furnace design	±1300 mW	< ±0.003%	-180 to 750 °C	±0.05 °C	0.01 to 300 °C/min	0.01 to 150 °C/min

- 1) The DSC Experiment of PDMS cure kinetics test follows the steps below: PDMS SILASTICTM MDX4-4210 is prepared by mixing PDMS and cure agent in weight ratio 10:1, spinning in mixer at 2200 RMP for 2mins and degas for 2 mins.
- 2) Load samples and prepare. Place the sample flat in a small Aluminum pan with disposable sticks (preferably no more than 1/3 of a volume of Al pan, about 10 mg).
- 3) Weigh sample: record the weight of crucible 1 + sample (experimental group), and the weight of crucible 2 (reference group).

- 4) Place the samples. Right: control group (no sample); Left: experimental group (with sample).
- 5) Open the software. Set a heating curve and wait for the sample temperature to stabilize and start heating.
- 6) Analyze the curves and save them when the heating is over.
- 7) Remove the sample. Open the furnace lid when the sample temperature drops above room temperature and take out the sample crucible, the reference crucible may continue to be used.
- 8) When the instrument is not in use, the normal order of shutdown is: shut down the software, exit the operating system, shut down the computer host, and monitor. Usually, to maintain the device in a good condition, leaving the device in an idling state and keeping a small amount of nitrogen gas flowing is a good way if it will be used shortly.

A.4.3 PDMS shrinkage and die shift measurement method

The process for PDMS shrinkage measurement is almost as same as the general FlexTrate™ process. Here, gold alignment marks are used to indicate the PDMS shrinkage in the whole 4-inch wafer in Figure A-8. Figure A-9 is the schematic view of the pattern design. This pattern is transferred to PDMS and then the pitch between the pattern is measured to show the PDMS shrinkage.

For the die shift measurement, we first transfer alignment marks to the first handler, and then use the pick and place tool to place the dies by aligning with these marks. Then PDMS is dispensed on top of it and the rest of the FlexTrate™ process is carried out.

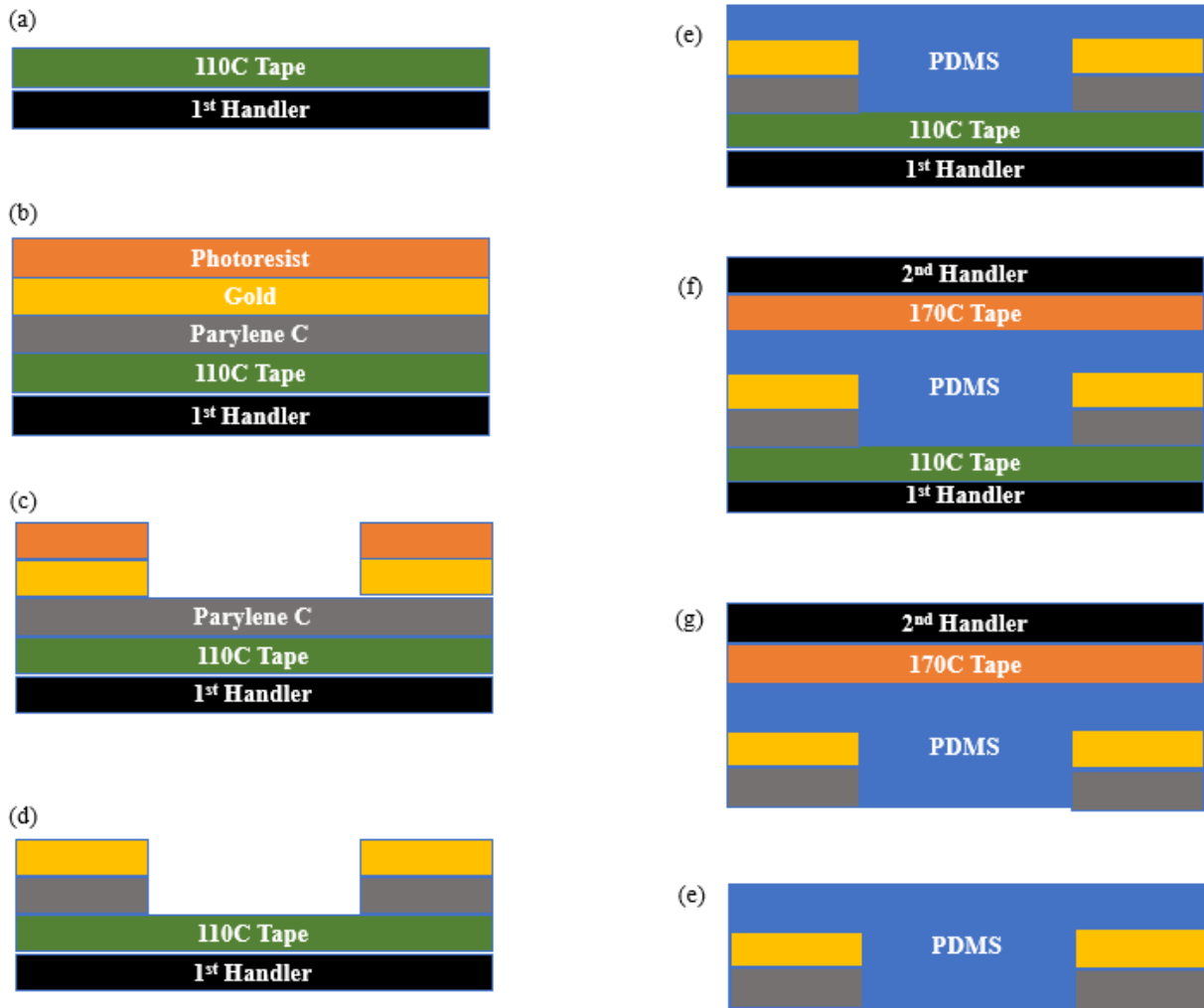


Figure A-8. FlexTrate™ process for PDMS shrinkage measurement: (a). Align thermal release tape on Si wafer; (b). Deposit Parylene C (1 μm), gold (50 nm) and photoresist SU8 (0.5 μm); (c). Lithograph SU8 and dry etch gold to create pattern; (d). Dispense PDMS; Cover Second handler and Cure; (e). Release 1st handler and measure pattern interval change; (f). Release 2nd handler and measure pattern interval change.



Figure A-9. Mark matrix layout after release 1st handler. The blue background is PDMS and yellow crosses are gold marks.

To measure the PDMS shrinkage and the die shift, Nanotronics Co. nSpec tool is used in this work. This tool contains three parts: optical camera, moveable stage, and software analyzer. By inputting the designed interval distance between the dies or alignment marks, software generates a matrix layout of die matrix or mark matrix. Then, the stage carries the PDMS sample and goes through the matrix layout map. Meanwhile, the optical lens takes pictures of each die or pattern. Finally, the analyzer which is integrated with Artificial Intelligence algorithm compares these images with a model image to analyze surface defects, die shift, or shift of alignment marks. Therefore, in this work, PDMS shrinkage and die shift are measured by comparing the mark position difference between the “perfect” picture and the captured pictures.



Figure A-10. Lab Owned Nanotronics Co. nSpec Tool.

Table 5-2 Specs of Nanotronics Co. nSpec tool.

System		Optics		Stage		
Dimensions	Power Supply	Light Source	Objectives	Travel	Flatness	Repeatability
153*133*176 cm	110/220V, 3.5 amps	White Light LED	2.5, 5, 10, 20X	200 mm X&Y direction	30 μm	$\pm 0.5 \mu\text{m}$

A.4.4 Finite Element Simulation of PDMS Shrinkage and Die Shift

ANSYS is a large scale general finite element analysis (FEA) software that integrates structural, thermal, fluid, electric, magnetic, and acoustic field analysis. It has a wide range of applications in semiconductors, electronics, chemical, biomedical, and other fields.

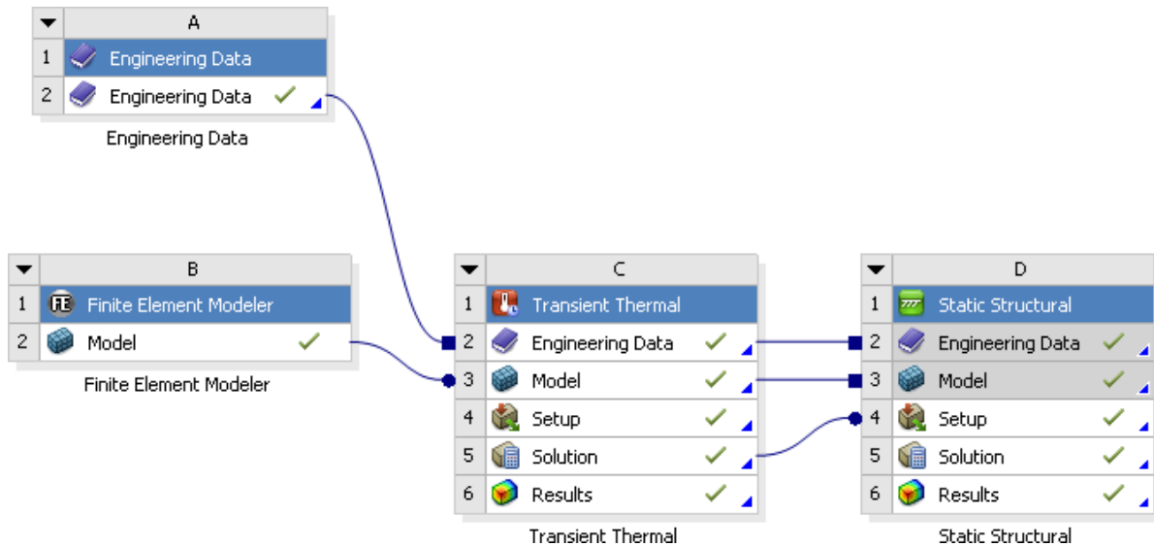


Figure A-11. Workflow of PDMS cure, PDMS shrinkage, and die shift simulation in ANSYS Workbench.

ANSYS Workbench Transient Thermal and Static Structural projects (Version 20R1) equipped with ANSYS Composite Cure Simulation Extension (ACCS, Version 1.7) are used in this work to simulate cure kinetics of PDMS, PDMS shrinkage, and die shift caused by PDMS shrinkage.

The ACCS extension is fully embedded into the ANSYS Workbench environment. The PDMS and silicon die properties are stored in the “Engineering Data” module. The structure of FlexTrate™ design is stored in the “Geometry” module. These are then fed into a “Transient Thermal” module equipped with ACCS extension where the temperature distribution will be computed based on the properties of degree of cure, the state of the material, and the instantaneous heat of reaction during the cure. Subsequently, thermal and cure data are fed into the “Static Structural” module where the ACCS cure material model calculates the development of stresses and distortion of PDMS and dies. The shrinkage of PDMS scales linearly with the degree of cure, so the die shift caused by PDMS shrinkage also relies on the degree of cure of PDMS.

The structure of simulation geometry is shown in Figure A-12. This is a 90mm diameter PDMS. The cure heating process in this simulation is same as the cure process we use in FlexTrate™. PDMS is cured at ambient 30 °C for 24 hours.

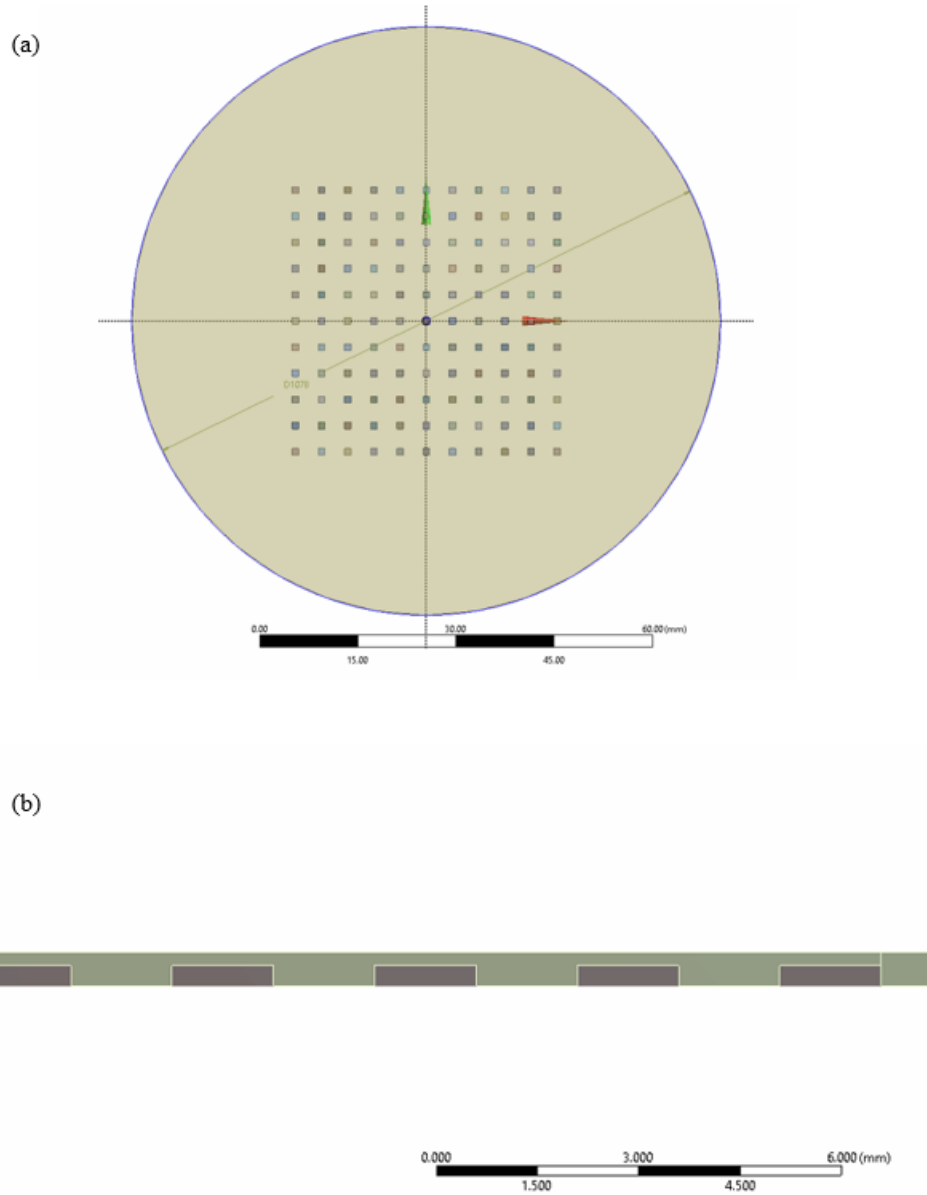


Figure A-12. Geometry model in ANSYS simulation. (a). Top View of PDMS embed with dies; (c). Cross section of PDMS embed with dies.

The contact between PDMS and dies are bonded because the PDMS flow on the surface of dies is ignored. A 5N force is applied on top of the handler, and a fixed support is placed at the edge of PDMS. After 24 hours cure, the force and the supports are released. All the boundary conditions are listed in Table 5-3.

Table 5-3 List of boundary conditions

Contact Bodies	Boundary Conditions	
	During cure	after cure
PDMS to Dies	bonded	bonded
PDMS to 1st Handler	Fixed	Free
PDMS to 2nd Handler	Fixed	Fixed
Dies to 1st Handler	Fixed	Free

Die size, PDMS thickness, die intervals, die thickness are variables studied in this work to understand how these parameters can affect die shift, which will be discussed in the next chapter.

Table 5-4 The parameters of the simulation design.

(mm)	Die Sizes	1 x 1
		1.5 x 1.5
		2 x 2
		3 x 3
		5 x 5
(mm)	Die Intervals	1
		1.5
		2
		3
		5
Die Thickness		200

	(μm)	300
		400
		500
PDMS Thickness	(μm)	600
		1000

A.5 Results of PDMS shrinkage and die shift

A.5.1 PDMS cure kinetics

Cure kinetics of PDMS is studied by determining the heat release rate during heating Figure A-13 and Table 5-5 summaries the DSC results for curing PDMS. In the theory mentioned in introduction, the heat released in each monomers reaction is constant, therefore, heat release rate can be considered as cure rate (Figure A-13 (a)) and the total heat of reaction can be considered as degree of cure (Figure A-13 (b)) after normalization. Figure A-13 (a), peak temperature increases with increasing heating rate, which means the curing rating increases as well.

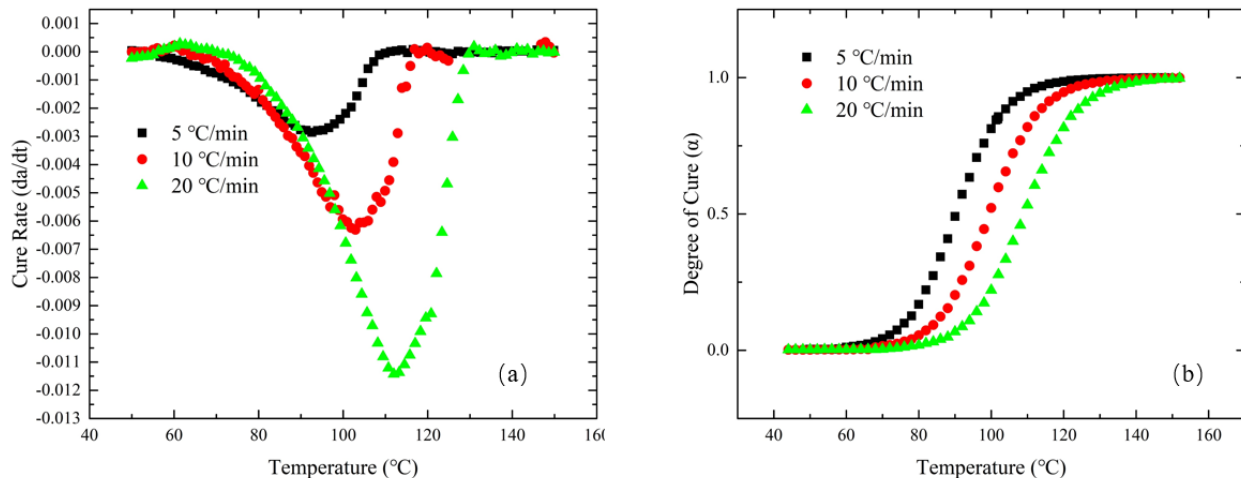


Figure A-13. DSC Results: (a). Dynamic DSC curves; (b) and their running integral at different heating rates.

Table 5-5 Summary of DSC experiment results.

Sample ID	Weight (mg)	Heating rate (°C/min)	Total heat of reaction (mJ)	Heat of reaction (J/g)	Peak cure rate (dα/dt)
1	7	5	64.541	5.8673	-0.00287
2	8	10	57.014	7.1268	-0.00634
3	10	20	61.197	6.1197	-0.01156

Autocatalytic Model is adopted to describe the DSC curve and calculate the activation energy and the preexponential factor k_0 . By taking the logarithm on both sides of the equation, we can get the form:

$$\ln \left(\frac{d\alpha}{dt(\alpha^m(1-\alpha)^n)} \right) = \ln k_0 + \frac{E_a}{RT}$$

Since k_0 , E_a and R is constant, we can plot the Figure A-13(b) into $\ln \left(\frac{d\alpha}{dt(\alpha^m(1-\alpha)^n)} \right)$ verse $1000/T$ in a straight line. Adjusting the factor m and n to fit the experiment data as close as possible. Figure A- shows the adjusted plot when $m = 0.59$ and $n = 1.49$ which is chosen in this work, and the standard deviation R^2 is 0.9836. The activation energy can be obtained from the slope of the line and the preexponential factor from the intercept.

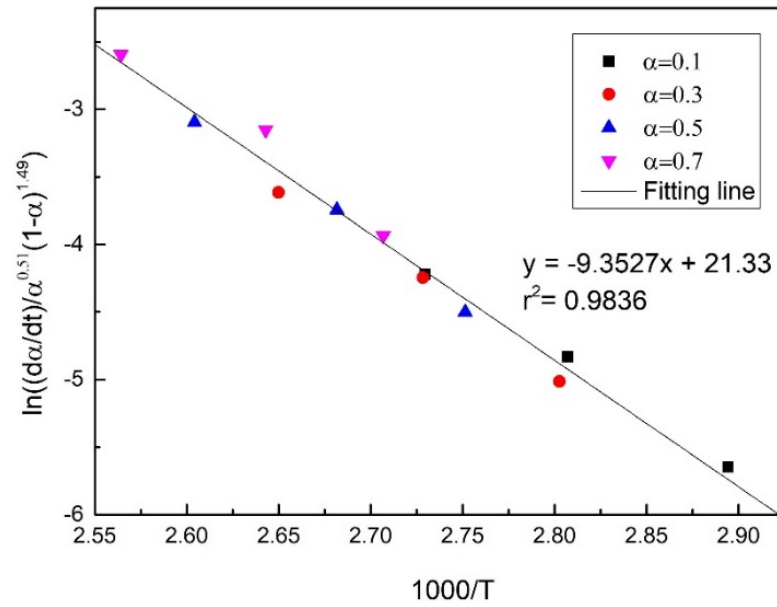


Figure A-14. Autocatalytic model at varying conversions.

Finally, partial differential autocatalytic equation is used to describe the cure behavior of PDMS:

$$\frac{d\alpha}{dt} = 1.834 \times 10^{-9} \times e^{\frac{-9261.46}{RT}} \times \alpha^{0.59}(1 - \alpha)^{1.41}$$

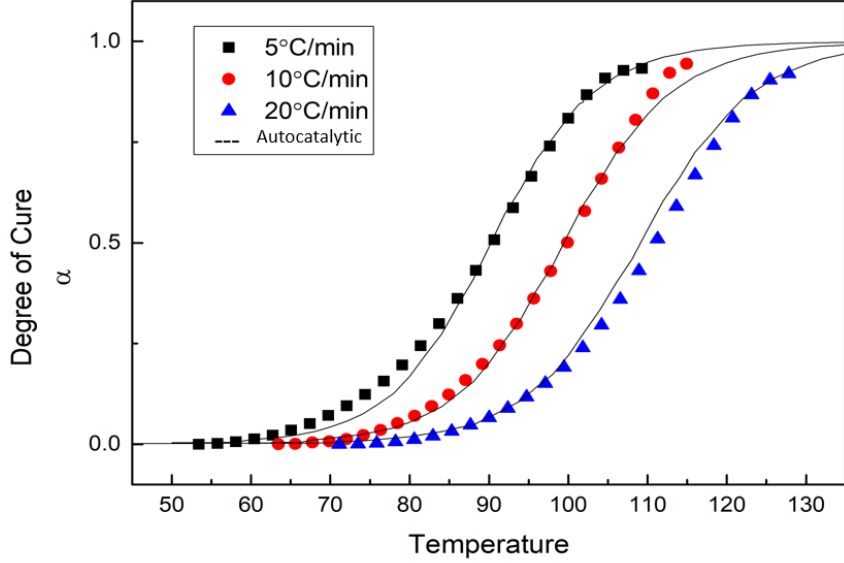


Figure A-15. Comparing the autocatalytic Model with experiment results.

By applying the Autocatalytic equation into Ansys Workbench Transient, the degree of cure, temperature distribution, and materials state versus time can be simulated. Figure A-15 shows the PDMS degree of cure versus time and the heat of reaction during FlexTrate™ process. From Figure A-16 (a), PDMS is almost fully cured after 24 hours curing at 30 °C. PDMS is cured around 80% at first 12 hours. Figure A-16 (b) indicates the highest curing rate happens after 6 hours cure. Since PDMS is cured at a low temperature and it has a very thin geometric structure, the released heat is negligible during cure process, which gives a very even distribution of temperature and the degree of cure across the whole substrate.

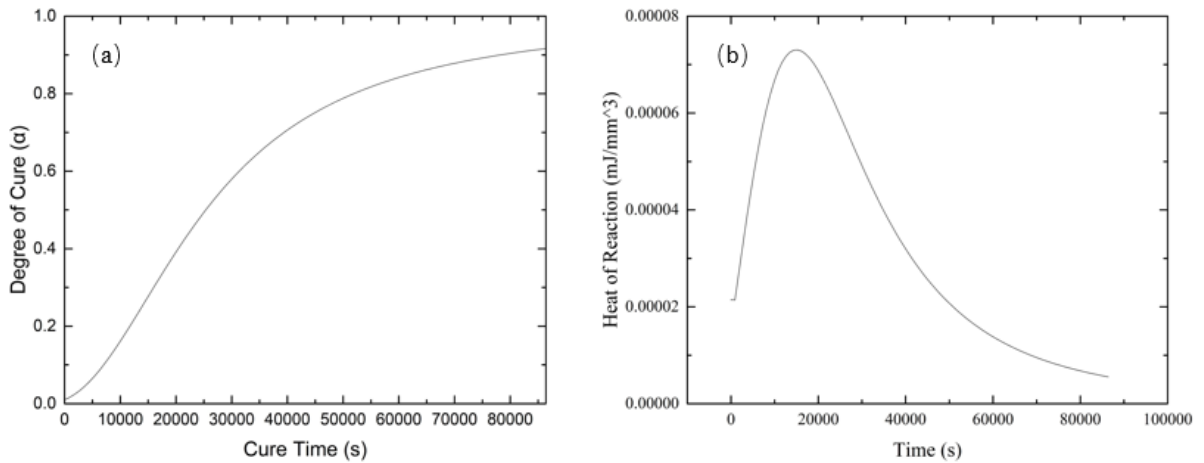


Figure A-16. ANSYS Transient Thermal module simulation of (a). PDMS degree of cure, and (b). Heat of reaction verse time in FlexTrate™ process.

A.5.2 PDMS shrinkage characterization

Figure A-17 shows a matrix of gold pattern on PDMS taken by the Nanotronics nSpec tool. The pattern is on PDMS after releasing the first handler. The designed interval distance of each pattern is 2.2 mm.

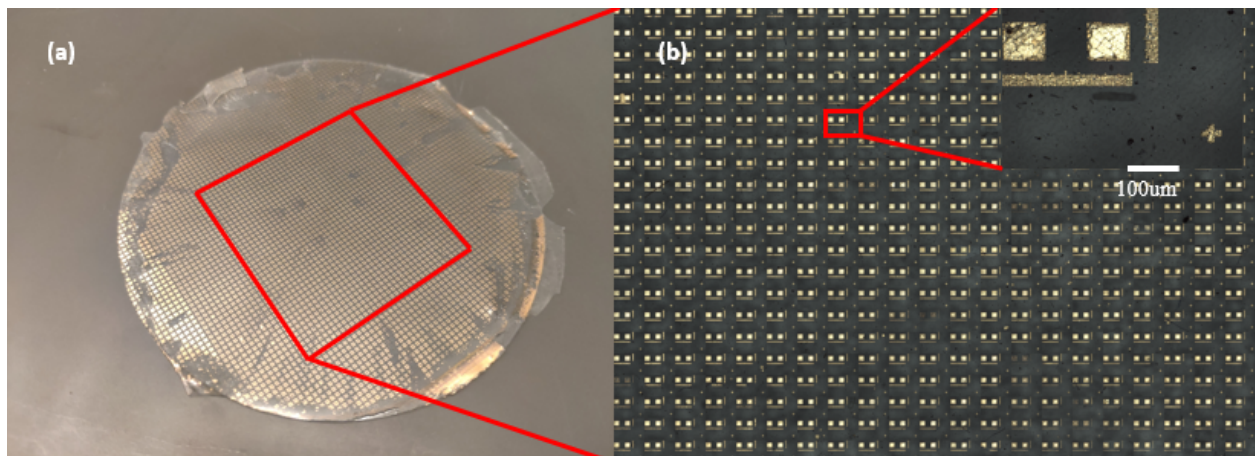


Figure A-17. (a). 90mm diameter PDMS with gold pattern; (b). Gold pattern on PDMS taken by nSpecs.

Figure A-18 is a mosaic graph which shows every gold pattern's shift measured by nSpec after release of first handler (a), and second handler (b). The value in each check indicates the

pattern's total shift distance. Colors from blue to yellow to red indicate the shrinkage distance becomes larger. The blanks are excluded data due to mismeasurement.

The results indicate that the shrinkage of PDMS is isotropic and radial, and the further away from the center the greater the shrinkage, which is reasonable because cured PDMS is isotropic material. It verified the assumption that the shrinkage of PDMS is linearly proportional to the degree of cure, providing a theoretical confirmation for the PDMS shrinkage simulation. The average shrinkage ratio is measured, which is 0.12% after releasing first handler and 0.24% after releasing second handler. By applying this shrinkage ratio parameter and degree of cure data into ANSYS Static Structural Simulation, the PDMS shrinkage profile is simulated, shown in Figure A-19. Figure A-20 compares the experiment data and simulation data of PDMS shrinkage. The simulation data fit the experiment data well.

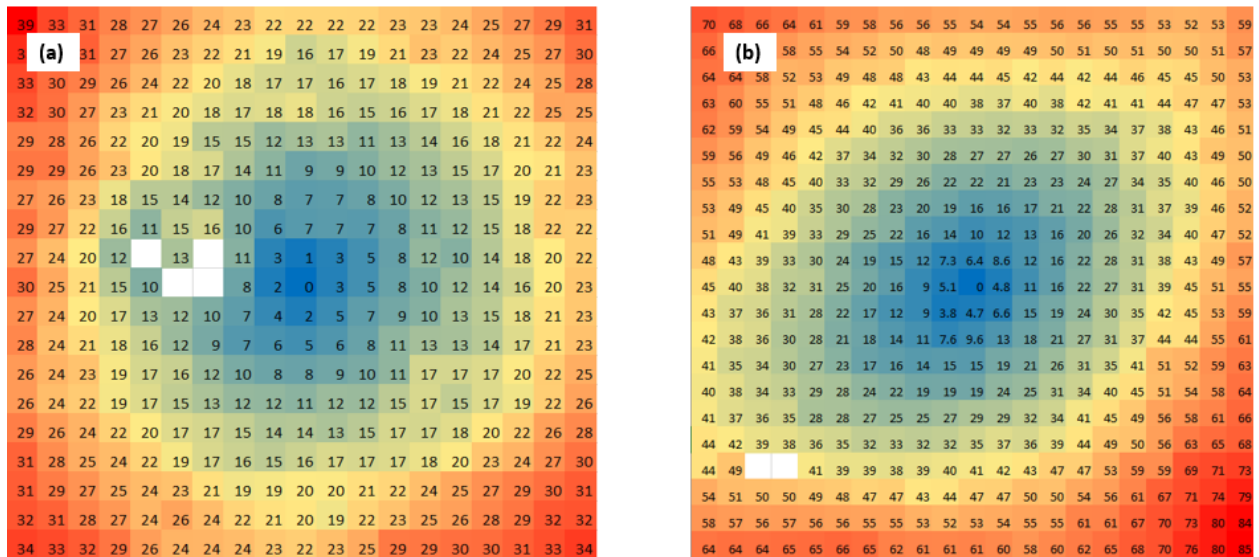


Figure A-18. Gold patterns shift on PDMS due to cure shrinkage (a). after release first handler; (b). After release second handler.

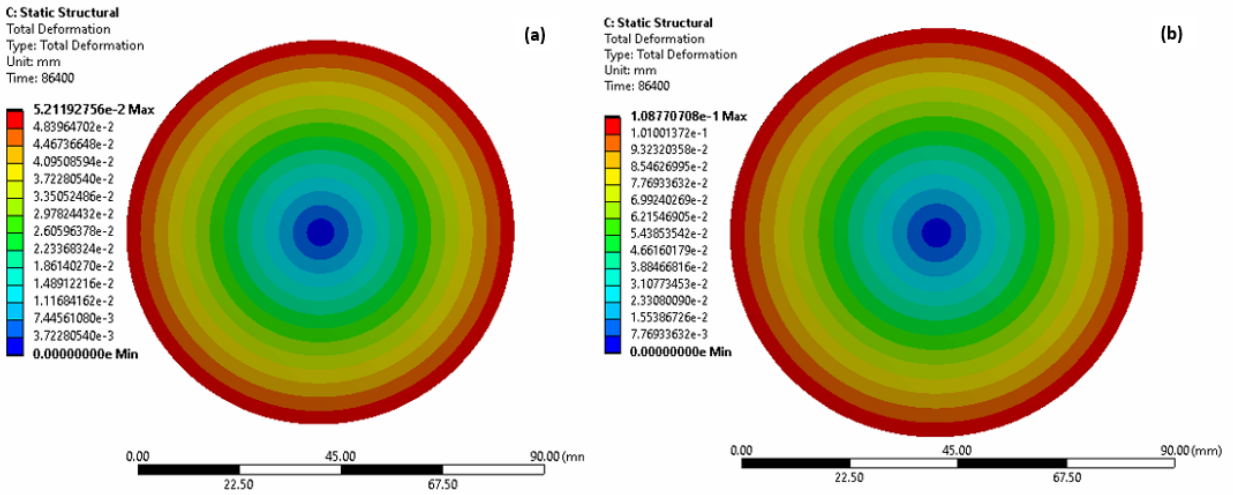


Figure A-19. PDMS shrinkage simulation after release (a) first handler and (b) second handler.

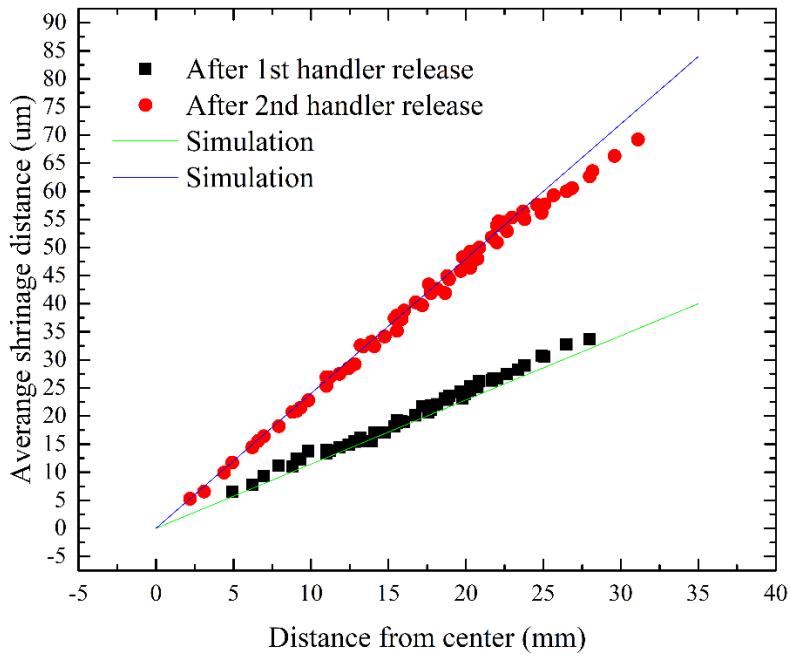


Figure A-20. Points: the experiment average shrinkage of PDMS verse distance from the center. Lines: the simulation results of PDMS shrinkage verse distance from the center.

A.5.3 Parametric study of die shift

Figure A-21 (© 2022 IEEE) is the simulation result generated from ANSYS models described in the last section. The interval distance between dies is 1.5 mm, the thickness is 300 μm , and the matrix is 11 x 11, a total of 121 dies. Die sizes used are 1 mm x 1 mm, 1.5 x 1.5 mm, 2 x 2 mm, 3 x 3mm, to 5 x 5 mm. Since 5 x 5 mm die size in 11 x 11 matrix occupied an area larger than PDMS, it is reduced to 10 x 10 matrix. Color Contour in each figure represents the degree of displacement, blue represents the minimum displacement, and red, the maximum displacement. Figure A-21 (b) compares the original die position with the position after cure. It shows that the die shift is radial.

Figure A-23 (a) compares die shift verse distance from center for different die sizes. Six dies are selected in each model and are distributed diagonally. The dies selected are shown in Figure A-23 (b). Since the pattern is symmetric across the whole model, the center die shift is 0. In each pattern, die displacement increases linearly from the center. The shift ratios, the ratio of die shift to its distance from center, are 0.085%, 0.078%, 0.065%, 0.038%, and 0.011% respectively for 1 x 1 mm, 1.5 x 1.5 mm, 2 x 2 mm, 3 x 3 mm, and 5 x 5 mm. The die shift ratios decrease almost linearly with increasing die size. This may be because the larger the dies, the smaller the stress they would experience.

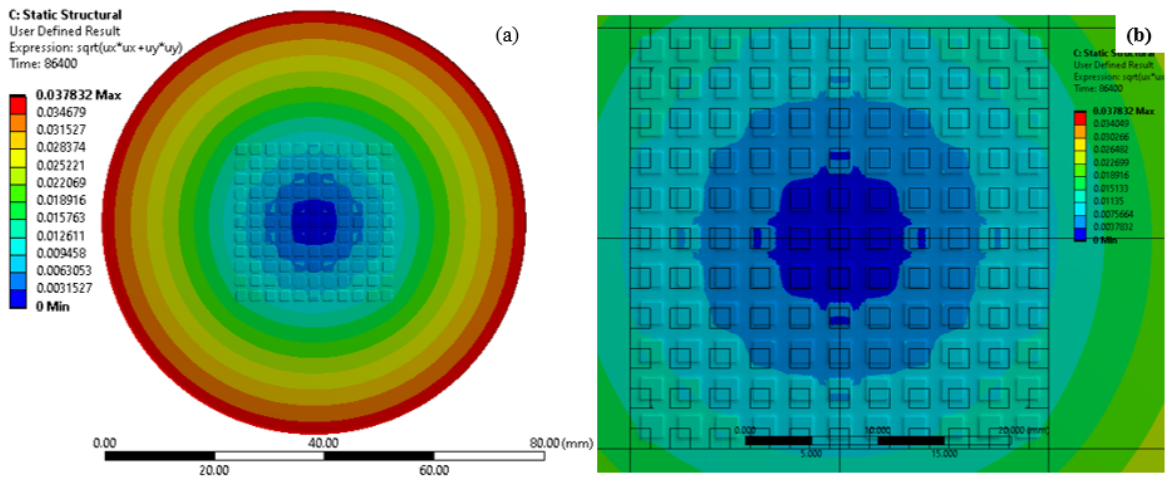


Figure A-21. (a). One of the die shift simulation results. (b). The scaled figure of (a), the black wireframe is the original die's position.

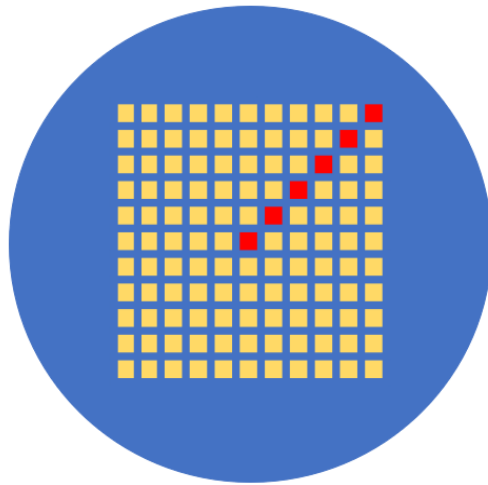


Figure A-22. The data select rule on each simulation.

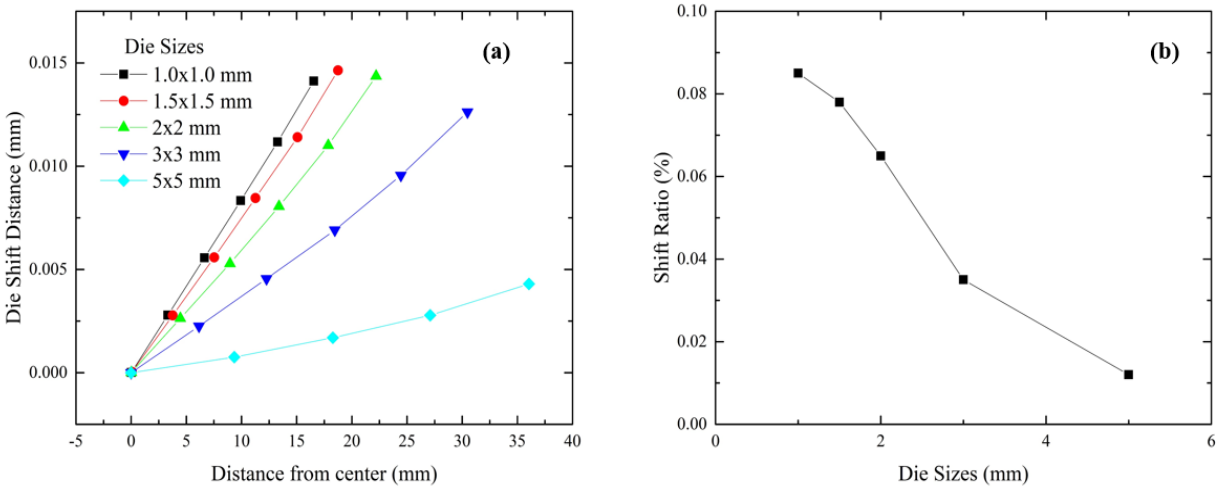


Figure A-23. (a). Simulation results of die shift verse die distance from center to the corner of matrix in different die size; (b). Die shift ratio verse different die sizes.

Figure A-24 shows the die shift for different die intervals. The size of each die is 1x1 mm, thickness is 300 μm , and the matrix is 11 x 11 number of dies. Die intervals are 1 mm, 1.5 mm, 2 mm, 3 mm, 5 mm, respectively.

Like the previous case, the minimum die shift is 0 at the center. Die shift linearly increases with the increase of the die position. The shift ratios are 0.079%, 0.085%, 0.089%, 0.094%, and 0.099% respectively for 1 mm, 1.5 mm, 2 mm, 3 mm, and 5 mm intervals. The die shift ratio slightly increases with increasing die intervals. However, because increasing die intervals will make the pattern looser and more relaxed, the maximum die shift increase significantly. It should be taken into consideration in the step of pattern design. The closer the dies are put together, the smaller the dies shift.

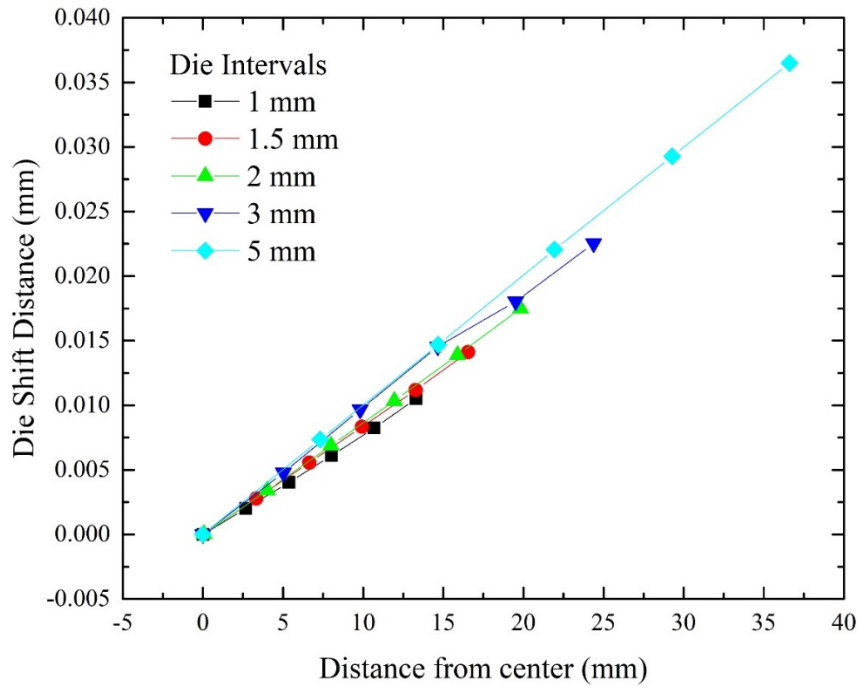


Figure A-24. Simulation results of die shift verse die intervals from center to the corner of matrix in different die size

Figure A-25 shows the die shift for different die thickness (a) and different PDMS thickness (b). The size of each die is 1x1 mm, die interval is 1.5 mm, and the matrix is 11 x 11 number of dies.

For different die thicknesses, the die shift ratios are about 0.092%, 0.090%, and 0.089% at 200 μm , 300 μm , and 400 μm . For different PDMS thicknesses, the die shift ratios are about 0.078%, 0.081%, and 0.083%.

In both cases, die shift increases linearly as previous cases. Die thickness and PDMS thickness do not show the same significant effect on die shift as die interval or die size factors. However increasing die or PDMS thicknesses will reduce the flexibility of device.

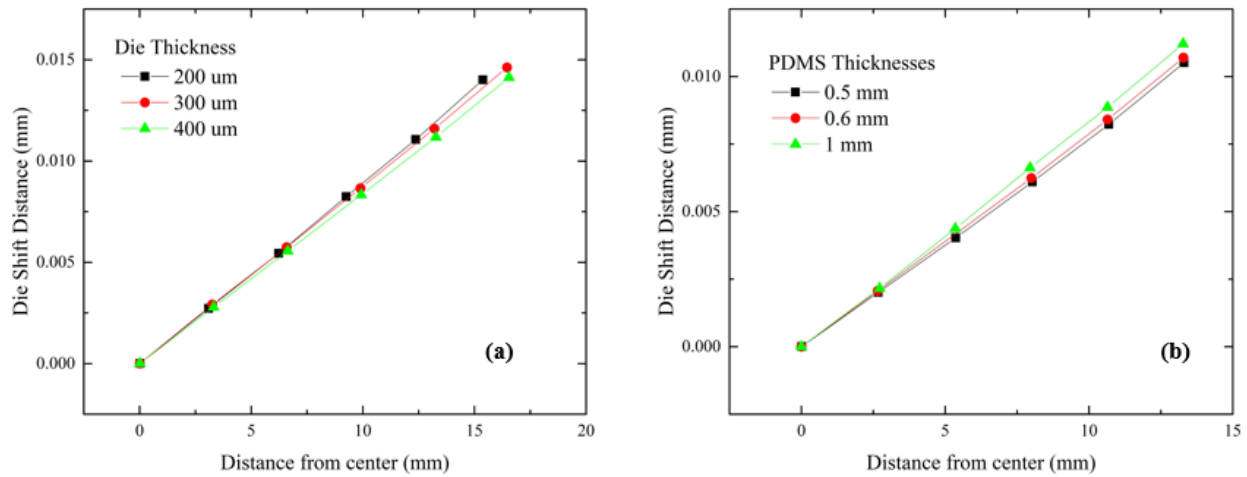


Figure A-25. Die shift difference (a). between different die thickness, and (b). different PDMS Thickness.

A.5.4 Die shift prediction on surface electromyography (sEMG) system

In addition to analyzing the factors that affect die shift, the die shift model can also be applied to predict the die shift on any device using FlexTrate™ process as shown in figure A-26 (© 2023 IEEE). One demonstration is to predict the die shift of sEMG system [22] in

Table 5-6. These are two devices placed in an x-axis mirror design. The PDMS thickness is 2 mm and the diameter is 90 mm. By using the theoretical model created in this work, each die's shift is predicted. Unlike the results shown in last section, the die shift is not symmetric since the device layout is not symmetric and it contains different sized dies. Therefore, each die shift in x and y direction should be analyzed individually.

Table 5-6 summaries each die's dimension and shift from simulation. The simulation result can be used as a reference for die interconnection design in the future.

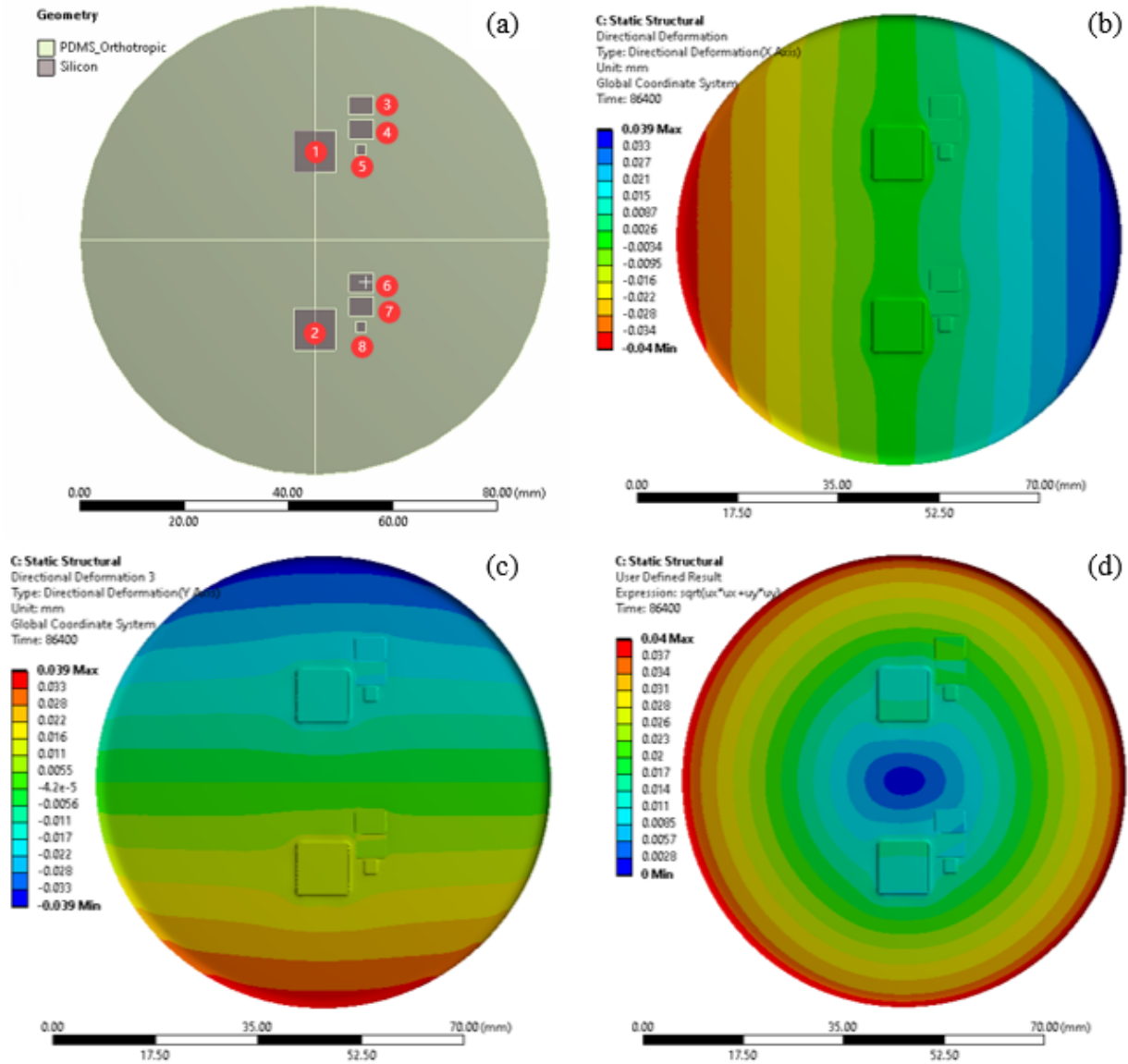


Figure A-26. (a). The geometry of two mirror-designed flexible sEMG systems on PDMS. Number 1 & 2 are Bluetooth chips; 3, 4, 6, 7 are capacitors, and 5, 8 are amplifiers. (b). Simulation of the die shift in x axis direction. (c). Simulation of the die shift in y axis.

Table 5-6 Summary of die dimensions and die shift results.

Sample ID	Function	Dimension (L x W x H mm)	Shift in X direction (μm)	Shift in Y direction (μm)	Total shift (μm)
1	Bluetooth	8 x 8 x 1	0.21	13.6	13.9
2	Bluetooth	8 x 8 x 1	0.37	12.5	13
3	Capacitor	4.7 x 3.6 x 0.1	5.5	19.4	20.1
4	Capacitor	4.7 x 3.6 x 0.1	4.89	16.4	17
5	Amplifier	2.2 x 1.8 x 0.4	5	14.1	14.9
6	Capacitor	4.7 x 3.6 x 0.1	5.6	7.3	9.3
7	Capacitor	4.7 x 3.6 x 0.1	4.9	10.6	11.6
8	Amplifier	2.2 x 1.8 x 0.4	5	12.9	13.7

REFERENCES

- [1] J. M. Raja *et al.*, “Apple Watch, Wearables, and Heart Rhythm: where do we stand?,” *Ann. Transl. Med.*, vol. 7, no. 17, p. 417, Sep. 2019, doi: 10.21037/atm.2019.06.79.
- [2] C. E. King and M. Sarrafzadeh, “A Survey of Smartwatches in Remote Health Monitoring,” *J. Healthc. Inform. Res.*, vol. 2, no. 1, pp. 1–24, Jun. 2018, doi: 10.1007/s41666-017-0012-7.
- [3] Y. Ni, Y. Wang, and W. Xu, “Recent Process of Flexible Transistor-Structured Memory,” *Small*, vol. 17, no. 9, p. 1905332, 2021, doi: 10.1002/sml.201905332.
- [4] S. Yuvaraja *et al.*, “Organic field-effect transistor-based flexible sensors,” *Chem. Soc. Rev.*, vol. 49, no. 11, pp. 3423–3460, 2020, doi: 10.1039/C9CS00811J.
- [5] Z.-W. Shang, H.-H. Hsu, Z.-W. Zheng, and C.-H. Cheng, “Progress and challenges in p-type oxide-based thin film transistors,” *Nanotechnol. Rev.*, vol. 8, no. 1, pp. 422–443, Jan. 2019, doi: 10.1515/ntrev-2019-0038.
- [6] Y. Gao, L. Yu, J. C. Yeo, and C. T. Lim, “Flexible Hybrid Sensors for Health Monitoring: Materials and Mechanisms to Render Wearability,” *Adv. Mater.*, vol. 32, no. 15, p. 1902133, 2020, doi: 10.1002/adma.201902133.
- [7] D. M. Dyson, “Flexible Hybrid Electronics: Conforming to the Market,” p. 42.
- [8] S. Gong, L. W. Yap, B. Zhu, and W. Cheng, “Multiscale Soft–Hard Interface Design for Flexible Hybrid Electronics,” *Adv. Mater.*, vol. 32, no. 15, p. 1902278, 2020, doi: 10.1002/adma.201902278.
- [9] T. Fukushima *et al.*, “‘FlexTrate TM’ — Scaled Heterogeneous Integration on Flexible Biocompatible Substrates Using FOWLP,” in *2017 IEEE 67th Electronic Components and Technology Conference (ECTC)*, May 2017, pp. 649–654. doi: 10.1109/ECTC.2017.226.

- [10] A. Hanna *et al.*, “Extremely Flexible (1mm Bending Radius) Biocompatible Heterogeneous Fan-Out Wafer-Level Platform with the Lowest Reported Die-Shift (<6 μm) and Reliable Flexible Cu-Based Interconnects,” in *2018 IEEE 68th Electronic Components and Technology Conference (ECTC)*, San Diego, CA: IEEE, May 2018, pp. 1505–1511. doi: 10.1109/ECTC.2018.00229.
- [11] A. Alam *et al.*, “A High Spatial Resolution Surface Electromyography (sEMG) System Using Fan-Out Wafer-Level Packaging on FlexTrate™,” in *2020 IEEE 70th Electronic Components and Technology Conference (ECTC)*, Jun. 2020, pp. 985–990. doi: 10.1109/ECTC32862.2020.00160.
- [12] G. Ezhilarasu, A. Hanna, R. Irwin, A. Alam, and S. S. Iyer, “A Flexible, Heterogeneously Integrated Wireless Powered System for Bio-Implantable Applications using Fan-Out Wafer-Level Packaging,” in *2018 IEEE International Electron Devices Meeting (IEDM)*, Dec. 2018, p. 29.7.1-29.7.4. doi: 10.1109/IEDM.2018.8614705.
- [13] T. Fukushima *et al.*, “Self-Assembly Technologies for FlexTrate™,” in *2018 IEEE 68th Electronic Components and Technology Conference (ECTC)*, May 2018, pp. 1836–1841. doi: 10.1109/ECTC.2018.00275.
- [14] N. Takahashi *et al.*, “RDL-first Flexible FOWLP Technology with Dielets Embedded in Hydrogel,” in *2020 IEEE 70th Electronic Components and Technology Conference (ECTC)*, Jun. 2020, pp. 811–816. doi: 10.1109/ECTC32862.2020.00132.
- [15] A. Alam *et al.*, “Heterogeneous Integration of a Fan-Out Wafer-Level Packaging Based Foldable Display on Elastomeric Substrate,” in *2019 IEEE 69th Electronic Components and Technology Conference (ECTC)*, Las Vegas, NV, USA: IEEE, May 2019, pp. 277–282. doi: 10.1109/ECTC.2019.00048.

- [16] Y. Khan, A. E. Ostfeld, C. M. Lochner, A. Pierre, and A. C. Arias, “Monitoring of Vital Signs with Flexible and Wearable Medical Devices,” *Adv. Mater. Deerfield Beach Fla*, vol. 28, no. 22, pp. 4373–4395, Jun. 2016, doi: 10.1002/adma.201504366.
- [17] T. R. Ray, “Bio-integrated wearable systems: a comprehensive review,” *Chem Rev*, vol. 119, 2019, doi: 10.1021/acs.chemrev.8b00573.
- [18] C. García Núñez, L. Manjakkal, and R. Dahiya, “Energy autonomous electronic skin,” *Npj Flex. Electron.*, vol. 3, Jan. 2019, doi: 10.1038/s41528-018-0045-x.
- [19] “nRF52832 - Nordic Semiconductor.” Accessed: Apr. 28, 2024. [Online]. Available: <https://www.nordicsemi.com/Products/nRF52832>
- [20] S. M. A. Iqbal, I. Mahgoub, E. Du, M. A. Leavitt, and W. Asghar, “Advances in healthcare wearable devices,” *Npj Flex. Electron.*, vol. 5, no. 1, pp. 1–14, Apr. 2021, doi: 10.1038/s41528-021-00107-x.
- [21] Y. Ma *et al.*, “Flexible Hybrid Electronics for Digital Healthcare,” *Adv. Mater.*, vol. 32, no. 15, p. 1902062, 2020, doi: 10.1002/adma.201902062.
- [22] B. Su *et al.*, “Scientific athletics training: Flexible sensors and wearable devices for kineses monitoring applications,” *Sci. Sin. Informationis*, Nov. 2021, doi: 10.1360/SSI-2021-0294.
- [23] H. Yu, N. Li, and N. Zhao, “How Far Are We from Achieving Self-Powered Flexible Health Monitoring Systems: An Energy Perspective,” *Adv. Energy Mater.*, vol. 11, no. 9, p. 2002646, 2021, doi: 10.1002/aenm.202002646.
- [24] X. Gong, Q. Yang, C. Zhi, and P. S. Lee, “Stretchable Energy Storage Devices: From Materials and Structural Design to Device Assembly,” *Adv. Energy Mater.*, vol. n/a, no. n/a, p. 2003308, doi: <https://doi.org/10.1002/aenm.202003308>.

- [25] J. Peng and G. J. Snyder, “A figure of merit for flexibility,” *Science*, vol. 366, no. 6466, pp. 690–691, Nov. 2019, doi: 10.1126/science.aaz5704.
- [26] Y. S. Zhang *et al.*, “A Review of Lithium-Ion Battery Electrode Drying: Mechanisms and Metrology,” *Adv. Energy Mater.*, vol. 12, no. 2, p. 2102233, 2022, doi: 10.1002/aenm.202102233.
- [27] S. Zhang, K. Zhao, T. Zhu, and J. Li, “Electrochemomechanical degradation of high-capacity battery electrode materials,” *Prog. Mater. Sci.*, vol. 89, pp. 479–521, Aug. 2017, doi: 10.1016/j.pmatsci.2017.04.014.
- [28] R. Jain *et al.*, “Nanostructuring versus microstructuring in battery electrodes,” *Nat. Rev. Mater.*, vol. 7, no. 9, pp. 736–746, Sep. 2022, doi: 10.1038/s41578-022-00454-9.
- [29] G. Bucci, T. Swamy, Y.-M. Chiang, and W. C. Carter, “Modeling of internal mechanical failure of all-solid-state batteries during electrochemical cycling, and implications for battery design,” *J. Mater. Chem. A*, vol. 5, no. 36, pp. 19422–19430, Sep. 2017, doi: 10.1039/C7TA03199H.
- [30] G. Liang, J. Zhu, A. Chen, Q. Yang, and C. Zhi, “Adhesive and cohesive force matters in deformable batteries,” *Npj Flex. Electron.*, vol. 5, no. 1, pp. 1–4, Sep. 2021, doi: 10.1038/s41528-021-00124-w.
- [31] A. Schilling, J. Schmitt, F. Dietrich, and K. Dröder, “Analyzing Bending Stresses on Lithium-Ion Battery Cathodes induced by the Assembly Process,” *Energy Technol.*, vol. 4, no. 12, pp. 1502–1508, 2016, doi: 10.1002/ente.201600131.
- [32] X. Ge *et al.*, “Mechano-Graded Electrodes Mitigate the Mismatch between Mechanical Reliability and Energy Density for Foldable Lithium-Ion Batteries,” *Adv. Mater.*, vol. 34, no. 45, p. 2206797, 2022, doi: 10.1002/adma.202206797.

- [33] A. J. Blake *et al.*, “Creasable Batteries: Understanding Failure Modes through Dynamic Electrochemical Mechanical Testing,” *ACS Appl. Mater. Interfaces*, vol. 8, no. 8, pp. 5196–5204, Mar. 2016, doi: 10.1021/acsami.5b11175.
- [34] Y. Liang *et al.*, “A review of rechargeable batteries for portable electronic devices,” *InfoMat*, vol. 1, no. 1, pp. 6–32, 2019, doi: 10.1002/inf2.12000.
- [35] T. K. Lee *et al.*, “PEO based polymer electrolyte comprised of epoxidized natural rubber material (ENR50) for Li-Ion polymer battery application,” *Electrochimica Acta*, vol. 316, pp. 283–291, Sep. 2019, doi: 10.1016/j.electacta.2019.05.143.
- [36] W. J. Chang *et al.*, “Direct Observation of Carboxymethyl Cellulose and Styrene–Butadiene Rubber Binder Distribution in Practical Graphite Anodes for Li-Ion Batteries,” *ACS Appl. Mater. Interfaces*, vol. 11, no. 44, pp. 41330–41337, Nov. 2019, doi: 10.1021/acsami.9b13803.
- [37] J. Li, R. B. Lewis, and J. R. Dahn, “Sodium Carboxymethyl Cellulose: A Potential Binder for Si Negative Electrodes for Li-Ion Batteries,” *Electrochem. Solid-State Lett.*, vol. 10, no. 2, p. A17, Dec. 2006, doi: 10.1149/1.2398725.
- [38] “3D-Printed All-Fiber Li-Ion Battery toward Wearable Energy Storage - Wang - 2017 - Advanced Functional Materials - Wiley Online Library.” Accessed: Feb. 19, 2022. [Online]. Available: <https://onlinelibrary.wiley.com/doi/full/10.1002/adfm.201703140>
- [39] A. Babapoor, M. Azizi, and G. Karimi, “Thermal management of a Li-ion battery using carbon fiber-PCM composites,” *Appl. Therm. Eng.*, vol. 82, pp. 281–290, May 2015, doi: 10.1016/j.applthermaleng.2015.02.068.

- [40] J. Zhou *et al.*, “A Quasi-Solid-State Flexible Fiber-Shaped Li–CO₂ Battery with Low Overpotential and High Energy Efficiency,” *Adv. Mater.*, vol. 31, no. 3, p. 1804439, 2019, doi: 10.1002/adma.201804439.
- [41] L. Huang, Z. Zhang, Z. Wang, L. Zhang, X. Zhu, and D. D. Dorrell, “Thermal runaway behavior during overcharge for large-format Lithium-ion batteries with different packaging patterns,” *J. Energy Storage*, vol. 25, p. 100811, Oct. 2019, doi: 10.1016/j.est.2019.100811.
- [42] E. Foreman *et al.*, “A Review of Inactive Materials and Components of Flexible Lithium-Ion Batteries,” *Adv. Sustain. Syst.*, vol. 1, no. 11, p. 1700061, 2017, doi: 10.1002/adsu.201700061.
- [43] A. A. Bajwa *et al.*, “Demonstration of a Heterogeneously Integrated System-on-Wafer (SoW) Assembly,” in *2018 IEEE 68th Electronic Components and Technology Conference (ECTC)*, May 2018, pp. 1926–1930. doi: 10.1109/ECTC.2018.00288.
- [44] G. Ouyang, G. Whang, E. MacInnis, and S. S. Iyer, “Fabrication of Flexible Ionic-Liquid Thin Film Battery Matrix on FlexTrate™ for Powering Wearable Devices,” in *2021 IEEE 71st Electronic Components and Technology Conference (ECTC)*, Jun. 2021, pp. 1620–1626. doi: 10.1109/ECTC32696.2021.00257.
- [45] V. Nilsson, R. Younesi, D. Brandell, K. Edström, and P. Johansson, “Critical evaluation of the stability of highly concentrated LiTFSI - Acetonitrile electrolytes vs. graphite, lithium metal and LiFePO₄ electrodes,” *J. Power Sources*, vol. 384, pp. 334–341, Apr. 2018, doi: 10.1016/j.jpowsour.2018.03.019.
- [46] X.-G. Sun and S. Dai, “Electrochemical investigations of ionic liquids with vinylene carbonate for applications in rechargeable lithium ion batteries,” *Electrochimica Acta*, vol. 55, no. 15, pp. 4618–4626, Jun. 2010, doi: 10.1016/j.electacta.2010.03.019.

- [47] A. Guerfi *et al.*, “Improved electrolytes for Li-ion batteries: Mixtures of ionic liquid and organic electrolyte with enhanced safety and electrochemical performance,” *J. Power Sources*, vol. 195, no. 3, pp. 845–852, Feb. 2010, doi: 10.1016/j.jpowsour.2009.08.056.
- [48] H. Srour *et al.*, “Ionic liquid-based electrolytes for lithium-ion batteries: review of performances of various electrode systems,” *J. Appl. Electrochem.*, vol. 46, no. 2, pp. 149–155, Feb. 2016, doi: 10.1007/s10800-015-0905-1.
- [49] A. Balducci, “Ionic Liquids in Lithium-Ion Batteries,” *Top. Curr. Chem.*, vol. 375, no. 2, p. 20, Feb. 2017, doi: 10.1007/s41061-017-0109-8.
- [50] M. Kerner, N. Plylahan, J. Scheers, and P. Johansson, “Thermal stability and decomposition of lithium bis(fluorosulfonyl)imide (LiFSI) salts,” *RSC Adv.*, vol. 6, no. 28, pp. 23327–23334, 2016, doi: 10.1039/C5RA25048J.
- [51] C. Choi *et al.*, “Achieving high energy density and high power density with pseudocapacitive materials,” *Nat. Rev. Mater.*, vol. 5, no. 1, pp. 5–19, Jan. 2020, doi: 10.1038/s41578-019-0142-z.
- [52] M. Kirchhöfer, J. von Zamory, E. Paillard, and S. Passerini, “Separators for Li-Ion and Li-Metal Battery Including Ionic Liquid Based Electrolytes Based on the TFSI⁻ and FSI⁻ Anions,” *Int. J. Mol. Sci.*, vol. 15, no. 8, pp. 14868–14890, Aug. 2014, doi: 10.3390/ijms150814868.
- [53] X. Lu, P. Wang, D. Niyato, D. I. Kim, and Z. Han, “Wireless Charging Technologies: Fundamentals, Standards, and Network Applications,” *IEEE Commun. Surv. Tutor.*, vol. 18, no. 2, pp. 1413–1452, Secondquarter 2016, doi: 10.1109/COMST.2015.2499783.
- [54] S. Y. Hui, “Planar Wireless Charging Technology for Portable Electronic Products and Qi,” *Proc. IEEE*, vol. 101, no. 6, pp. 1290–1301, Jun. 2013, doi: 10.1109/JPROC.2013.2246531.

- [55] N. Shinohara, “The wireless power transmission: inductive coupling, radio wave, and resonance coupling,” *WIREs Energy Environ.*, vol. 1, no. 3, pp. 337–346, 2012, doi: <https://doi.org/10.1002/wene.43>.
- [56] A. Murali, “Design of Inductive Coils for Wireless Power Transfer to Pediatric Implants.”
- [57] Ryu, Daun, Kim, Young Hyun, and Koo, Kyung-Heon, “Performance Measurement of the Wireless Charging Devices Using Elettromagnetic Induction Techniques,” *J. Adv. Navig. Technol.*, vol. 19, no. 3, pp. 237–243, Jun. 2015, doi: 10.12673/JANT.2015.19.3.237.
- [58] J. Li, F. Yin, L. Wang, B. Cui, and D. Yang, “Electromagnetic Induction Position Sensor Applied to Anti-Misalignment Wireless Charging for UAVs,” *IEEE Sens. J.*, vol. 20, no. 1, pp. 515–524, Jan. 2020, doi: 10.1109/JSEN.2019.2940925.
- [59] D. W. Harrist, “Wireless Battery Charging System using Radio Frequency Energy Harvesting.” Accessed: Apr. 17, 2024. [Online]. Available: <https://d-scholarship.pitt.edu/8478/>
- [60] P. Wu, F. Bai, Q. Xue, X. Liu, and S. Y. R. Hui, “Use of Frequency-Selective Surface for Suppressing Radio-Frequency Interference from Wireless Charging Pads,” *IEEE Trans. Ind. Electron.*, vol. 61, no. 8, pp. 3969–3977, Aug. 2014, doi: 10.1109/TIE.2013.2284136.
- [61] S. L. Ho, J. Wang, W. N. Fu, and M. Sun, “A Comparative Study Between Novel Witricity and Traditional Inductive Magnetic Coupling in Wireless Charging,” *IEEE Trans. Magn.*, vol. 47, no. 5, pp. 1522–1525, May 2011, doi: 10.1109/TMAG.2010.2091495.
- [62] “Design and Optimization of Load-Independent Magnetic Resonant Wireless Charging System for Electric Vehicles | IEEE Journals & Magazine | IEEE Xplore.” Accessed: Apr. 17, 2024. [Online]. Available: <https://ieeexplore.ieee.org/abstract/document/8303685>

- [63] H. Kim *et al.*, “Coil Design and Measurements of Automotive Magnetic Resonant Wireless Charging System for High-Efficiency and Low Magnetic Field Leakage,” *IEEE Trans. Microw. Theory Tech.*, vol. 64, no. 2, pp. 383–400, Feb. 2016, doi: 10.1109/TMTT.2015.2513394.
- [64] D. B. Ahire and V. J. Gond, “Wireless power transfer system for biomedical application: A review,” in *2017 International Conference on Trends in Electronics and Informatics (ICEI)*, May 2017, pp. 135–140. doi: 10.1109/ICOEI.2017.8300903.
- [65] T. Fukushima, A. Alam, A. Hanna, S. C. Jangam, A. A. Bajwa, and S. S. Iyer, “Flexible Hybrid Electronics Technology Using Die-First FOWLP for High-Performance and Scalable Heterogeneous System Integration,” *IEEE Trans. Compon. Packag. Manuf. Technol.*, vol. 8, no. 10, pp. 1738–1746, Oct. 2018, doi: 10.1109/TCPMT.2018.2871603.
- [66] T. Agcayazi, K. Chatterjee, A. Bozkurt, and T. K. Ghosh, “Flexible Interconnects for Electronic Textiles,” *Adv. Mater. Technol.*, vol. 3, no. 10, p. 1700277, 2018, doi: 10.1002/admt.201700277.
- [67] F. Xiang *et al.*, “Recent advances in flexible batteries: From materials to applications,” *Nano Res.*, Sep. 2021, doi: 10.1007/s12274-021-3820-2.
- [68] L. Yin *et al.*, “A stretchable epidermal sweat sensing platform with an integrated printed battery and electrochromic display,” *Nat. Electron.*, vol. 5, no. 10, Art. no. 10, Oct. 2022, doi: 10.1038/s41928-022-00843-6.
- [69] Y. J. Hong, H. Jeong, K. W. Cho, N. Lu, and D.-H. Kim, “Wearable and Implantable Devices for Cardiovascular Healthcare: from Monitoring to Therapy Based on Flexible and Stretchable Electronics,” *Adv. Funct. Mater.*, vol. 29, no. 19, p. 1808247, 2019, doi: 10.1002/adfm.201808247.

- [70] H. Sun, G. Ezhilarasu, G. Ouyang, R. Irwin, and S. S. Iyer, "A Heterogeneously Integrated and Flexible Inorganic Micro-display on FlexTrate™ using Fan-Out Wafer-Level Packaging," in *2022 IEEE 72nd Electronic Components and Technology Conference (ECTC)*, May 2022, pp. 1390–1394. doi: 10.1109/ECTC51906.2022.00223.
- [71] G. Ezhilarasu, A. Hanna, A. Paranjpe, and S. S. Iyer, "High Yield Precision Transfer and Assembly of GaN μ LEDs Using Laser Assisted Micro Transfer Printing," in *2019 IEEE 69th Electronic Components and Technology Conference (ECTC)*, May 2019, pp. 1470–1474. doi: 10.1109/ECTC.2019.00226.
- [72] Y. Orikasa *et al.*, "Transient Phase Change in Two Phase Reaction between LiFePO₄ and FePO₄ under Battery Operation," *Chem. Mater.*, vol. 25, no. 7, pp. 1032–1039, Apr. 2013, doi: 10.1021/cm303411t.
- [73] Y. Chen *et al.*, "Application of Galvanostatic Intermittent Titration Technique to Investigate Phase Transformation of LiFePO₄ Nanoparticles," *Electrochimica Acta*, vol. 241, pp. 132–140, Jul. 2017, doi: 10.1016/j.electacta.2017.04.137.
- [74] W. Ki *et al.*, "Chip Stackable, Ultra-thin, High-Flexibility 3D FOWLP (3D SWIFT® Technology) for Hetero-Integrated Advanced 3D WL-SiP," in *2018 IEEE 68th Electronic Components and Technology Conference (ECTC)*, May 2018, pp. 580–586. doi: 10.1109/ECTC.2018.00092.
- [75] L. T. Guan, D. Soon Wee Ho, C. T. Chong, and S. Bhattacharya, "3D FOWLP Integration," in *2020 IEEE 70th Electronic Components and Technology Conference (ECTC)*, Jun. 2020, pp. 1728–1735. doi: 10.1109/ECTC32862.2020.00270.

- [76] Y. Susumago *et al.*, “FOWLP-Based Flexible Hybrid Electronics with 3D-IC Chiplets for Smart Skin Display,” in *2021 IEEE 71st Electronic Components and Technology Conference (ECTC)*, Jun. 2021, pp. 34–39. doi: 10.1109/ECTC32696.2021.00017.
- [77] R. d’Agostino and D. L. Flamm, “Plasma etching of Si and SiO₂ in SF₆–O₂ mixtures,” *J. Appl. Phys.*, vol. 52, no. 1, pp. 162–167, Jan. 1981, doi: 10.1063/1.328468.
- [78] S. R. Oh, “Thick single-layer positive photoresist mold and poly(dimethylsiloxane) (PDMS) dry etching for the fabrication of a glass–PDMS–glass microfluidic device,” *J. Micromechanics Microengineering*, vol. 18, no. 11, p. 115025, Oct. 2008, doi: 10.1088/0960-1317/18/11/115025.
- [79] X. Liu *et al.*, “Fabrication of a Multilayer Implantable Cortical Microelectrode Probe to Improve Recording Potential,” *J. Microelectromechanical Syst. Jt. IEEE ASME Publ. Microstruct. Microactuators Microsens. Microsyst.*, vol. 30, no. 4, pp. 569–581, 2021, doi: 10.1109/jmems.2021.3092230.
- [80] Q. Jiang, S. Zhang, J. Jiang, W. Fei, and Z. Wu, “Pneumatic Enabled Vertical Interconnect Access of Liquid Alloy Circuits toward Highly Integrated Stretchable Electronics,” *Adv. Mater. Technol.*, vol. 6, Feb. 2021, doi: 10.1002/admt.202000966.
- [81] X. Fan, “Wafer level packaging (WLP): Fan-in, fan-out and three-dimensional integration,” in *2010 11th International Thermal, Mechanical Multi-Physics Simulation, and Experiments in Microelectronics and Microsystems (EuroSimE)*, Apr. 2010, pp. 1–7. doi: 10.1109/ESIME.2010.5464548.
- [82] C. Lu, “Overview of Fan-out Wafer Level Package (FO-WLP),” in *2014 9th International Microsystems, Packaging, Assembly and Circuits Technology Conference (IMPACT)*, Oct. 2014, pp. 208–208. doi: 10.1109/IMPACT.2014.7048396.

- [83] J. Sun, S. Zhou, D. Veeramani, and K. Liu, "Prediction of Condition Monitoring Signals Using Scalable Pairwise Gaussian Processes and Bayesian Model Averaging," *IEEE Transactions on Automation Science and Engineering*, pp. 1–12, 2024, doi: [10.1109/TASE.2024.3383811](https://doi.org/10.1109/TASE.2024.3383811).
- [84] J. Sun, S. Zhou, and D. Veeramani, "A neural network-based control chart for monitoring and interpreting autocorrelated multivariate processes using layer-wise relevance propagation," *Quality Engineering*, vol. 35, no. 1, pp. 33–47, Jan. 2023, doi: [10.1080/08982112.2022.2087041](https://doi.org/10.1080/08982112.2022.2087041).
- [85] J. Sun, A. Deep, S. Zhou, and D. Veeramani, "Industrial system working condition identification using operation-adjusted hidden Markov model," *J Intell Manuf*, vol. 34, no. 6, pp. 2611–2624, Aug. 2023, doi: [10.1007/s10845-022-01942-z](https://doi.org/10.1007/s10845-022-01942-z).
- [86] T. Fukushima, A. Alam, A. Hanna, S. C. Jangam, A. A. Bajwa, and S. S. Iyer, "Flexible Hybrid Electronics Technology Using Die-First FOWLP for High-Performance and Scalable Heterogeneous System Integration," *IEEE Trans. Compon. Packag. Manuf. Technol.*, vol. 8, no. 10, pp. 1738–1746, Oct. 2018, doi: [10.1109/TCPMT.2018.2871603](https://doi.org/10.1109/TCPMT.2018.2871603).
- [87] D. Corning, "SILASTIC MDX4-4210 BioMedical Grade Elastomer," no. 51, p. 4.
- [88] Y.-C. Liu, H.-C. Cheng, and Z.-D. Wu, "Molding Compound Effects on Warpage of Fan-out Wafer Level Packaging," in *2018 20th International Conference on Electronic Materials and Packaging (EMAP)*, Clear Water Bay, Hong Kong: IEEE, Dec. 2018, pp. 1–2. doi: [10.1109/EMAP.2018.8660759](https://doi.org/10.1109/EMAP.2018.8660759).
- [89] "Critical extent of reaction of a polydimethylsiloxane polymer network." Accessed: Mar. 27, 2020. [Online].

- [90] “Influence of cross-linker concentration on the cross-linking of PDMS and the network structures formed - ScienceDirect.” Accessed: Sep. 12, 2024. [Online].
- [91] C.-C. Chen, T.-M. Don, T.-H. Lin, and L.-P. Cheng, “A kinetic study on the autocatalytic cure reaction of a cyanate ester resin,” *J. Appl. Polym. Sci.*, vol. 92, no. 5, pp. 3067–3079, 2004, doi: 10.1002/app.20314.
- [92] M. R. Keenan, “Autocatalytic cure kinetics from DSC measurements: Zero initial cure rate,” *J. Appl. Polym. Sci.*, vol. 33, no. 5, pp. 1725–1734, 1987, doi: 10.1002/app.1987.070330525.
- [93] “Poly(Dimethylsiloxane) - an overview | ScienceDirect Topics.” Accessed: May 10, 2020. [Online]. Available: <https://www.sciencedirect.com/topics/materials-science/poly-dimethylsiloxane>
- [94] H.-C. Cheng, C.-H. Chung, and W.-H. Chen, “Die Shift Assessment of Reconstituted Wafer for Fan-Out Wafer-Level Packaging,” *IEEE Trans. Device Mater. Reliab.*, vol. 20, no. 1, pp. 136–145, Mar. 2020, doi: 10.1109/TDMR.2020.2965000.
- [95] Chee Houe Khong *et al.*, “A novel method to predict die shift during compression molding in embedded wafer level package,” in *2009 59th Electronic Components and Technology Conference*, May 2009, pp. 535–541. doi: 10.1109/ECTC.2009.5074066.
- [96] Lin Bu, Siowling Ho, S. D. Velez, Taichong Chai, and Xiaowu Zhang, “Investigation on Die Shift Issues in the 12-in Wafer-Level Compression Molding Process,” *IEEE Trans. Compon. Packag. Manuf. Technol.*, vol. 3, no. 10, pp. 1647–1653, Oct. 2013, doi: 10.1109/TCPMT.2013.2268192.
- [97] G. Sharma, A. Kumar, V. S. Rao, S. W. Ho, and V. Kripesh, “Solutions Strategies for Die Shift Problem in Wafer Level Compression Molding,” *IEEE Trans. Compon. Packag. Manuf. Technol.*, vol. 1, no. 4, pp. 502–509, Apr. 2011, doi: 10.1109/TCPMT.2010.2100431.

- [98] C.-Y. Yang, Y.-C. Liu, K.-S. Chen, T.-S. Yang, Y.-C. Wang, and S.-S. Lee, “Process emulation for predicting die shift and wafer warpage in wafer reconstitution,” in *2017 18th International Conference on Electronic Packaging Technology (ICEPT)*, Aug. 2017, pp. 215–220. doi: 10.1109/ICEPT.2017.8046441.
- [99] Y. Han, M. Z. Ding, B. Lin, and C. S. Choong, “Comprehensive Investigation of Die Shift in Compression Molding Process for 12 Inch Fan-Out Wafer Level Packaging,” in *2016 IEEE 66th Electronic Components and Technology Conference (ECTC)*, May 2016, pp. 1605–1610. doi: 10.1109/ECTC.2016.46.
- [100] “Ling et al_2014_Comprehensive Study on the Interactions of Multiple Die Shift Mechanisms During.pdf.”